Intrinsic three photon correlations mediated by a single Rydberg superatom

Nina Stiesdal
Master thesis

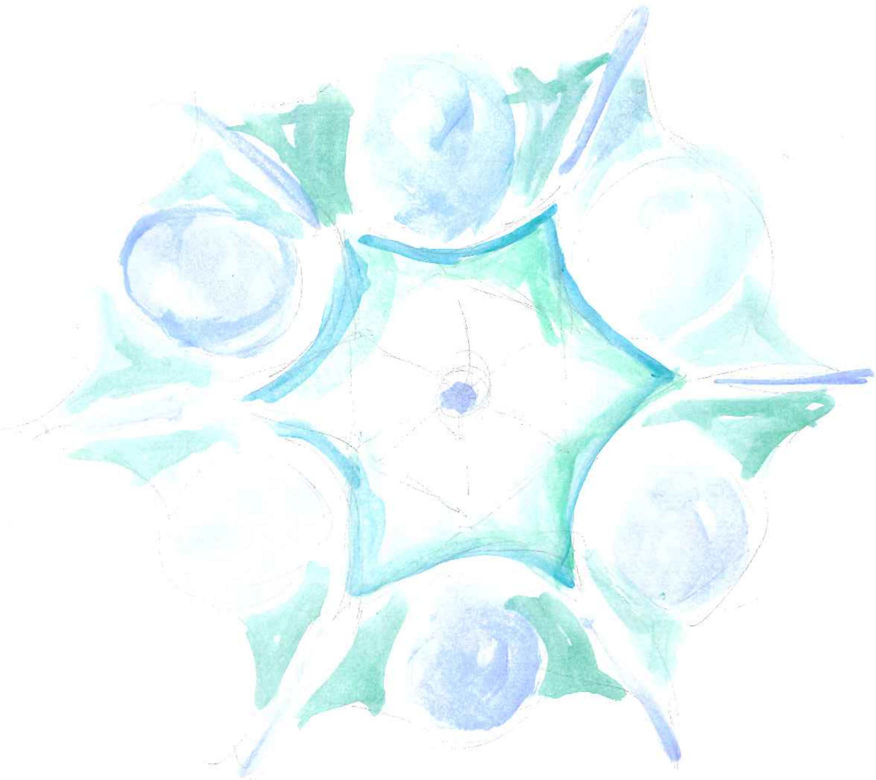

UNIVERSITY OF
SOUTHERN DENMARK

Cover illustration: Doodle of three photon correlation.

Master's thesis

Intrinsic three photon correlations mediated by a single Rydberg superatom

Nina Stiesdal
June 1, 2018

Supervisor: Sebastian Hofferberth

Department of Physics,
Chemistry and Pharmacy

SDU
UNIVERSITY OF
SOUTHERN DENMARK

University of Southern Denmark
Campusvej 55
5230 Odense M

Nonlinear Quantum Optics Group

Abstract

In this thesis, a setup for realization of Rydberg superatoms was implemented in an existing experiment. With this new setup, the modulation of a few photon light pulse mediated by a single Rydberg superatom was investigated.

The setup for realizing such a superatom consist of an additional optical trap, a dimple trap, overlapped with the existing dipole trap. The main component in this additional trap is an acousto optic deflector, which can deflect a laser beam into multiple beams of variable position, and therefore gives the new setup a high degree of versatility, allowing us to realize multiple dimple traps.

With a single dimple trap, a Rydberg superatom was realized. A superatom is an atomic ensemble which behaves collectively as a single atom. The Rydberg superatom consisting of N atoms interacts collectively with a driving field, experiencing a coupling strength enhancement of $\sqrt{N}$ compared to the single atom coupling. Because of this coupling enhancement, our Rydberg superatom will interact with a field of even very few photons.

With the Rydberg superatom the interactions of quantized light with a two level system can be investigated. The system modulates the light pulse on single photon level, causing a signal in the two photon correlation function.

In this thesis, the photon correlating dynamics of the superatom is investigated, showing the signal of up to three photon correlations in the photon third order correlation function and showing the signal of pure three photon correlations in the connected third order correlation function. These measurements are the first of their kind, and they clearly show how a two-level system interacting with a light field introduces correlations of three photons.

As the superatom is highly unidirectional, it also poses as an interesting candidate for a cascaded quantum system. In this thesis we discuss initial measurements on two atomic ensembles in series. With the alignment achieved so far, compared with the single realization the two superatoms do not behave as well as single two-level systems, and this must be further optimized.

Resumé

I dette specialeforløb har vi bygget en eksperimentel opstilling til at realisere Rydberg superatomer. Opstillingen er blevet implementeret i et eksisterende eksperimentalt setup. Med den nye opstilling har vi undersøgt, hvordan et elektromagnetisk felt med få fotoner interagerer med et enkelt Rydberg superatom.

Opstillingen til at producede et superatom består af en ekstra optisk fælde, der bliver overlappet med en eksisterende optisk fælde. Den vigtigste komponent i opstillingen er en akusto-optisk deflektor, som kan afbøje en laserstråle i adskillige stråler. Dette gør opstillingen meget fleksibel, fordi det er muligt at lave flere optiske fælder samtidig.

Med en enkelt optisk fælde realiserede vi et enkelt Rydberg superatom. Et superatom er et atomensemble, der kollektivt opfører sig som et enkelt atom. Rydberg-superatomer realiseres ved hjælp af Rydberg blokademekanismen. Ved at afgrænse atomensemblet så det er vel indenfor det volumen, der er defineret af en enkelt Rydberg blokaderadius, får man et medium, der kun tillader en enkelt excitation, og som effektivt er et to-levelsystem.

Et Rydberg superatom bestående af N atomer interagerer kollektivt med et drivende elektromagnetisk felt med en interaktionsstyrke, der er forstærket med en faktor $\sqrt{N}$ sammenlignet med interaktionsstyrken for et enkelt atom. På grund af denne forstærkning af interaktionen mellem lys og to-levelsystem interagerer vores Rydberg superatom interagerer med selv felter med meget få fotoner.

Med et Rydberg superatom kan man derfor undersøge interaktionen mellem et to-levelsystem og et kvantiseret lysfelt. Man finder, at systemet ændrer lysfeltet på enkelt-foton niveau, og at dette resulterer i et signal i to-foton-korrelationsfunktionen.

I dette speciale har vi undersøgt hvordan et superatom skaber foton-korrelationer. Her viser vi et signal af korrelation af op til tre fotoner i tredjeordens korrelationsfunktionen, og vi viser et signal af rene trefoton korrelationer i den connectede tredjeordens korrelationsfunktion. Disse målinger er de første af deres slags, og de viser klart hvordan et to-levelsystem, som interagerer med et lysfelt, introducerer korrelationer mellem tre fotoner i feltet.

Fordi Rydberg superatomer også er meget ensrettede i deres emission af lys, er de interessante kandidater for et kvante-kaskadesystem. I dette speciale diskuterer vi de første målinger på to atomensembler i serie. Indtil nu har vi ikke kunne få to superatomer til at opføre sig lige så godt som et to-level system, som et enkelt superatom gør. Fremtidige finjusteringer er derfor nødvendige.

Contents

1 Introduction **1**

2 The Rydberg superatom **3**
- 2.1 The open two-level system . . . 3
- 2.2 Rydberg Physics . . . 7
- 2.3 Superatom . . . 9
  - 2.3.1 Adiabatic elimination . . . 13
- 2.4 Two plus one level system strongly interacting with light . . . 16

3 Experimental realization **21**
- 3.1 Preparation of experiment . . . 21
  - 3.1.1 MOT . . . 21
  - 3.1.2 Optical dipole trap . . . 22
- 3.2 Experimental procedure . . . 24

4 Dimple setup **27**
- 4.1 Setup . . . 28
  - 4.1.1 Laser . . . 29
  - 4.1.2 Objective and telescope . . . 29
  - 4.1.3 Acousto-Optic Deflector . . . 30
- 4.2 Integration in existing setup . . . 32
  - 4.2.1 Alignment in absorption imaging . . . 32
- 4.3 Experiments with a single superatom . . . 36

5 Three-photon correlation **39**
- 5.1 Results . . . 39
  - 5.1.1 Extraction of fit parameters . . . 40
- 5.2 Correlation functions . . . 41
- 5.3 Jacobi coordinates . . . 42
  - 5.3.1 Binning of data points . . . 44
  - 5.3.2 Averaging over R . . . 44
- 5.4 Third order correlation function . . . 46
- 5.5 Connected correlation function . . . 48
  - 5.5.1 Connected third order correlation function . . . 49
  - 5.5.2 Reference pulses . . . 51
  - 5.5.3 Center of mass dependency . . . 51
  - 5.5.4 The origin of three-photon correlations . . . 54

6 Multiple superatoms **57**
6.1 Multiple superatoms 57
6.2 Initial results 59
6.2.1 Ion detection and two photon absorption 59
6.2.2 Ion statistics 61
6.2.3 Ion time traces 63
6.2.4 Outlook for two superatoms 64

7 Conclusion **67**
7.1 Outlook 68

Bibliography **69**

Acknowledgment **73**

Chapter 1

Introduction

Harnessing quantum effects has been proposed as key concept for future technology. This wide-ranging research and development effort has been designated the second quantum revolution [1].

Among the large variety of system under investigation, optical photons play a key role. They have been identified as the ideal carrier of long-distance quantum information, as they do not interact and move with speed of light. Besides information transfer, optical photons can also be used directly for information processing. Here the above points are rather a problem, and one possible solution are engineered interaction between photons, because this enables deterministic on-the-fly processing of photonic qubits[2, 3].

Such nonlinear processes are well known from e.g. frequency doubling or sum-frequency generation and from the nonlinear Kerr-effect. refs The field of quantum nonlinear optics focuses on the regime where interactions between single photons are so strong that the nonlinearity depends on the exact number of photons present [3]. The realization of strongly nonlinear media is an expanding field of research with many different media, but so far only two systems have reached the quantum nonlinear regime. Those are high finess cavities and Rydberg nonlinear medium [4].

The key consept is Rydberg nonlinear optics is the mapping of photons onto atomic states with strong interactions, as the strong dipole-dipole interactions between Rydberg atoms enable the realizationo of highly nonlinear media [5, 4].

Rydberg nonlinear media in free space have many useful applications, and have been used to realized a number of quantum tools such as, single photon sources [6, 7, 8], phase gates and switches [9], transistors [10], CNOT gates [11], single photon absorbers [12], entanglement between photons and entanglement between photons and atoms [13, 14].

Antibunched and bunched photons have been observed in free space Rydberg nonlinear media [8]. The bunching and antibunching are measured with the two photon correlation function, which is a standard measure of how photons interact [15, 16].

The concept of Rydberg superatoms can me used for creating photon-photon interactionn. By employing the Rydberg blockade mechanism, we make an atomic ensemble of N atoms behave collectively as a single two plus one level system [17]. This ensemble, which we call a Rydberg superatom, has a strongly enhanced coupling to the driving field and enhanced emission into the forward mode of our system due to the collective behavior [18]. Therefore, a Rydberg superatom allows investigation of the most fundamental interactions between light and a two level system. In our setup we have previously showed that the collective coupling can become so strong that a Rydberg superatom can modulates the light field on single photon level, and show a strong correlation effects on two photons [12, 19].

In this thesis, the measurements of photon correlations are taken further by analyzing the three-photon correlations mediated by a superatom. Three-photon correlations have recently been observed with propagating Rydberg polaritons [20]. In the scope of this thesis we have shown the first signature of three-photon correlations observed in the connected correlation function. The analysis has lead to a joint publication with theory partners from Universitẗ Stuttgart.

Three-photon correlation measurements are an experimental achievement, in the sense that very high experimental stability is required to keep a high signal to noise ratio on the connected third order correlation function signal which is two orders of magnitude than the two photon correlation signal.

The Rydberg superatom is not only a promising system for high order photon-photon interactions. Due to the unidirectional character of the superatom, which has enhanced emission into the forward mode, and the strong coupling to light the Rydberg superatom can also be a candidate for future cascaded quantum systems [21]. This would be realized with multiple superatoms in series. The initial experimental steps for such a system have been taken within this thesis by realizing two superatoms.

Chapter 2

The Rydberg superatom

In this chapter, the concept of the Rydberg superatom is introduced. The key aspect is to use the Rydberg blockade mechanism to turn an ensemble of identical atoms into a single, effective 2-level quantum emitter. Because of the large number of real atoms involved, the coupling between this superatom and a single photonic mode is strongly enhanced. The chapter in section 2.1 begins with a short introduction to the two-level system coupled to a light field.

In section 2.2 the interaction between Rydberg atoms is introduced, and we discuss the Rydberg blockade mechanism. In section 2.3 we see how the Rydberg blockade can be used to realize a Rydberg superatom. The Rydberg superatom is an ensemble of atoms that experiences a collective enhancement of atom light coupling. Finally, in section 2.4 we introduce a model describing the coupling between a single superatom and a quantized photonic field.

2.1 The open two-level system

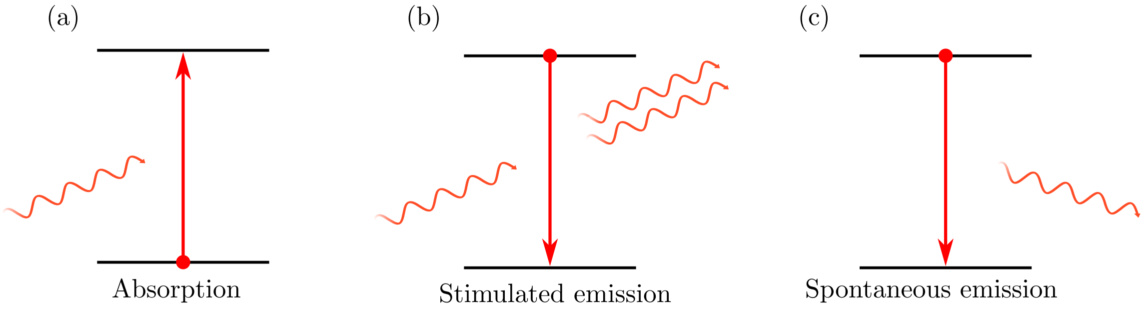

Figure 2.1: Three fundamental processes of a two-level system. **a)** is the absorption of a photon leading to an excitation, **b)** is the decay of the excitation due to stimulated emission of a photon. **c)** is spontaneous emission of a photon.

In this section, the theoretical principles of a two-level system interacting with a photonic field are discussed. As already mentioned, a two-level system coupled to a photonic field is the simplest system which can modulate light. As discussed in most quantum optics textbooks when the interaction between light and a two-level systems is treated, three fundamental processes are typically considered. These processes are illustrated in figure 2.1, and they a) absorption of a photon, raising the two-level system from ground to excited state. b) stimulated emission,

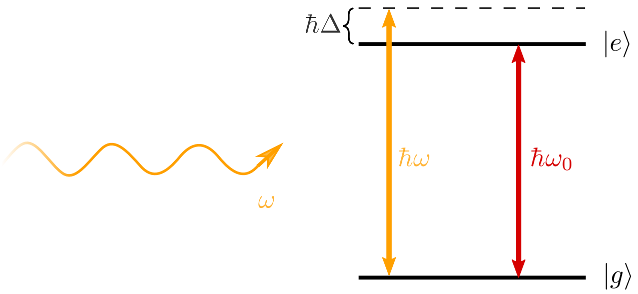

Figure 2.2: Two-level system with ground state $|g\rangle$ and excited state $|e\rangle$. The energy-gap between the two levels is $\hbar\omega_0$. An incoming light field with frequency ω is detuned with $\Delta = \omega_0 - \omega$ with respect to the system resonance frequency.

where an absorbed photon is emitted into the same mode as an incoming, triggering photon, while the two-level system decays is brought from the excited state to the ground state, and c) spontaneous emission, where a photon is spontaneously emitted while the system decays from the excited state to the ground state. The last process is in the simple picture a random process. To describe spontaneous emission, it is necessary to take vacuum fluctuations into account [22].

Because of the spontaneous emission, it is often too complicated to describe the full system, as this will include all possible photon modes [15]. To include the vacuum fluctuations, it is therefore instructive to consider an open quantum system, where the full system is broken into the part of interest and a surrounding environment. The interaction of the system and the environment is treated as a decay term, describing the loss of coherence into the quantum states involving the not described photonic modes.

In the following the time evolution of a two-level system coupled to a photonic field is described by solving a fully coherent master equation. The dissipative dynamics are added in an additional Lindblad term.

First, the situation of an atom in free space interacting with electromagnetic fields in general is considered. The system is illustrated in figure 2.2. The atom is considered to have a ground state $|g\rangle$ and an excited state $|e\rangle$. The levels have an energy difference $\hbar\omega_0$, where $\hbar$ is the reduced Planck constant and ω_0 is the resonance frequency of the system.

The full Hamiltonian for a coupled system is the sum of the Hamiltonians for the atom, the field, and the interactions between atom and field, so that

$$\mathcal{H} = \mathcal{H}_{\text{atom}} + \mathcal{H}_{\text{field}} + \mathcal{H}_{\text{int}}. \tag{2.1.1}$$

The atomic Hamiltonian is given by the energy of each of the two states. Setting the ground state energy to zero yields

$$H_{\text{atom}} = \hbar\omega_0 |e\rangle\langle e|. \tag{2.1.2}$$

As a general field is considered, the field Hamiltonian is an integral over all modes $\mathbf{k}$, where $\mathbf{k}$ contains both the wave vector and one of two orthogonal polarizations,

$$\mathcal{H}_{\text{field}} = \int \mathrm{d}\mathbf{k}\, \hbar\omega_{\mathbf{k}} a^\dagger_{\mathbf{k}} a_{\mathbf{k}}, \tag{2.1.3}$$

where $\omega_{\mathbf{k}}$ is the frequency of the $\mathbf{k}$'th mode, and $a_{\mathbf{k}}$ is the annihilation operator for the $\mathbf{k}$'th mode. When applying to a photon state, $a_{\mathbf{k}}$ removes one photon of the $\mathbf{k}$'th mode. The product $a^\dagger_{\mathbf{k}} a_{\mathbf{k}}$ is the number operator, giving the number of photons in the $\mathbf{k}$'th mode.

To describe the interaction between the uncharged atom and the field, the dipole moment induced in the atom by the field is considered. The dipole operator $\mathbf{d}$ is

$$\mathbf{d} = -e\mathbf{r}, \tag{2.1.4}$$

where e is the elementary charge and $\mathbf{r}$ is the relative position of the electron to the center of mass coordinate of the atom in the case of a single electron. If the atom contains more than one electron, the dipole operator will be the sum over all electrons. For alkali atoms with a single valence electron in an outer orbital, it is a good approximation to assume that only the valence electron is relevant, as the electrons in inner orbitals can be assumed to provide spherically symmetric screening around the nucleus [23, 24]. The dipole term is only the first term in the multipole expansion, but for most cases the higher order terms are negligible.

The Hamiltonian describing the interaction between the two levels and the electric field is

$$\mathcal{H}_{\text{int}} = -\mathbf{d} \cdot \hat{\mathbf{E}}, \tag{2.1.5}$$

where $\hat{\mathbf{E}}$ is the electric field operator. The description of the electric field operator depends on whether a stationary or a traveling field is considered. If the electric field is described as quantized, the field operator will contain creation and annihilation operators of the photonic modes. A quantized field considered in section 2.4.

With these three terms of the Hamiltonian, the behavior of a two-level atom interacting with light can be described. The three fundamental processes in figure 2.1 are all captured by this model.

In principle by combining all three terms of the Hamiltonian, the full time evolution is given by the Liouville-von Neumann equation,

$$\partial_t \rho(t) = -\frac{i}{\hbar}[\mathcal{H}, \rho], \tag{2.1.6}$$

where ρ is the density matrix of the system given by $\rho = \sum_\alpha P_\alpha |\psi_\alpha\rangle\langle\psi_\alpha|$, where $|\psi\rangle$ is the state vector of the system [25].

It is however usually not of interest or not possible to solve the full time evolution for all fields. Therefore, it is instructive to go to the master equation formalism for an open quantum system. In this formalism, the spontaneous decay of the system is taken into account with a single decay term. To see this, the terms in equation 2.1.1 can be renamed to consider the system, that is the atom, the environment, that is the field, and the interaction, so that

$$\mathcal{H} = \mathcal{H}_{\text{s}} + \mathcal{H}_{\text{env}} + \mathcal{H}_{\text{int}}. \tag{2.1.7}$$

Here the three separated Hamiltonians govern the system, the environment and the system-environment interaction respectively. In most situations, the full environment is not of interest or cannot be solved or known.

Therefore, the terms considering the environment is transformed out of equation 2.1.7 by taking the partial trace of the density matrix. Thereby information about the degrees of freedom of the environment are lost. Since the Hamiltonian describing the system-environment interaction will thus lose information of how the system affects the environment, and it can be reduced to containing the term describing spontaneous decay, $\sigma_{ge} = |g\rangle\langle e|$, from the excited state to the ground state.

Here the time evolution of the system is treated on its own, while the interaction with the environment is handled by a second term. Thus the master equation of the system is

$$\partial_t \rho_s = -\frac{i}{\hbar}[\mathcal{H}_s, \rho_s] + \Gamma \mathcal{L}(\sigma_{ge})\rho_s, \tag{2.1.8}$$

where Γ is a decay term which handles decay of the system due to the environment, and $\mathcal{L}$ is the Lindblad superoperator. The Lindblad superoperator working on an operator A is defined as

$$\mathcal{L}(A)\rho_s = A\rho_s A^\dagger - \frac{1}{2}\left\{A^\dagger A, \rho_s\right\}. \tag{2.1.9}$$

The first term of equation 2.1.8 accounts for the coherent behavior of the system, while the second term of the master equation containing the Lindblad operator is dissipative.

The master equation is only valid on timescales much longer than the timescale of the system-environment interaction, as this formalism assumes a stationary environment, and that the coupling between the system and environment is a fluctuation around a zero mean. This holds for interactions between a two-level atom and the general electromagnetic fields [26].

Now the situation where the system is driven by a classical field is considered. The driving field is assumed to be a traveling wave with frequency ω, as drawn in figure 2.2. It can be described with

$$\mathbf{E}(\mathbf{r}, t) = \mathcal{E}_0 \mathbf{e}_p \cdot \cos(\omega t - \mathbf{k}\cdot\mathbf{r}), \tag{2.1.10}$$

where $\mathcal{E}_0$ is the field amplitude and $\mathbf{e}_p$ is the field polarization.

For a two-level system, where the wavefunction is

$$|\psi_s\rangle = c_g(t)|g\rangle + c_e(t)|e\rangle, \tag{2.1.11}$$

the density matrix becomes

$$\rho_s = \begin{pmatrix} \rho_{gg} & \rho_{ge} \\ \rho_{eg} & \rho_{ee} \end{pmatrix} = \begin{pmatrix} |c_g(t)|^2 & c_g(t)c_e^*(t) \\ c_e c_g^*(t) & |c_e(t)|^2 \end{pmatrix}. \tag{2.1.12}$$

The diagonal elements describe the populations of the states, while the off-diagonal elements describe the coherences of the system.

The interaction between the driving field and the atom is given by the same expression as in equation 2.1.5, but in the semiclassical treatment the atom is treated quantum mechanically while the driving field is considered a classical vector field,

$$\mathcal{H}_{\text{int}}^{\text{semiClas}} = -\hat{\mathbf{d}}\cdot\mathbf{E}. \tag{2.1.13}$$

The dipole operator can also be written on matrix form, considering the elements of the atomic matrix of equation 2.1.11. There are no entries for the diagonal part of the dipole operator matrix, as the dipole operator depends on $\mathbf{r}$, which is odd. Evaluating the probability of a dipole transition from a state to itself will give zero. Thus, the dipole operator is

$$\hat{\mathbf{d}} = \bar{d}(|e\rangle\langle g| + |g\rangle\langle e|), \tag{2.1.14}$$

where $\bar{d}$ is the expectation value of $\mathbf{d}$, and $|e\rangle\langle g|$, $|g\rangle\langle e|$ are the off-diagonal elements of the system density matrix. With the classical field description, the total Hamiltonian of the system is

$$\mathcal{H} = \mathcal{H}_{\text{atom}} + \mathcal{H}_{\text{int}}^{\text{semiClas}}. \tag{2.1.15}$$

Transforming to the rotating frame, where the reference frame of the system is rotating with the phase of the light, and using the rotating wave approximation to omit fast rotating terms, the Hamiltonian can be written in the form

$$\mathcal{H} = \frac{\hbar}{2}\begin{pmatrix} 0 & \Omega \\ \Omega & 2\Delta \end{pmatrix}, \tag{2.1.16}$$

where Δ is the detuning between the light field frequency ω and the two-level system resonance frequency ω_0, $\Delta = \omega - \omega_0$. Ω is the Rabi frequency of the system, which is an expression for the interaction between the field and the two-level system and describes the coupling strength between the levels. The Rabi frequency is given by

$$\Omega = -\frac{\mathcal{E}_0 \hat{\mathbf{d}} \cdot \mathbf{E}}{\hbar}. \tag{2.1.17}$$

The Lindblad superoperator term is

$$\Gamma \mathcal{L}(\sigma_{ge})\rho_s = \frac{\hbar}{2} \begin{pmatrix} 2\Gamma\rho_{ee} & \Gamma\rho_{ge} \\ -\Gamma\rho_{eg} & -\Gamma 2\rho_{gg} \end{pmatrix}. \tag{2.1.18}$$

The diagonal entries correspond to the decay of population from the excited state to the ground state. The signs reveal that the population in the excited state decreases, while the population in the ground state increases. The off-diagonal element describes the decay of the coherences in the system.

Substituting equation 2.1.16 and equation 2.1.18 into equation 2.1.8 leads to four coupled differential equations for the components of the system density matrix. This set of differential equations are known as optical Bloch equations,

$$\partial_t \rho_{ee} = i\frac{\Omega}{2}(\rho_{eg} - \rho_{ge}) - \Gamma \rho_e e, \tag{2.1.19}$$

$$\partial_t \rho_{gg} = -i\frac{\Omega}{2}(\rho_{eg} - \rho_{ge}) - \Gamma \rho_e e, \tag{2.1.20}$$

$$\partial_t \rho_{ge} = -i\frac{\Omega}{2}(\rho_{ee} - \rho_{gg}) - (\Gamma - i\Delta)\, \rho_e g, \tag{2.1.21}$$

$$\partial_t \rho_{eg} = i\frac{\Omega}{2}(\rho_{ee} - \rho_{gg}) - (\Gamma + i\Delta)\, \rho_g e. \tag{2.1.22}$$

These equations describe the populations in the two states respectively, which follows from the diagonal elements of the density matrix.

What is observed is oscillations in the populations which dampen out over time. When $\Delta = 0$ the oscillation frequency is given by the Rabi frequency, Ω and the damping is given by Γ. Both the Rabi frequency and the damping contains the coupling between the atom and the light [26, 27]. Figure 2.3 shows solutions to the two-level system. Figure 2.3 a) shows the oscillations of the undamped system, whereas figure 2.3 b) shows oscillations for a damped system with $\Delta = 0$. In the damped system the oscillations damp to a steady state value.

2.2 Rydberg Physics

Rydberg atoms are atoms with a single electron excited to a state with large principle quantum number n. Compared to ground state atoms, the key properties of Rydberg atoms, such as lifetime and size, are extremely large [23]. One important aspect for our experiments is the resulting long-range interaction between Rydberg atoms.

Due to the spatially large distribution of the wave function of the highly excited electron, which scales as n^2 [23], the atoms are very prone to get induced dipole moments, and as a consequence they are very sensitive to electric and magnetic fields. The interaction between Rydberg atoms can be calculated with a multipole expansion for distances larger than the Le Roy radius R_{LR} [28]. For distances smaller than R_{LR}, it becomes necessary to take into account that the wave functions of the Rydberg atoms start to overlap. For S-states, at large distances,

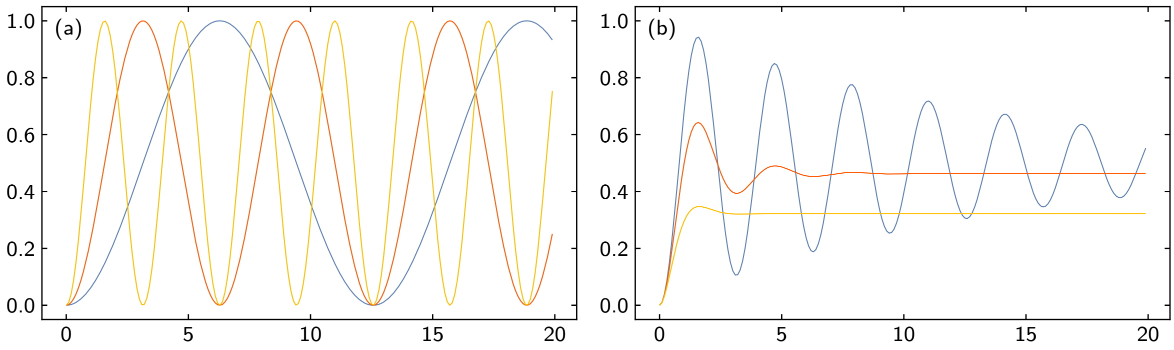

Figure 2.3: Rabi oscillations illustrated. **a** Rabi oscillations in driven two level system with $\Gamma = 0$. The oscillations continue forever when spontaneous decay is not taken into account. The lines show different values of Ω. Blue is $\Omega = 2$, orange is $\Omega = 1$, and yellow is $\Omega = 0.5$. **b)** Rabi oscillations with decay. All lines are for $\Omega = 0.5, \Delta = 0$. Blue line is for $\Gamma = 0.1$, orange for $\Gamma = 0.5$, and yellow for $\Gamma = 1$.

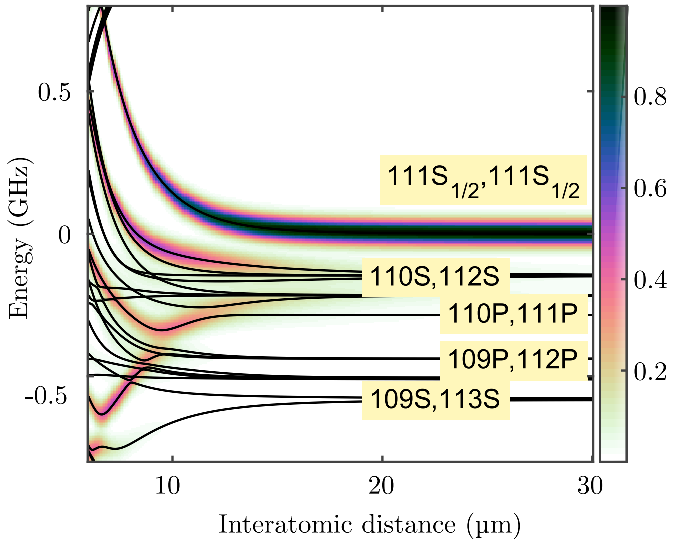

Figure 2.4: Interaction between Rydberg atoms. Potential curve for Rydberg states with the interaction between Rydberg states around $|111S_{1/2}, m_j = 1/2\rangle$. It is seen that the $|111S_{1/2}, m_j = 1/2\rangle$-$|111S_{1/2}, m_j = 1/2\rangle$ interaction goes as $1/r^6$, whereas other states have different behaviours at small distances. The colorcoding shows the overlap of the state of interest with nearby states. Thus the colors show the admixture of the $|111S_{1/2}, m_j = 1/2\rangle$ pair state in other states.

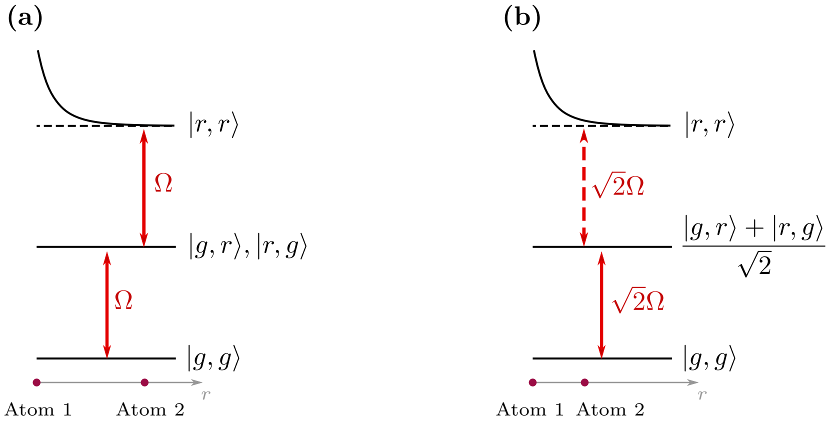

Figure 2.5: Rydberg level schemes. **a)** Excitation of two Rydberg atoms is allowed if the distance between them is sufficiently large. **b)** Within the blockade radius, the energy of a second Rydberg excitation is shifted out of resonance.

the interaction can be assumed to be well described by Van der Waals interactions, such that that $U \propto {}^{C_6}/_{r^6}$.

Figure 2.6 c) shows the potential curve for different Rydberg states interacting with the $|111S_{1/2}, m_j = 1/2\rangle$ state as calculated with the *Pair Interaction* software [28]. The $|111S_{1/2}, m_j = 1/2\rangle$ Rydberg state is chosen as this is the state used for the data presented in this thesis.

A key consequence of the strong interaction is the so-called Rydberg blockade. A Rydberg excitation will cause a modulation of the energy levels of the atoms in the immediate vicinity [11, 29]. This shift of energy levels effectively blocks further excitation of close by atoms to the same level as this transition is no longer resonant with the driving field. The energy potential for different Rydberg state interactions is shown in figure 2.4.

The blockade caused by the Van der Waals interaction is described with a blockade radius,

$$r_\mathrm{b} = \sqrt[6]{\frac{c_6}{\hbar\Omega}}. \tag{2.2.1}$$

Within the blockade sphere with this radius, only one atom can be excited by a monochromatic field driving the transition with Rabi frequency Ω, to a state with Van der Waals coefficient c_6. This is what is illustrated in figure 2.6 a) and b). In figure 2.6 a), the two atoms are spaced with a distance greater than the blockade radius, while in figure 2.6 b), the interatomic spacing is smaller than the blockade radius, and the second atom therefore experiences a level shift as shown with the curved line. The blockade effect allows ensembles much larger than optical wavelengths to behave in a collective fashion, and this is the key to the strong nonlinear behavior of Rydberg atomic media [7, 30] and to enhancing the coupling between atoms and driving field, allowing a meaningful Ω for a driving field with few photons [31].

2.3 Superatom

The Rydberg superatom is one of many applications of the Rydberg blockade mechanism. A superatom is an ensemble of multiple atoms, which behaves as a single atom. A Rydberg superatom can be realized by confining an atomic ensemble entirely within a volume limited to one blockade radius [32]. Single Rydberg superatoms have been realized, and the superatom

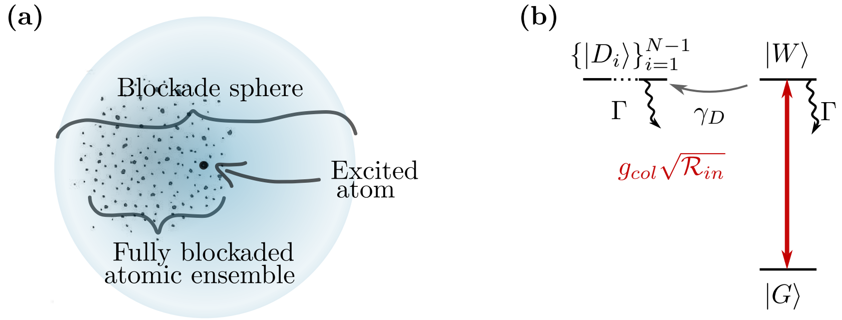

Figure 2.6: Rydberg superatom. **a)** An atomic ensemble is fully within the volume defined by one blockade radius, and thus they all experience the Rydberg blockade when one atom is excited to a Rydberg state. **b)** Level diagram showing the collective states; the collective ground state $|G\rangle$, the bright state, $|W\rangle$, which is a symmetric superposition of the states where one atom is excited to a Rydberg level, and the manifold of dark states, $\{|D_i\rangle\}_{i=1}^{N-1}$. The dark states are only accessed through dephasing. For a sufficiently large number of atoms in the ensemble, the dephasing from the excited state into the dark states can be treated with a decay rate, γ_D.

interaction with weak photonic fields has been investigated [33, 7, 12, 19]. In the scope of this thesis, the framework of the previous investigations has been extended to study correlations between three photons Something on arxiv?.

A Rydberg superatom is effectively a zero-dimensional system, as all the atoms are blockaded by any possible Rydberg excitation. Thus, the position of the Rydberg excitation does not have an influence on the collective behavior of the system.

An ensemble of $N \gg 1$ atoms can exhibit a complex dynamic behavior leading to superradiance [31]. To see the dynamics of such an ensemble of atoms within the blockade sphere, we consider N two-level atoms each with a ground state, $|g\rangle$, and an excited Rydberg state $|r\rangle$. Using this description as basis, the first state is $|g\rangle, |r_1\rangle$, where $|r_i\rangle$ corresponds to the i'th atom being excited to the Rydberg state.

Instead of this basis describing the state of the individual atoms, a collective basis can be defined. The ground state of the collective basis for N atoms is trivially the state where all atoms are in the ground state, $|G\rangle = |g_1, g_2, \cdots, g_i, \cdots, g_N\rangle$ [18]). To find the collective excited state, it is instructive to consider the time evolution of the ground state.

The Hamiltonian handling interactions between a plane wave electromagnetic field and an atomic ensemble is the sum of the operators for a single atom [18]. For a system with N atoms with two levels, the interaction is given by

$$\mathcal{H}_{\text{int}} = \hbar g_0 \sum_{j=1}^{N} \left(\sigma_j^\dagger a_{\mathbf{k}_0} \mathrm{e}^{i\mathbf{k}_0 \cdot \mathbf{r}_j} \mathrm{e}^{-i(\omega-\omega_0)t} + \sigma_j a_{\mathbf{k}_0}^\dagger \mathrm{e}^{-i\mathbf{k}_0 \cdot \mathbf{r}_j} \mathrm{e}^{i(\omega-\omega_0)t} \right). \tag{2.3.1}$$

where $\sigma_j, \sigma_j^\dagger$ are operators for the j'th atom, bringing this specific atom from the excited state to the ground state or from the ground state to the excited state respectively. The photons are handled by the annihilation and creation operators, $a_{\mathbf{k}_0}, a_{\mathbf{k}_0}^\dagger$, which acts on photons in the $\mathbf{k}_0$ mode with frequency $\omega = c|\mathbf{k}_0|$. In this interaction Hamiltonian, the driving field is already considered to be quantized, as it will further be discussed in section 2.4.

Comparing the interaction Hamiltonian of equation 2.3.1 to the interaction Hamiltonian of section 2.1, equation 2.1.13, it is clear that the dipole operator from equation 2.1.13, given by equation 2.1.14, will be a sum over all atoms where all terms includes a phase factor handling the position of the specific atom.

$$\hat{d}_N = \bar{d}\sum_{j=1}^{N}(\sigma_j^\dagger \mathrm{e}^{i\mathbf{k}_0\cdot\mathbf{r}_j} + \sigma_j \mathrm{e}^{-i\mathbf{k}_0\cdot\mathbf{r}_j}) = \sum_{j=1}^{N}\hat{d}_j. \tag{2.3.2}$$

Here $\hat{d}_N$ is the full dipole operator working on the full system, and d_j is the dipole matrix element of the j'th atom. Again, $\bar{d}$ is the expectation value of the dipole operator.

In the case of the excited state being a Rydberg state, the interactions between Rydberg atoms must also be included, yielding the interaction term

$$\mathcal{H}_{\text{int}} = \hbar g_0 \sum_{j=1}^{N}\left(\sigma_j^\dagger a_{\mathbf{k}_0}\mathrm{e}^{i\mathbf{k}_0\cdot\mathbf{r}}\mathrm{e}^{-i(\omega-\omega_0)t} + \sigma_j a_{\mathbf{k}_0}^\dagger \mathrm{e}^{-i\mathbf{k}_0\cdot\mathbf{r}}\mathrm{e}^{i(\omega-\omega_0)t}\right) + \frac{1}{2}\sum_{j\neq i}^{N} V_{i,j}\sigma_j^\dagger\sigma_j\sigma_i^\dagger\sigma_i. \tag{2.3.3}$$

Here $V_{i,j}$ is the potential that governs Rydberg-Rydberg interactions [34**?**]. This potential is given by the multipole expansion of the interatomic interactions. Thus, when only the dipole term is relevant, $V_{i,j}$ will be the Van der Waals term discussed above. This potential is only relevant when two Rydberg excitations are present. When the potential is much greater than the atom-light coupling, it corresponds to the blockade situation, as the first term of equation 2.3.3 can create a single operator. The second term however will cause an energy shift of states containing two excitation, shifting these states out of resonance.

The unitary time evolution of the system is described by [18]

$$\begin{aligned} U(\tau) &= \mathcal{T}\mathrm{e}^{-(i/\hbar)\int_0^\tau \mathrm{d}t'\,V(t')} && (2.3.4)\\ &\simeq 1 - ig_0\int_{t_0}^{\tau}\mathrm{d}t'\sum_{j=1}^{N}\left(\sigma_j^\dagger a_{\mathbf{k}_0}\mathrm{e}^{i\mathbf{k}_0\cdot\mathbf{r}}\mathrm{e}^{-i(\omega-\omega_0)t} + \sigma_j a_{\mathbf{k}_0}^\dagger\mathrm{e}^{-i\mathbf{k}_0\cdot\mathbf{r}}\mathrm{e}^{i(\omega-\omega_0)t}\right) && (2.3.5)\end{aligned}$$

where $\mathcal{T}$ is time ordering operator. The approximation to first order is made under the assumption that the interaction strength of a single atom with the field, g_0 is small.

Applying this unitary operator to the initial state with one photon in the system in mode $\mathbf{k}_0$ yields

$$U(\tau)|G\rangle|1_{\mathbf{k}_0}\rangle \simeq |G\rangle|1_{\mathbf{k}_0}\rangle - ig_0\tau\sum_{j=1}^{N}\mathrm{e}^{i\mathbf{k}_0\cdot\mathbf{r}}|g_1, g_2, \cdots, r_j, \cdots, g_N\rangle|0\rangle \tag{2.3.6}$$

The subtracted state is then an expression for the excited state. This state is normalized by a factor of $\sqrt{1/N}$ to give the excited state

$$|W\rangle = \frac{1}{\sqrt{N}}\sum_{j=1}^{N}e^{i\mathbf{k}_0\cdot\mathbf{x_j}}|j\rangle, \tag{2.3.7}$$

where $|j\rangle$ is the symmetric linear combination of states where the j'th atom is excited to $|r\rangle$ and all other atoms are in the ground state $|g\rangle$. $|W\rangle$ is called the bright state, as it interacts with the light.

What is important to note in equations 2.3.6 and 2.3.7 is how the photon causing the excitation to the bright state remains in the bright state vector as a phase factor.

The excitation from the ground to the excited state by absorption of one photon is calculated by

$$\langle 0|\langle W|V(t)|G\rangle|1_{\mathbf{k}_0}\rangle = \frac{N}{\sqrt{N}}\langle 0|\langle r|V(t)|g\rangle|1_{\mathbf{k}_0}\rangle = \sqrt{N}\langle 0|\langle r|V(t)|g\rangle|1_{\mathbf{k}_0}\rangle. \tag{2.3.8}$$

The transition of the collective system between ground and excited state is enhanced by $\sqrt{N}$ compared to the single atom transition.

This is a general observation. For a system with a single allowed excitation collective Rabi oscillations arises. The collective Rabi frequency of the oscillations will be enhanced from the one atom effective Rabi frequency Ω_{eff} to $\sqrt{N}\Omega_{eff}$ [5, 33, 31]. For the situation of just two atoms an increase of the Rabi frequency of $\sqrt{2}$ has been observed [29].

The decay from the collective excited state given by equation 2.3.7 can also be considered. Assuming no photons in the field, the time evolution can be described in the same way as in equation 2.3.6. The time evolution operator is given by [18, 15]

$$U_W(t) = \sum_j U_W^{(j)} = \sum_j \gamma_j^\dagger \sigma_j, \tag{2.3.9}$$

$$\gamma_j^\dagger = \sum_{\mathbf{k}} \frac{g_{\mathbf{k}} \mathrm{e}^{-i\mathbf{k}\cdot\mathbf{r}_j}}{\omega_{\mathbf{k}} - \omega_0 + \frac{i}{2}\gamma}, \tag{2.3.10}$$

where $\omega_{\mathbf{k}}$ is the frequency of photons in the $\mathbf{k}$'th mode, $\gamma_j^\dagger$ is the radiation operator, creating a photon in the $\mathbf{k}$'th mode from the j'th atom. γ and in the radiation operator is the spontaneous emission rate from the Weisskopf-Wigner approximation [15]. σ is the annihilation operator of the j'th atom, bringing this specific atom from $|r\rangle$ to $|e\rangle$.

In equation 2.3.11 the spontaneous decay is treated in the Wigner Weisskopf formalism, and not as in the master equation formalism, as in equation 2.1.8.

With this time evolution operator of equation 2.3.9, the evolution of the state $|W\rangle|0\rangle$ is

$$\langle G|U_W(t)|W\rangle|0\rangle = \frac{1}{\sqrt{N}} \sum_j \mathrm{e}^{-i\mathbf{k}_0\cdot\mathbf{r}_j} \gamma_j^\dagger |0\rangle = \frac{1}{\sqrt{N}} \sum_{\mathbf{k}} \frac{g_{\mathbf{k}}}{\omega_{\mathbf{k}} - \omega_0 + \frac{i}{2}\gamma} |1_{\mathbf{k}}\rangle \sum_j \mathrm{e}^{i(\mathbf{k}_0 - \mathbf{k})\cdot\mathbf{r}_j}. \tag{2.3.11}$$

The final sum in equation 2.3.6 can, under the assumption that the density of atoms is high enough to be assumed continuous, be approximated by an integral over the volume of the medium [18],

$$\sum_j \mathrm{e}^{i(\mathbf{k}_0 - \mathbf{k})\cdot\mathbf{r}_j} \approx \frac{N}{V} \int_v \mathrm{d}^3\mathbf{r}\, \mathrm{e}^{i(\mathbf{k}_0 - \mathbf{k})\cdot\mathbf{r}_j} = \frac{N}{V} (2\pi)^3 \deg^{(3)}(\mathbf{k}_0 - \mathbf{k}). \tag{2.3.12}$$

With this approximation, equation 2.3.6 becomes

$$\langle G|U_W(t)|W\rangle|0\rangle = \frac{\sqrt{N}}{V} \sum_{\mathbf{k}} \frac{g_{\mathbf{k}}}{\omega_{\mathbf{k}} - \omega_0 + \frac{i}{2}\gamma} \delta^{(3)}(\mathbf{k}_0 - \mathbf{k}) |1_{\mathbf{k}}\rangle. \tag{2.3.13}$$

From equation 2.3.13, it is clear that the spontaneously emitted photon is emitted into the same direction as the photon which was initially absorbed to excite the system [18]. This is a key element which underlines the relevance of the superatom. Not only is the collective system coupling to the driving field by a factor of $\sqrt{N}$, the system also preferentially emits back into the $\mathbf{k}_0$-mode, which is the mode of the driving field. It should also be noted, that just as the coherent coupling to the field is enhanced by a factor of $\sqrt{N}$, so is the collective decay rate.

Apart from the ground state and the excited state, the system also features a collection of $N - 1$ collective dark states, given by the remaining asymmetric linear combinations of $|j\rangle_{j=1}^N$,

$$|D\rangle = \sum_{j=1}^N \alpha_j |j\rangle, \tag{2.3.14}$$

where α contains the normalization and the phase factor. The collection of dark states are denoted $\{D\}_{i=1}^{N}$.

Since the dark states are the remaining linear combinations, they must all be orthonormal to the bright state, so that

$$0 = \langle W|D\rangle = \frac{1}{\sqrt{N}} \sum_{j=1}^{N} \sum_{l=1}^{N} \langle j|l\rangle \alpha_l \mathrm{e}^{-i\mathbf{k_0}\cdot\mathbf{r_j}} = \frac{1}{\sqrt{N}} \sum_{j=1}^{N} \alpha_j \mathrm{e}^{-i\mathbf{k_0}\cdot\mathbf{r_j}}. \tag{2.3.15}$$

The interaction between a dark state and the ground state is given by

$$\langle G|\hat{d}_N|D\rangle = \sum_{j=1}^{N} \langle G|\hat{d}_N|j\rangle \alpha_j \tag{2.3.16}$$

$$= \sum_{j=1}^{N} \langle g|\hat{d}_j|j\rangle \alpha_j = 0. \tag{2.3.17}$$

The last equality in equation 2.3.17 follows from $\langle g|\hat{d}|j\rangle$ being independent of j [35]. Here the dipole operator could have been substituted with the full interaction operator from equation 2.3.3, but the final result would not have been different.

With the ground state orthogonal to all dark states, it is clear why they are called dark: There is no allowed transition from the ground state to the dark states involving the light field. Without the interaction with the light, it is on one hand not possible to excite an atom to a dark state by the light field, but on the other hand it is not possible to have stimulated decay from the dark states, this decay can only be spontaneous, i.e. dissipative. An important point is that the decay of the dark states is neither directional nor enhanced by collective effects. The dark states decay as single atoms decay rather than as an ensemble.

The collection of dark states can be treated as a single third level, yielding a system of three states, but where one state can only be accessed by dephasing. Therefore, this system will be called a two plus one system.

The transition from the bright state into a dark state can be described for each dark state, but in the case of $1 \gg N$, the collection of dark states can also be treated as a single level to which the bright state can decay with rate γ [17].

Also, though the dark states are orthogonal to the bright state, they still contain one Rydberg excitation and thereby block the medium. Thus dephasing from the bright state into the manifold of dark states accounts for a main damping mechanism in the system. The dephasing into the dark states is caused by for finite laser linewidth, thermal motion and collisions between atoms and describes the loss of coherence in the system.

This extra degree of freedom in the system in the form of a third level allows a range of effects that cannot take place in a true two-level system. Among these effects is the realization of a single photon absorber, where the dephasing to dark states are exploited to make an absorbed photon inaccessible for stimulated emission while keeping the medium transparent to subsequent photons [12, 17].

2.3.1 Adiabatic elimination

In order to achieve a Rydberg state of long lifetime, it is common to have a transition from the ground state to the Rydberg state via an intermediate state in a scheme involving at least two different driving fields. Such a setup is shown in figure 2.7 a). Here the two fields drive the

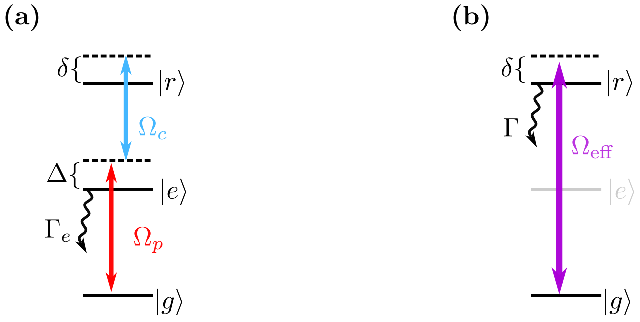

Figure 2.7: Adiabatic elimination. **a)** Level scheme for one atom. The red probe light drives the transition from ground state $|g\rangle$ to the intermediate state $|e\rangle$ with Rabi frequency Ω_p. It is detuned from resonance of the intermediate state with Δ. The blue control light drives the transition from the intermediate state to the excited state $|r\rangle$ with Rabi frequency Ω_c. The probe light is detuned with $\delta - \Delta$. The intermediate state decays with Γ_e. **b)** Collective level schemes. By detuning the two driving fields far off intermediate state resonance, $\Delta / ll \Gamma_e$, the intermediate state can be adiabatically eliminated. The system can then be treated as a two-level system driven by an effective Rabi frequency Ω_{eff}.

transition with Rabi frequencies Ω_p and Ω_c. The detuning from intermediate state resonance is Δ, and the detuning from two photon reonance is δ. Depending on how these detunings are chosen, a number of different regimes with different characteristics can be reached.

For the range of detunings where both fields are relatively close to their respective transition resonances and where the medium can be considered a three-level system the medium can accommodate the mapping of incoming photons to polaritons, which are quasi particles of dipolar excitations propagating through the medium. The interactions between the polaritons as they propagate through the medium is imprinted on the photons which leaves the medium. Thus, the medium facilitates photon-photon interactions [30].

With both fields on resonance, electromagnetically induced transparency (EIT) is reached, causing a medium which is otherwise opaque to be transparent. At this resonance, two polaritons cannot be closer than the blockade radius. This can results in antibunched photons [8].

Keeping the sum of the field frequencies close to two photon resonance, $\delta \approx 0$ but detuning both of them from the intermediate state resonance, $|\Delta| > \Gamma_R, \Gamma_e$, the behavior of the system will change, leading to a variety of different interactions between the polaritons.

Going further off resonance leads to a regime where the intermediate state can be neglected, as it can be assumed to be in equilibrium at any given time, permitting it to be treated as constant.

In the setup described here, Rydberg levels are accessed from the ground state through an intermediate state. This is seen in figure 2.7 a) where a weak (red) probe field and a strong (blue) control field excite an atom from the ground state, $|g\rangle$, to an intermediate state, $|e\rangle$, and from the excited state to the Rydberg state, $|r\rangle$, respectively.

The ground state and the Rydberg state are here both S-states, while the intermediate state is a P-state, meaning that the direct transition $|g\rangle \leftrightarrow |r\rangle$ is dipole forbidden, while the transitions through the intermediate state $|g\rangle \leftrightarrow |e\rangle$ and $|e\rangle \leftrightarrow |r\rangle$ are dipole allowed.

These transitions have Rabi frequencies Ω_p for the probe transition $|g\rangle \leftrightarrow |e\rangle$ and Ω for the control transition $|e\rangle \leftrightarrow |r\rangle$ respectively. Ω_p is given by $g_0\sqrt{\mathcal{R}_{\text{in}}}$, where $\mathcal{R}_{\text{in}}$ is the incoming photon rate and g_0 is the coupling between the light field and a single atom. Ω is given by a similar expression, but is not of same interest as Ω_p, as $\mathcal{R}_{\text{in}}$ for the probe is on the order of tenths of photons per micro second, while the strong control light can be treated as a completely classical light field.

Writing the Hamiltonian which describes the interactions between light and atoms in the rotating frame allows all energies to be expressed as detuning from the relevant transitions. For detunings Δ off δ for the control respectively, the Hamiltonian is

$$\mathcal{H} = \frac{\hbar}{2}\begin{pmatrix} 0 & \Omega_p & 0 \\ \Omega_p & 2\Delta & \Omega \\ 0 & \Omega & 2(\Delta-\delta) \end{pmatrix}. \tag{2.3.18}$$

Here the rotating wave approximation has been applied, so that fast rotating terms are neglected.

The diagonal elements of the Hamiltonian describe the energy associated with each state, while the off-diagonal elements describe the energy of the dipole coupling between the states. Thus, the transition from ground state to intermediate state is driven by Ω_p, while the same is true from the stimulated decay back from the intermediate state.

For a system with the Hamiltonian described in equation 2.3.18, the wavefunction is

$$\Psi(t) = c_g(t)|g\rangle + c_e(t)|e\rangle + c_r(t)|r\rangle, \tag{2.3.19}$$

where the states $|g\rangle, |e\rangle, |r\rangle$ are time independent and the probability amplitudes $c_g(t), c_e(t), c_r(t)$ includes all information about time dependence and phase of the states.

With the Hamiltonian given in 2.3.18, this yields three coupled differential equations describing the time evolution of the system.

$$i\partial_t c_g = \frac{\Omega_p}{2}c_e(t), \tag{2.3.20}$$

$$i\partial_t c_e = \Delta c_e(t) + \frac{1}{2}(\Omega c_r(t) + \Omega_p c_g(t)), \tag{2.3.21}$$

$$i\partial_t c_r = (\Delta-\delta)c_r(t) + \frac{\Omega}{2}c_e(t). \tag{2.3.22}$$

In the case where the detuning from the intermediate state, Δ is large, so that $\Omega_p, \Omega \ll \Delta$ but the detuning from the two photon resonance is δ is small, $c_e(t)$ is always well in equilibrium compared to the two other parameters with much slower dynamics. This is due to $\partial_t c_e(t)$ depending on the very large Δ. Hence c_e will to first order be constant, and setting $\partial_t c_e(t) = 0$ yields

$$c_e(t) = -\frac{(\Omega c_r(t) + \Omega_p c_g(t))}{2\Delta}. \tag{2.3.23}$$

The time evolution of $c_g(t)$ and $c_r(t)$ then becomes

$$i\partial_t c_g(t) = -\frac{|\Omega_p|^2}{4\Delta}c_g(t) - \frac{\Omega_p\Omega}{4\Delta}c_r(t) \tag{2.3.24}$$

$$i\partial_t c_r(t) = -\frac{\Omega_p\Omega}{4\Delta}c_g(t) - \frac{|\Omega|^2}{4\Delta}c_r(t) + (\Delta-\delta)c_r(t). \tag{2.3.25}$$

These equations also governs the dynamics of a two-level system. The driving field then has the effective Rabi frequency

$$\Omega_{\text{eff}} = \frac{\Omega\Omega_p}{2\Delta}. \tag{2.3.26}$$

Neglecting the intermediate state on the assumption that it is always in equilibrium is called adiabatic elimination [36, 26]. The adiabatic elimination of the intermediate state is only an approximation. For the system described in this thesis, the intermediate state cannot be fully neglected. Though the population is suppressed by the large detuning Δ, the intermediate state still offers a decay channel for the Rydberg state. Thus there will be spontaneous Raman decay via the intermediate state $|e\rangle$ with decay rate given by

$$\Gamma = \frac{\Omega^2}{(2\Delta)^2}\Gamma_e, \tag{2.3.27}$$

where Γ_e is the decay rate of the intermediate state [26]. This means that for the effective two-level system, the decay of the excited Rydberg state depends on the decay of the intermediate state.

2.4 Two plus one level system strongly interacting with light

To investigate how the superatom affects the electric field, the space and time dependence of this must be expressed. With the time dependent electric field and the density matrix elements, the dynamics of the two plus one system interacting with the field can be described. In chapter 5 the model of the interaction derived below is compared to the experimental results.

As described above, the superatom behaves as a single two plus one level system. The dynamics of this system can now be described with a model. The model is described in the master thesis of Christoph Braun [37] and in [19]. The model was developed by Jan Kumlin and Hans Peter Büchler from Universität Stuttgart.

This model is an extension of the one described in section 2.1. The main difference is the treatment of the driving electric field, which here is treated quantum mechanically. Further, due to the two-level system now being a superatom, the coupling to the light field is strongly enhanced for a specific mode, namely the Gaussian mode defined by the probe beam. The coupling to all other modes is well described by the spontaneous decay term as introduced in section 2.1. This makes our system identical to a waveguide system, where the coupling to a single (waveguide) mode is strongly enhanced through the confinement of the light. An important aspect both of our free-space system and waveguide systems is that the strongly coupled mode is a traveling wave, in contrast to cavity quantum electro-dynamics, where this is a stationary mode.

The Hamiltonian of the field, atom and field-atom interaction with the two plus one level superatom placed at $x = 0$ is given by

$$\mathcal{H} = \frac{1}{2\pi}\int \mathrm{d}\mathbf{k}\, \hbar c \mathbf{k} a^\dagger_{\mathbf{k}}(t) a_{\mathbf{k}}(t) + \hbar\sqrt{\kappa}\left(E(0,t)\sigma^\dagger_{GW} + \sigma_{GW}E^\dagger(0,t)\right). \tag{2.4.1}$$

Where $\sigma_{GW} = |G\rangle\langle W|$ is the transition operator bringing an atom from the excited state to the ground state. The coupling strength is given by $\sqrt{\kappa} = g_{col}/2$.

This Hamiltonian is the same as in section 2.1, except that the atomic part is not written out, as atomic part vanishes in the rotating frame for $\Delta = 0$. The Hamiltonian then contains the energy of the field in the first term, and the interaction between the field and the atom as the second term.

The traveling quantized electric field for all modes is

$$E(x,t) = \frac{\sqrt{c}}{2\pi}\int_{-\infty}^{\infty} \mathrm{d}\mathbf{k}\, \mathrm{e}^{i\mathbf{k}\cdot\mathbf{x}} a_k(t). \tag{2.4.2}$$

Here $a_{\mathbf{k}}$ is the annihilation operator for a photon in the $\mathbf{k}$'th mode. In order to see how the electric field evolves in time as it interacts with the superatom, it is necessary to find the time dependence of the annihilation operator, and the expectation values of the atomic operators. The annihilation operator follows from the Heisenberg equation of motion:

$$\partial_t a_{\mathbf{k}}(t) = -\frac{i}{\hbar}[H, a_{\mathbf{k}}] = -icka_{\mathbf{k}}(t) - i\sqrt{\kappa c}\,\sigma_{GW}(t), \tag{2.4.3}$$

where the last equality follows from the commutator rules for a_k with itself and $a_k^\dagger$. $[a_k, a_k^\dagger] = 1$, and therefore these terms remains in the equation of motion.

Integrating over time from some initial time in which the state of the system is known, t_0, to the time of interest, t, yields

$$a_{\mathbf{k}}(t) = \mathrm{e}^{-ic\mathbf{k}(t-t_0)}a_{\mathbf{k}}(t_0) - i\sqrt{\kappa c}\mathrm{e}^{-ic\mathbf{k}(t-t_0)}\int_{t_0}^{t}\mathrm{d}t'\,\mathrm{e}^{-ic\mathbf{k}(t'-t_0)}\sigma_{GW}(t'). \tag{2.4.4}$$

For convenience we set $t_0 = 0$, and hence the electric field with the expression for the annihilation operator,

$$E(x,t) = \frac{1}{2\pi}\int_{-\infty}^{\infty}\mathrm{d}\mathbf{k}\,a_{\mathbf{k}}(0)\mathrm{e}^{-ic\mathbf{k}t+i\mathbf{k}\cdot\mathbf{x}} - i\sqrt{\kappa}\int_0^t \mathrm{d}t'\int\frac{\mathrm{d}\mathbf{k}}{2\pi}\mathrm{e}^{-ic\mathbf{k}(t-t')+i\mathbf{k}\cdot\mathbf{x}}\sigma_{GW}(t'). \tag{2.4.5}$$

The first term does not interact with the superatom: it 'passes by' without experiencing a change. Therefore, this part can be collapsed to a noninteracting term, $\bar{E}(ct-x)$. Assuming the incoming field to be coherent, the coherent field amplitude is defined $\alpha(t) = \langle\bar{E}(t)\rangle$. This field amplitude relates to the incoming coherent field as $|\alpha(t)|^2 = \mathcal{R}_{\text{in}}$.

The last, inner integral reduces to a delta function $\delta(t-t'-x/c)$, and the outer integral then has the shape of a Heaviside step function, denoted Θ. The Heaviside function is defined such that $\Theta(0) = 1/2$. The step function is usually given by the integral from $-\infty$ to some value t, whereas the outer integral in this case goes only from 0. This is handled by subtracting another Heaviside step function from $-\infty$ to 0, which again corresponds to multiplying two Heaviside step functions, such that

$$E(x,t) = \bar{E}(ct-x) - i\sqrt{\kappa}\,\sigma_{GW}(t-x/c)\Theta(x)\Theta(ct-x) \tag{2.4.6}$$

$$= \bar{E}(ct-x) - i\frac{\sqrt{\kappa}}{2}\sigma_{GW}(t-x/c). \tag{2.4.7}$$

For the last equality the approximation that the superatom is a zero-dimensional system has been applied, setting $\Theta(x) = 1/2$. Assuming the state of the incoming field is known all the way up to the superatom, but not after, $\Theta(ct-x)$ will be one for all times and positions after the superatom.

The expression for the electric field, equation 2.4.7, still contains the atomic operator σ_{GW}. To find a value for σ_{GW}, the atomic time evolution is considered by studying the equation of motion of an operator $A(t)$ interacting only with the superatom.

The equation of motion for this operator becomes

$$\partial_t A(t) = -i\sqrt{\kappa}\left(\bar{E}^*(t)[A(t),\sigma_{GW}(t)] + [A(t),\sigma_{GW}^\dagger(t)]\bar{E}(t)\right) \tag{2.4.8}$$

$$-\frac{\kappa}{2}\left([A(t),\sigma_{GW}^\dagger(t)]\sigma_{GW}(t) - [A(t),\sigma_{GW}(t)]\sigma_{GW}^\dagger(t)\right). \tag{2.4.9}$$

Equation 2.4.9 can be divided in two, a part regarding the coherent interaction, and a part which is dissipative, as described in equation 2.1.8.

For this operator, and with the coherent field amplitude, the effective Hamiltonian becomes

$$\mathcal{H}_0(t) = \hbar\sqrt{\kappa}(\alpha^*(t)\sigma_{GW} + \alpha(t)\sigma^\dagger_{GW}). \tag{2.4.10}$$

The effective Hamiltonian is responsible for describing the coherent part of the equation of motion, while the dissipative part can be rewritten to the Lindblad form,

$$\kappa\mathcal{L}[\sigma_{GW}]\rho(t) = \kappa\left(\sigma_{GW}\rho(t)\sigma^\dagger_{GW}(t) - \frac{1}{2}\{\sigma^\dagger_{GW}\sigma_{GW}, \rho(t)\}\right), \tag{2.4.11}$$

where ρ is the density matrix and $\{\cdots, \cdots\}$ denotes the anti-commutator, defined as $\{A, B\} = AB + BA$.

This relation is seen by using that whatever picture of quantum mechanics is used for calculations, the results must describe the same physical picture. Hence considering the time dependence to belong to an operator or a state must be equivalent, and we can write

$$\partial_t\langle A\rangle = \mathrm{Tr}(\partial_t A(t)\rho) = \mathrm{Tr}(A\partial_t\rho(t)). \tag{2.4.12}$$

The expectation value of the operator A is given by the trace of the operator applied to the density matrix - independently of where the time dependency is placed. The time dependency is moved by transforming between the Heisenberg and the Schrödinger picture with the unitary operator $U = \exp(-iH(t - t_0)/\hbar)$, which is sandwiched onto operators so that $A(t) = U^\dagger AU$, and $\rho(t) = U^\dagger\rho U$. Writing out $\mathrm{Tr}(A\partial_t\rho(t))$, one finds

$$\mathrm{Tr}(A\partial_t\rho(t)) = \mathrm{Tr}\left[\kappa A\left(\sigma_{GW}(t)\rho(t)\sigma^\dagger_{GW}(t) - \frac{1}{2}\left\{\sigma^\dagger_{GW}(t)\sigma_{GW}(t), \rho(t)\right\}\right) - \frac{i}{\hbar}A[H_0(t), \rho(t)]\right], \tag{2.4.13}$$

The above holds for the full density matrix, but the part concerning the envir

$$\partial_t\rho(t) = \kappa\left(\sigma_{GW}(t)\rho(t)\sigma^\dagger_{GW}(t) - \frac{1}{2}\left\{\sigma^\dagger_{GW}(t)\sigma_{GW}(t), \rho(t)\right\}\right) - \frac{i}{\hbar}[H_0(t), \rho(t)]. \tag{2.4.14}$$

With the equation of motion at hand, the expectation value of the outgoing field can be written as an expression of the expectation values of the atomic operators.

$$\langle E(t - x/c)\rangle = \alpha(t - x/c) - i\sqrt{\kappa}\langle\sigma(t - x/c)\rangle\Theta(x/c) \tag{2.4.15}$$

More interestingly, the actual outgoing field is given by the expectation value of the norm square of the field operator, namely

$$\begin{aligned}\langle E^\dagger(t - x/c)E(t - x/c)\rangle = {}&|\alpha(t - x/c)|^2 + \kappa\langle\sigma^\dagger_{GW}(t - x/c)\sigma_{GW}(t - xc)\rangle\Theta(x/c) \qquad (2.4.16)\\ &- i\sqrt{\kappa}\left(\alpha^*(t - xc)\langle\sigma_{GW}(t - x/c)\rangle - \alpha(t - x/c)\langle\sigma^\dagger_{GW}(t - x/c)\rangle\right). \qquad (2.4.17)\end{aligned}$$

This is the general set of equation governing the behavior of a two-level system interacting with an electric, coherent field. The system can be solved analytically in the case where there is no decay [19, 38].

To get the full behavior dephasing into the dark states and spontaneous emission into other modes than the incoming mode are added by hand, and the master equation becomes

$$\partial_t\rho(t) = -\frac{i}{\hbar}[H_0(t), \rho(t)] + (\kappa + \Gamma)\mathcal{L}[\sigma_{GW}(t)] + \gamma_D\mathcal{L}[\sigma_{DW}(t)] + \Gamma\mathcal{L}[\sigma_{GD}(t)] \tag{2.4.18}$$

Now the atomic operators σ are taken for three different transitions, as indicated by the different subscripts. Recalling that $\sigma_{AB} = |A\rangle\langle B|$, the three terms with the Lindblad operator handles decay of the Rydberg state with spontaneous emission of a photon into the foreward direction with rate κ and decay of the Rydberg state to an arbitrary mode with rate Γ. The second term handles dephasing from the Rydberg state into the manifold of dark states with rate γ_D. The last term contains the spontaneous decay of the dark states back to the ground state. The dark states and the Rydberg state decay spontaneously with the same decay rate, as they are both excited states.

The model given above with the included decay and dephasing can be used for simulating the system. Such simulations have already been shown for a superatom comparing the two photon correlation function measured in experiments to the model [19]. A similar comparison of the theory and the experimental results are shown in chapter 5.

To summarize on this chapter after introduction of the general interaction between a two-level system and a driving light field and an introduction of Rydberg physics, we show how a Rydberg superatom consisting of N atoms exhibits enhanced coupling to a driving field with a factor of $\sqrt{N}$. This coupling also shows up in the spontaneous emission from the excited state into the driving field mode. This decay is enhanced with $\sqrt{N}$ as well, while the spontaneous decay to an arbitrary mode remains the decay of a single atom. Due to the enhancement of field coupling, it is possible to study the interaction of the superatom two-level system with a few photon probe, and therefore the initial description of a classical light field coupled to a two-level system is extended to a description with a quantized electric field. This shows that for a waveguide system coupled to a driving field with coupling constant $\sqrt{\kappa}$ both the coherent term and the dissipative term depend on κ as $\sqrt{\kappa}$ and κ respectively.

Chapter 3

Experimental realization

In the scope of this thesis, a setup for the realization of a superatom was implemented as an addition to an existing experimental setup. In this chapter, a brief review of the theory of laser cooling and trapping will be given, along with a short description of our experimental procedure. The full existing experimental setup is well described elsewhere [39, 40], therefore only the main points of the experimental procedure will be described.

Laser trapping is applied to position the atoms for observation. At the same time, an extensive scheme of laser cooling is applied to reduce the thermal motion of the atoms to a level where they move less than the wavelength of the field of interest during the time of the pulse, thereby minimizing Doppler broadening.

3.1 Preparation of experiment

The preparation of an experiment requires the following steps:

- Cooling in a magneto optical trap (MOT)
- Raman sideband cooling and evaporative cooling in a dipole trap

Further, as it will be discussed in chapter 4, a secondary dipole trap is used to confine the atomic cloud even further in order to realize a Rydberg superatoms.

The preparation produces a cigar shaped cloud of ultracold rubidium gas in a dipole trap, which suspends the cloud in ultra-high vacuum.

The atomic cloud is loaded from a room temperature gas of Rubidium in the vacuum chamber. The gas is mainly ^{85}Rb and ^{87}Rb in natural abundance relation provided by electrically heated dispensers. The pressure of the gas is 2×10^{-10} mbar. From this background gas a magneto optical trap (MOT) is loaded; it contains only ^{87}Rb atoms due to the laser frequencies applied.

3.1.1 MOT

The MOT provides a dissipative and a conservative force on each atom. The dissipative force slows the atoms, while the conservative force provides a trap.

The dissipative force is provided by pairs of counterpropagating laser beams. The frequency of the laser is red detuned from an atomic resonance. Due to the Doppler effect, atoms traveling in a detuned field will experience a shift in the field frequency depending on their velocity. Atoms within a certain velocity range will interact strongly with the light, as they experience it shifted to resonance. This velocity range is determined by the detuning and by the bandwith of the laser.

A red detuned laser beam will slow the atoms, since momentum is conserved in the excitation process, but not in the subsequent de-excitation, where the direction of the spontaneously emitted photon occurs in random direction. Due to this random direction of spontaneous emission, the mean contribution from reemission is zero, while momentum contribution from excitation is in the opposite direction of the atom movement, hence the atom is slowed by the interaction.

The light fields of a MOT which serves to cool the atoms does not provide any trapping. Hence atoms which have been slowed down by the light of the MOT, are not confined and will eventually, by random walk, exit the MOT volume. This slowing effect with detuned light is referred to as optical molasses.

In order to produce a trap, a force which depends on the position of the atoms is also needed to keep the slow atoms at the position of interest. Such a conservative force can be introduced by making the light-atom interaction depend on their position. To do this, a quadrupole magnetic field is applied. The Zeeman effect causes a splitting in the m_F-levels of each state, which are otherwise degenerate. Due to the spatially varying quadrupole magnetic field, the splitting of the levels will be position dependent

With the spatially varying splitting of the levels, the levels are only degenerate where the magnetic field is zero. The m_f-levels are sensitive to polarization of light. By choosing the circular polarization of the light in each MOT beam, it is possible to choose which $\sigma^{\pm}$-transitions is driven by the specific beam. This means that the trap can be setup so that atoms which are far from the center of the trap, but still in the capturing light will scatter more strongly on light propagating towards the trap center.

To get three-dimensional cooling and trapping, the optical part of the MOT comprises six pairwise reflected beams at right angles, and the magnetic field is a quadrupole field. The MOT beams are all intersecting in the center of the magnetic field.

For a MOT, the capture velocity is related to the velocity range of atoms addressed by the laser beams. Atoms faster than the capture velocity are not trapped, as they will experience the light detuned too far from resonance to interact strongly with it.

In the setup described here, the laser frequency is detuned to the D_2 transition in ^{87}Rb, which is a closed transition.

3.1.2 Optical dipole trap

After loading the MOT for around 1.3 s it contains around 5×10^6 atoms, which are loaded into an optical dipole trap, in which they are kept for most of the experimental procedure. The trapping beams of the optical dipole trap are illustrated in figure 3.2.

To load the optical dipole trap, the trap is on in the center of the magneto-optical trap, which is then turned off. The trapping beam is crossed at an angle of 32°. They are focused at the crossing point where a potential minimum in the trapping potential is formed as a consequence. This trapping potential results in an elongated atomic cloud.

The dipole trap is far detuned from resonance as it is operated at wavelength 1070 nm. The operation power of the trap is relatively high, up to $P_{odt} = 11\,\mathrm{W}$ in the beams. The dipole trap in this experiment addresses the D_1 and D_2 transitions.

Dipole trapping relies on the interactions between induced atomic dipole moments and the intensity gradient of the field and not on radiation pressure as in the MOT. As the dipole interactions are second order effects, the contribution to heating from the dipole trap is minimal [41].

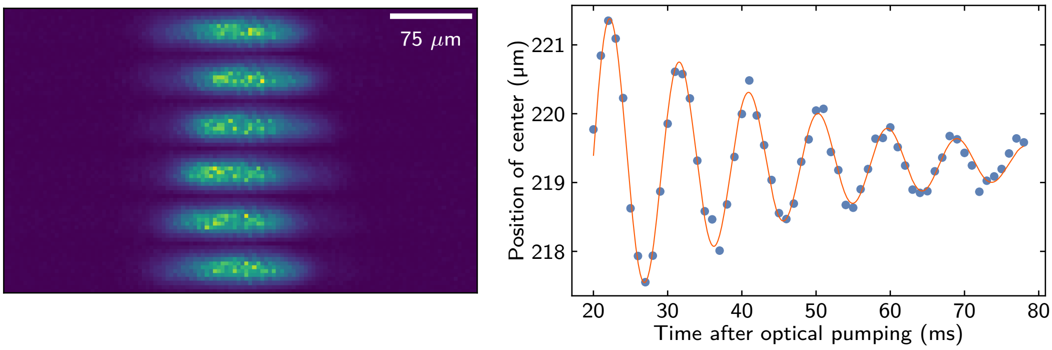

Figure 3.1: Oscillations in dipole trap. **a)** Atomic cloud at different times after optical pumping. Each slice is averaged over four images, and the spacing is 3 µs. The oscillations are taken from top. **b)** Center of Gaussian fitted to the atomic cloud density profile (points). An exponentially damped sinusoidal fit is shown as the line.

For a transition to a level with decay rate Γ and resonance frequency ω_0, addressed by a laser with frequency ω and intensity I, the dipole potential for this specific transition is

$$U_{\text{dip}}(\mathbf{r}) = -\frac{3\pi}{2\omega_0^3}\frac{\Gamma}{\omega_0 - \omega} I(\mathbf{r}). \tag{3.1.1}$$

Thus a deep potential is achieved if $\Delta \approx 0$, where $\Delta = \omega_0 - \omega$. However, as the spontaneous scattering rate scales with $\Delta^{-2} I(\mathbf{r})$, the heating from scattering makes the limit $\Delta \approx 0$ undesirable for a trap [41].

In our case the main contributions stem from the D_1 and D_2 transitions. For these the dipole trap potential becomes

$$U_{\text{dip}}(\mathbf{r}) \approx \frac{3\pi c^2 \Gamma}{2\omega_0^2}\left(\frac{2}{\Delta_2} + \frac{1}{\Delta_1}\right) I(\mathbf{r}). \tag{3.1.2}$$

Here the polarization of the light, which would affect the respective trapping for different m_f states, is not taken into account. $\Delta_{1,2}$ is the detuning from the $D_{1,2}$ transition respectively.

The trapping potential of equation 3.1.2 can be approximated with a harmonic potential. For the trapping parameters, the frequency of this harmonic potential can be calculated. For a crossed dipole trap, the angular trapping frequencies are $\nu_x = 2\pi \cdot 0.71\,\text{kHz}$, $\nu_y = 2.5\,\text{kHz}$ and $\nu_z = 0.71\,\text{kHz}$, where z is along the probe, y is in the plane spanned by the dipole trap beams and x is out of this plane, and are calculated for the maximal value of power in the dipole trap beams. Thus they are the maximal achievable trapping frequencies, and the frequencies of the trap during experiments are often lower.

Oscillations of the atomic cloud in the trap can be observed experimentally. To show the oscillations, the time after repumping between hyperfine levels is varied. The optical pumping introduces a momentum kick to the cloud, which will yield an oscillating atomic cloud. The oscillation frequency is characteristic for the trap. The oscillations are damped out over time, due to interactions between the atoms in the cloud. Both the oscillations and the damping effect are clearly observed in the dipole trap. An example of these effects is presented in figure 3.1 a), which shows the oscillations over time for a the first oscillation peak, and figure 3.1, where the points show the center of atomic cloud as a function of time. The center is fitted with a Gaussian. The solid line shows a damped sinusoidal fit to the center.

The fit yields a trap frequency of $\nu_z = 0.11\,\mathrm{kHz}$, which is much lower than the expected trapping frequencies calculated for the dipole potential. However, the images are taken after evaporative cooling, where the power in the dipole trap is ramped far down and only somewhat up again, and therefore this low value is not unexpectedly low.

The evaporative cooling is one of a number of steps used to cool the atoms in the dipole trap further. Firstly, a Raman sideband cooling (RSC) scheme is applied, which allows cooling without loss of atoms. RSC is followed by an evaporative cooling scheme, where the optical dipole trap is ramped down with three different rates to allow fast atoms to escape the trap, while the coldest atoms are left behind. The trap is ramped back up.

This process leads to a temperature of $5.9\,\mu\mathrm{K}$ and trap dimensions $60\,\mu\mathrm{m}$ along the probe and $15\,\mu\mathrm{m}$ in the other two directions where the dimensions are measured as the $1/e$-width of the Gaussian density profile of the atomic cloud. This atomic ensemble can then be used for experiments, as described in the following.

After the cooling state, the atoms are then optically pumped into the m_F-level which is addressed by the probe light. It is this optical pumping light which is used to kick the atoms to show the oscillations of figure 3.1.

3.2 Experimental procedure

After the preparation described above, experiments are performed on the atomic ensemble with a weak light field, the probe, and a counterpropagating strong control field. The two fields are focused to waists of $6.2\,\mu\mathrm{m}$ and $14\,\mu\mathrm{m}$ respectively. The foci are overlapped with the center of the dipole trap Figure 3.2 b) illustrates how the dipole trap beams crosses in the vacuum chamber, and how the probe and control light goes through the atomic ensemble caught in this the trap.

The system is driven with the transition from the ground state $|5S_{1/2}, F = 2, m_f = 2\rangle$ to $|111S_{1/2}, J = 1/2, m_j = 1/2\rangle$ through an intermediate state $|5P_{3/2}, F = 3, m_F = 3\rangle$. The probe wavelength is wavelength 780 nm and a strong control beam is of wavelength 479 nm.

The van der Waals coefficient of this state is calculated to be $C_6 = 1.88 \times 10^5\,\mathrm{GHz}\,\mu\mathrm{m}^6$ with the Pair Interaction software[28], and the Rabi frequency of the control field is $\Omega = 2\pi 12\,\mathrm{MHz}$.

The probe pulse has a Tukey-shape. This shape is chosen because it has a long constant part and the rise and fall times are long enough to avoid too much Fourier broadening. The Tukey shape is defined by

$$f(t, t_{rise}, t_{\mathrm{up}}) = \begin{cases} \frac{1}{2}\left\{1 + \cos\left(\pi\left[\frac{t + t_{\mathrm{rise}} + \frac{t_{\mathrm{up}}}{2}}{t_{\mathrm{rise}}} - 1\right]\right)\right\} & \text{if } -t_{\mathrm{rise}} - \frac{t_{\mathrm{up}}}{2} \leq t < -t_{\mathrm{up}}/2 \\ 1 & \text{if } -\frac{t_{\mathrm{up}}}{2} \leq t < \frac{t_{\mathrm{up}}}{2} \\ \frac{1}{2}\left\{1 + \cos\left(\pi\frac{t + \frac{t_{\mathrm{up}}}{2}}{t_{\mathrm{rise}}}\right)\right\} & \text{if } \frac{t_{\mathrm{up}}}{2} \leq t < t_{\mathrm{rise}} + \frac{t_{\mathrm{up}}}{2} \\ 0 & \text{otherwise.} \end{cases} \tag{3.2.1}$$

The parameters t_{rise} and t_{up} determines how sharply the pulse rises and how length of the flat part of the pulse respectively. For the pulse we usually use, the up time is $5\,\mu\mathrm{s}$ and the rise time is $0.8\,\mu\mathrm{s}$.

Each atomic medium is recycled over 1000 experiments. The experiments are performed within a time of 100 ms. For each experiment the optical dipole trap is turned off for $14\,\mu\mathrm{s}$ during probing. After probing the dipole trap is turned back on, recapturing the atoms.

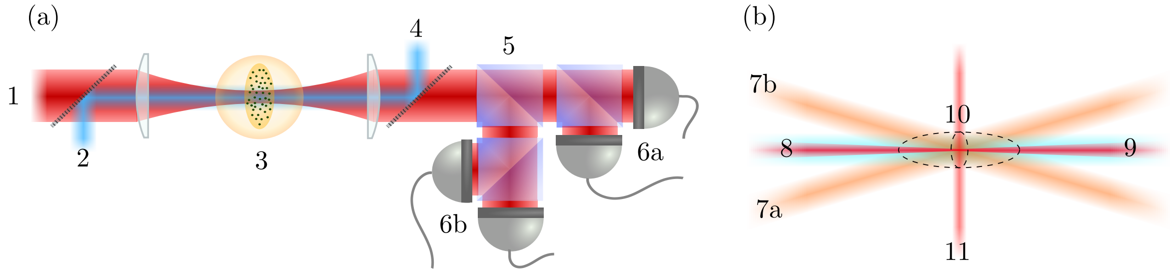

Figure 3.2: Schematic illustration of the laser setup. a) Setup of probe and control laser with a single superatom. 1) is the probe light, which is narrowly focused down onto an atomic cloud, 3), which is all within a single Rydberg blockade radius (illustrated with the yellow sphere). The probe light goes through a 50/50 beam splitter, which sends the light into two Hanbury Brown Twiss setups, which again each contains a 50/50 beams plitter. The light is detected by four single photon counting modules (SPCM), 6a) and 6b). The control light is propagating in the opposite direction of the probe light, entering at 4 and leaving at 2, and it is overlapped with the probe beam with dichroic mirrors. b) Laser beams inside the vacuum chamber. Two dipole trap beams, 7a) and 7b), are crossed, trapping an atomic cloud 10)(large dashed ellipse) in the intersection. The counterpropagating probe, 8), and control, 9), lasers are focused on the center of the atomic cloud. A third trapping beam can be overlapped with the dipole trap 11). This trap further confines the atomic cloud, yielding a smaller, denser cloud 10) (small dashed ellipse), called a dimple. Depending on the detunings of probe and control, the dimple can be tuned to the superatom regime.

After each measurements any remaining Rydberg excitations are removed with a field-ionization pulse. For the superatom, which hosts only a single excitation, the field ionization pulse removes a single atom from the medium.

Since atoms are removed with this field-ionization from the atomic cloud after every experiment, the atom number in the cloud will decrease over time. To avoid this, the optical dipole trap intensity is ramped up over the 1000 experiments with a slope that gives a constant absorption of the probe at resonance with the intermediate state and without control field.

After the 1000 experiments the atomic cloud is released and 1000 reference experiments are performed without any medium. To ensure that the atoms have fully evaporated before the reference experiments, these are only performed after 10 ms wait time with trapping and cooling light off.

The setup of the probe and control light is illustrated in figure 3.2 a). In the figure, it is assumed that the experiment is configured so the atomic cloud is already confined by a second trap in addition to the dipole trap, yielding a smaller atomic cloud. In the next chapter, the setup of such a trap is described.

The probe signal is detected on four single photon counter modules (SPCM) in an extended Hanbury Brown Twiss setup with three 50/50 beam splitters distributing the light equally on the counters. This detection scheme is shown in figure 3.2 a). The quantum efficiency for the four counters is approximately 64 %.

Chapter 4

Dimple setup

In section 2.3, the Rydberg superatom was introduced. To experimentally realize an atomic medium confined within a given Rydberg blockade sphere, thereby enabling the creation of a Rydberg superatom, a second trapping setup is implemented in the experiment described in chapter 3.

The experimental preparation described in chapter 3 produces a cigar shaped atomic cloud with $1/e$ radial and axial radii of 15 µm and 60 µm respectively. This oblong cloud can further be overlapped with other, more tightly focused laser beams perpendicular to the probe axis. In the scope of this thesis, the setup for producing these additional traps was assembled and integrated with the existing experimental. The additional traps, the dimple traps, will be discussed in the following.

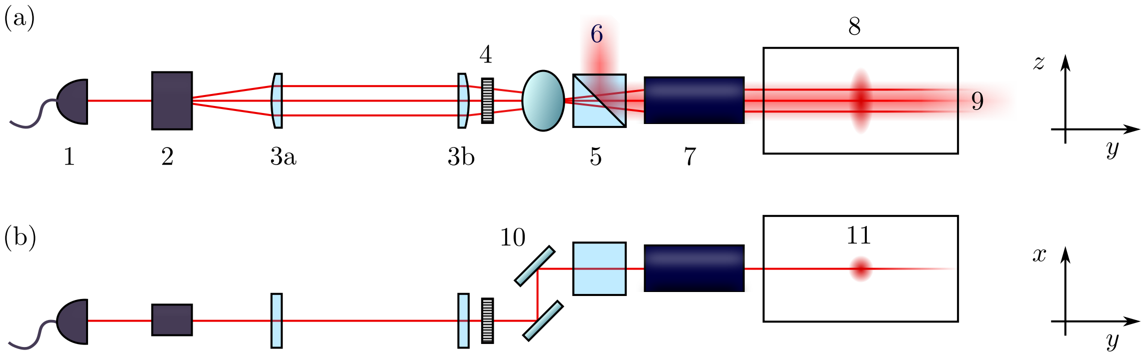

Figure 4.1: Setup of dimple trap. **a)** Viewed from top. **b)** Viewed from the side. The elements are 1) a fiber outcoupler, 2) the acusto-optic deflector (AOD), 3a) and 3b) a telescope of cylindrical lenses serving two purposes, namely to enlarge the beams in the y-direction in order to focus them more to more narrow spots when they pass through the focus, and to make the diffracted beams from the AOD parallel, 4) a half wave plate, polarizing the light of the dimple trap so they are transmitted through 5), which is a polarizing beam splitter, and 7) the objective. The objective is focusing each beam tightly down onto the atomic cloud in the dipole trap inside the vacuum chamber 8). The polarizing beam splitter is used to reflect the imaging light 9) out of the dimple beam path and on to a camera 6). 10) A periscope is used in the setup to lift the beams and to give alignment freedom. 11) is the atoms in the dipole trap viewed from the side.

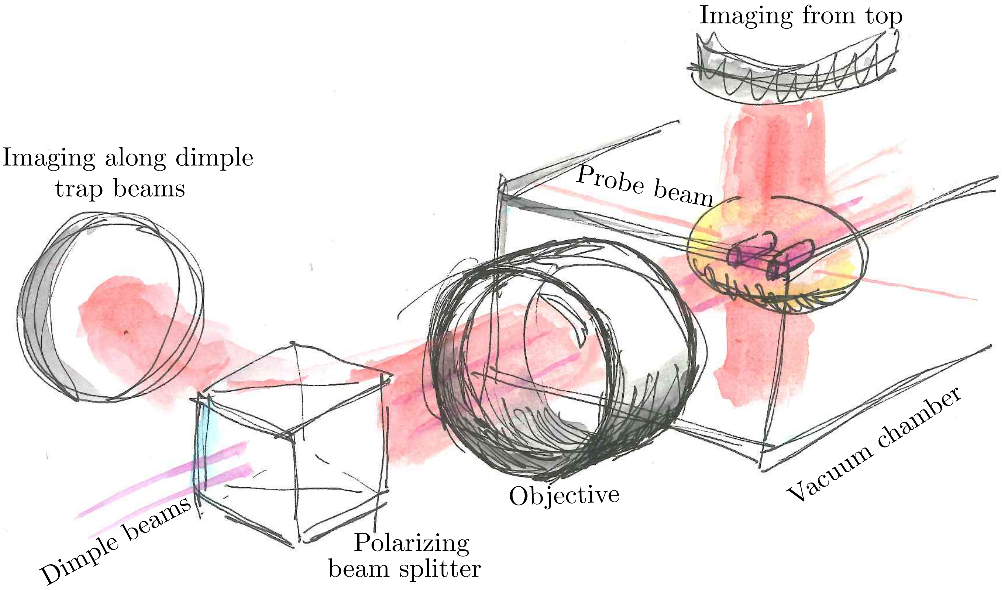

Figure 4.2: Sketch of setup showing the two currently available directions of absorption imaging. Imaging along dimple trap beams refer to absorption imaging with light counterpropagating the dimple beams. The imaging light is number 9 in figure 4.1, and it is reflected out of the dimple beam path by the polarizing beam splitter, which is number 5 in figure 4.1, and onto a camera. Imaging from top refers to absorption imaging with light coming from below the vacuum chamber and being detected on a camera above the chamber. An atomic ensemble in the optical dipole trap is drawn in yellow, and two overlapped dimple traps are marked with purple.

4.1 Setup

The setup for the dimple trap, figure 4.1, consists of an 805 nm laser beam, tightly focused with an objective onto the dipole trap. Before the telescope, the light passes through an acusto-optical deflector (AOD). With the AOD, the position of the first diffraction order in the direction along the probe can be controlled by the frequency of the applied radio-frequency field. The AOD can also, if multiple radio frequencies are applied, split the beam in multiple spots corresponding to the frequencies. Introducing the AOD gives the setup considerable versatility, as it can produce both single and multiple dimple traps, and as the position of the dimple beams in the z-direction as defined in figure 4.1 to some degree can be controlled individually.

In order to get a trap confining an atomic ensemble to a volume defined by the Rydberg blockade radius, the beam is enlarged in the direction along the probe beam with telescope of cylindrical lenses. The telescope also serves the purpose of making the outgoing beams of the AOD parallel to the each other.

To have an alignment tool for the position of the dimple beam with respect to the crossed optical dipole trap, a periscope is inserted which raises the height of the beam from 5 cm to 12.5 cm at which all experiment optics are mounted. However, this periscope can introduce aberrations in the optics which can lead to problems with the trapping potential.

The beams for the dimple trap enter the vacuum chamber along an axis which is also used for imaging. The imaging light is counter propagating to the dimple beam, and therefore a polarizing beam splitter cube and a half-wave plate are introduced in the beam path, so that the imaging light is reflected onto a camera before the periscope while the dimple beam is allowed

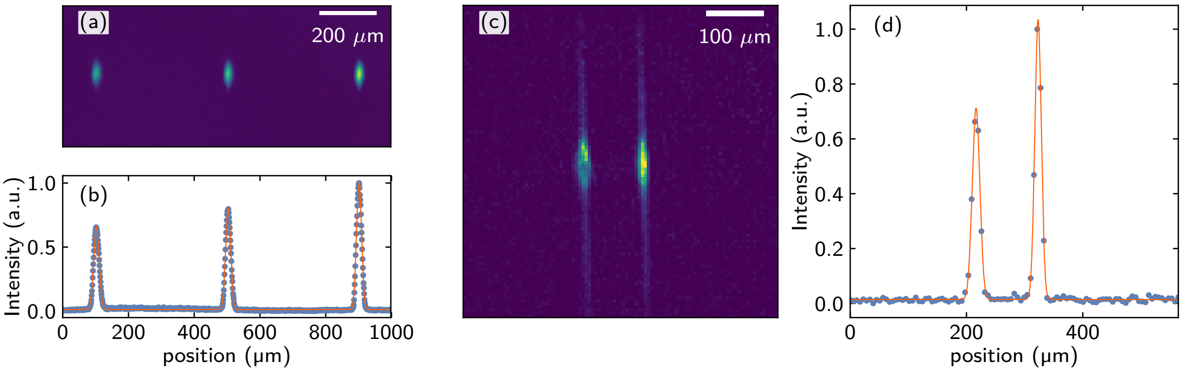

Figure 4.3: Size of dimple trapping beams and resulting atomic clouds. **a)** Imaging of three dimple beams focused onto the Raspberry Pi camera module. **b)** Gaussian fit estimating the beam size of the beams in a). **c)** Two atomic clouds in dimple traps imaged with absorption imaging from top, as defined in figure 4.2, averaged over 10 images. The dimple trapping beams come from the bottom of the image. The two atomic clouds are so dense in the center of the image because they are confined by the optical dipole trap. **d)** Gaussian fit estimating the size of the atomic ensembles.

to pass.

In the following sections, each component is described, and the alignment of the setup is discussed.

4.1.1 Laser

The dimple traps are produced with an amplified 805 nm laser. This wavelength is chosen as a compromise between having a far-detuned laser to minimize heating and having a wavelength close to resonance and hence allowing imaging and trapping through the same objective. As the position of focus depends on the wavelength, meaningful imaging can only be done through the same optics when the trapping and the imaging wavelengths are not too far apart. Further the required power is not very high. The dimple trap presented here holds around 20 mW. As some light is clipping at the chamber, very high powers are not useful for the dimples.

The imaging along the dimple trapping beams are shown in figure 4.2.

4.1.2 Objective and telescope

The objective used for focusing the dimple beam down on the dipole trap has been used for imaging in this direction as well as for an earlier iteration of the dimple trap, and has an effective resulting in an effective focal length of 79.5 mm [19, 42].

A telescope is used to enlarge the beam in z-direction as defined on figure 4.1 while the size of the beam in y-direction as defined on figure 4.1, is determined by the spherical lens with focal length $f = 6.25\,\mathrm{mm}$ that collimates the beam from the fiber. In this coordinate system, the probe propagates along the z-axis, and the dimple beam propagates along the y-direction.

The initial testing of the objective was done with a Raspberry Pi camera module, which was used to determine the beam size and other properties, while the absorption imaging was used in the actual setup to give estimates of the same values.

The telescope was initially planned to contain a lens of focal length $f = 75.6\,\mathrm{mm}$ and a lens of focal length $f = 500\,\mathrm{mm}$, but due to space constraints on the main experiment table, the second lens was changed to a lens of focal length $f = 300\,\mathrm{mm}$ when the dimple trap was integrated with the existing experiment. This means that there is a small difference between the spot sizes measured on the Raspberry Pi camera module and the size on the dimple trap.

With the $f = 500\,\mathrm{mm}$ lens in the telescope, the waist was calculated to be $5.3\,\mu\mathrm{m}$ in the narrow direction. The waist in the wide direction was calculated to be $26\,\mu\mathrm{m}$. These results compare relatively well to the beam size deduced from images on the Raspberry Pi camera module, as shown in figure 4.3. The fit results in a beam radius ($1/e^2$) of $7.4\,\mu\mathrm{m}$, and a beam height of $26.5\,\mu\mathrm{m}$. These difference arises from alignment.

With the final telescope, the objective yields a beam with waist size $w_z = 8.9\,\mu\mathrm{m}$ in z-direction and $w_x = 29\,\mu\mathrm{m}$. The size of the spots for the final telescope was only investigated indirectly, as the change of telescope was done at the experimental table. For the final imaging, the interesting parameter is the extend of the atomic medium in each dimple trap. The dimple beam size is only one out of a number of parameters determining the number of atoms in each dimple. The other parameters include intensity in both the dimple trapping laser and the dipole trap laser, as well as loading time of MOT, time of flight, evaporation cooling parameters, etc.

Beam distortion

Proper alignment of the objective is key to the quality of the experiments. If the beam passes through the objective with a tilt or off centered, it results in a variety of deformations of the beam shape. This is demonstrated in figure 4.4.

There are a number of things worth noticing in figure 4.4. Firstly, in figure 4.4 a) the three spots which in the first line image are clear, narrow lines, evolves into a split beam shape with substructure as the camera is moved out of the point of focus. This evolution, which starts with the clear, narrow line, goes through first a state where each spot seems to have a companion spot on each side (second line), then it is divided into a cloven hoof shape (third line), and in the fourth line, the three spots have gained butterfly shapes. In this butterfly shapes, some further substructure can be seen.

The distortion of the beam is also different for each spot, though the differences are minor. One notices however that the spot on the right seems to have a stronger right toe (remaining in the cloven hoof picture) in line three. For the left spot, the left toe is stronger. This indicates that some distortion is due to the point where the beams hit the objective.

The amplitude in each of the three spots is different, which can either be due to the AOD not providing exactly the same power in each diffraction, or due to background light. One also notices that the three beams evolve only to the left. This is assumed to be due to the stage of the camera not being aligned with translation exactly along the beam.

Considering the images in figure 4.4 b), which are from absorption imaging, it is clear that the distortion of the beam will be reflected in the resulting atomic cloud.

4.1.3 Acousto-Optic Deflector

For the Acusto-Optic Deflector (AOD), an element from AA Opto-Electronics[1] is used. The AOD contains a crystal of TeO_2, and the light passes through an axis of the crystal, where the speed of sound is $650\,\mathrm{m/s}$.

The crystal is driven with radio frequency by a piezo inducer. Depending on the radio frequencies applied, the angle of diffraction in one plane varies. In principle there is no limit to the number of frequencies applied. In the setup described here, up to four frequencies can be

---

[1] Model DTSX-400-800

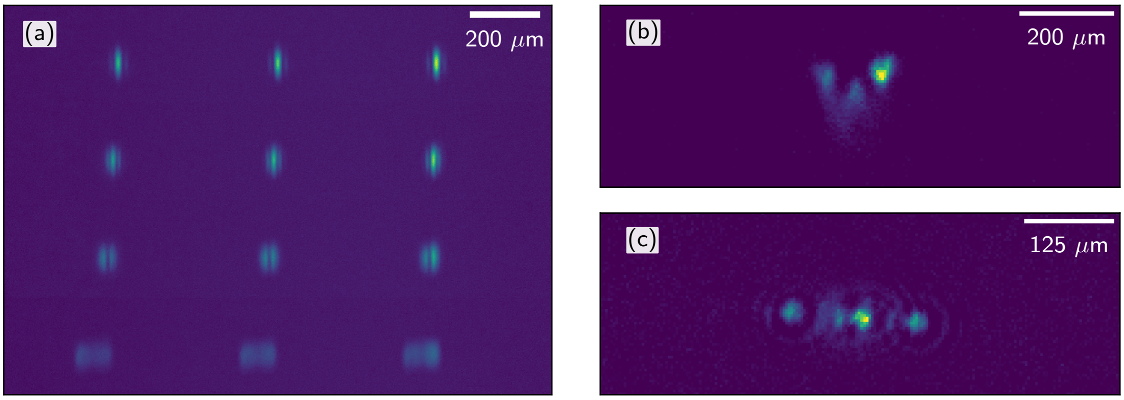

Figure 4.4: Spot deformations out of focus. **a)** on the Raspberry Pi camera module, moving the camera away from the point of focus. Between the images, the camera was moved on the order of 0.4 mm on a translation stage. **b)** in absorption imaging of the plane spanned by probe and dimple beam. A resonant laser is used to blow away atoms in the dipole trap. The scull-shape is due to the same cloven hoof-shape as in a). This image is averaged over 6 images. **c)** Distortion as seen with absorption imaging along the dimple beam. Multiple smaller traps are formed by three trapping beams.

used. The diffractions have already been shown in figures 4.3 and 4.4. On these figures three laser beams are shown as seen by the Raspberry Pi camera module, and two atomic clouds are seen as a result of overlapping the dimple trap beams with the optical dipole trap.

Figure 4.5 shows the position of spots as a function of applied frequency. As the line shows, the position depends at least to a very good approximation linearly on the applied frequency. The AOD is specified to have a linear dependency of the diffraction angle on the frequency of the rf-field, and when investigating only the range of angles where the small angle approximation is valid, the linear dependency of position on frequency is well supported. The frequency cannot be used as a direct measure of the positions of spots, as these depend on the optics between the AOD and the point of measurement.

The frequencies applied to the AOD are set by individual channels of a four channel DDS board. Before applying the signal to the AOD, the signal from the individual channels are mixed with a power combiner and amplified. This means that the intensity distribution in the dimple beams can be well controlled.

The light intensity in each trapping beam is however also controlled by other factors, including alignment of the AOD and frequency. There is a certain frequency dependence of the diffraction efficiency, but since the atom number in the end is the figure of merit, and this also depend on the alignment of the dimple trap on the dipole trap, the amplitudes are are chosen based on absorption imaging and probe absorption scans rather than the measured power in each diffraction order.

In the case where we are interested in more than one dimple traps, it is important that all diffraction spots have the same intensity. It turns out that the intensity in each spot depends on the number of frequencies applied, the total power in the situation where two frequencies are applied is smaller than the sum of power for each frequency applied. Therefore when operating two dimple beam the intensity in each is chosen to be only around one fourth of the maximal intensity, as this gives approximately the same power in two beams together as the sum of two independent beams.

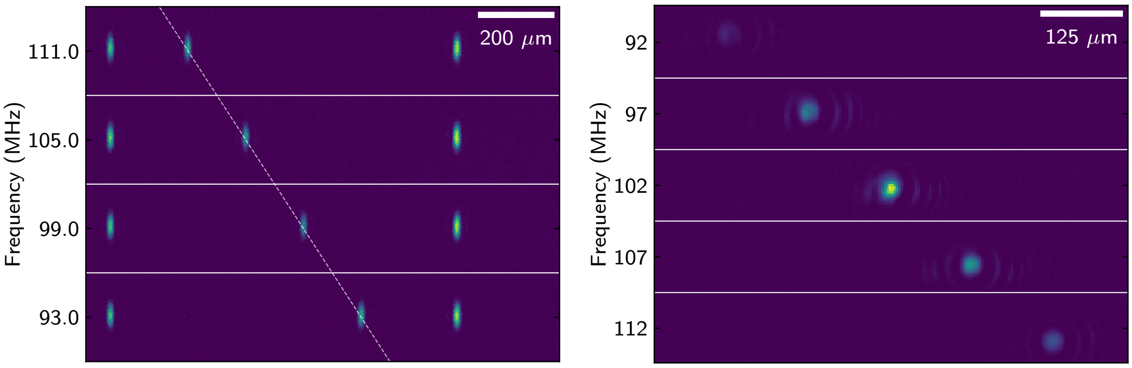

Figure 4.5: Beam position as a function of applied frequency. **a)** on the Raspberry-pi camera module. Here four images are shown together. For the actual linear fit, these are four out of a series of 33 images. For each image, a Gaussian is fitted to each spot in horizontal direction. The centers of the Gaussian fits are used for a linear fit, shown as the dashed line. **b)** in the absorption imaging, here in the imaging along the dimple trap, the position of the beam as function of frequency is also well described by a linear dependency. Each slice is averaged over 6 images.

As all acousto-optic devices, the AOD introduces a frequency shift of the applied frequency. This is not of great importance when considering the detuned trapping laser, but for alignment purposes, where an on-resonant laser replaces the far-detuned 805 nm trapping laser, it is important to consider this shift.

4.2 Integration in existing setup

The objective is also used for the imaging, hence the setup also contains a polarizing beam splitter cube and a half-wave plate, as shown in figure 4.1. The beams for the dimples enter the chamber along the $y-$axis, perpendicular to the probe.

The main challenge of integrating the dimple trap setup with the existing setup is posed by alignment of the dimple beam well on the optical dipole trap. The main tools of alignment is the absorption imaging and single photon measurements. How to align with these tools will be discussed in the following sections.

4.2.1 Alignment in absorption imaging

A single dimple beam is aligned on the dipole trap using the absorption imaging in the independent direction. For this the 805 nm trapping laser is replaced by a laser on resonance, which blows away the atoms in the dipole trap where the beam hits the cloud. By iteratively decreasing the power in the resonant beam and realigning it on the cloud, a starting point for alignment with the trapping laser is reached. Figure 4.6 a) shows the resonant laser cutting the dipole trap in half as the power is increased. Figure 4.6 b) shows alignment of the dimple beam onto the optical dipole trap. A well aligned dimple beam will together with the dipole trap produce a trap deep enough to contain all the atoms that will otherwise be placed throughout the dipole trap.

In figure 4.6 b) it is seen how a dimple beam which initially is just touching the dipole trap will not have much an effect, but as the height of the beam is changed, fewer atoms will remain

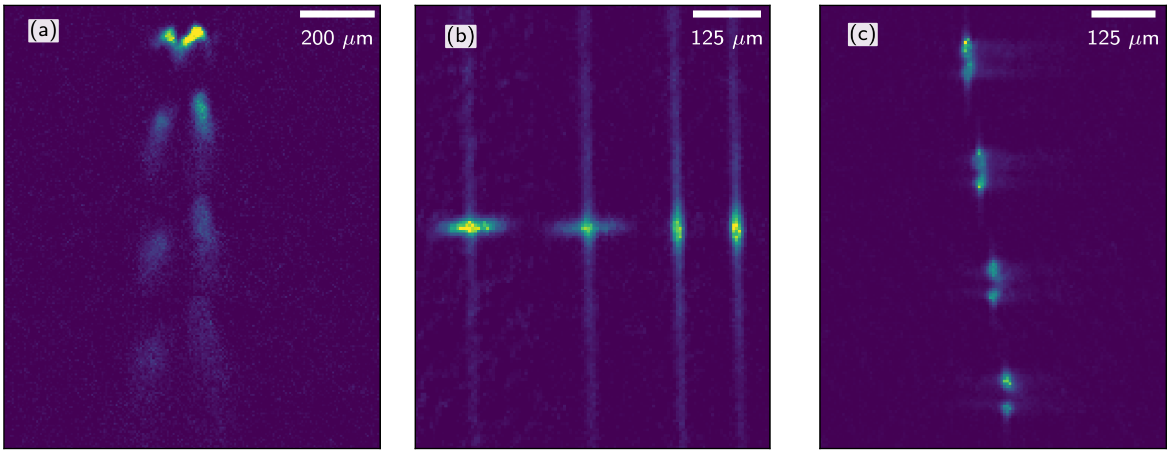

Figure 4.6: Alignment procedures. All imaged from top as defined in figure 4.2. **a)** atoms in the dipole trap are blown away with an on-resonant beam. **b)** alignment of dimple beam onto dipole trap. Each vertical slice represents a different position with respect to the dipole trap. It should be noted that this figure is sliced in the opposite direction of figure 4.5. When the dimple trap is not well aligned, some atoms from the dimple trap will fill the dimple beam, while most will stay in the dipole trap. As the alignment is improved, the dimple trap provides a deeper potential than the dipole trap, and the atoms will preferentially fill the the dimple trap. Thus, the dipole trap vanishes as the alignment is improved. **c)** dimple trap being cut by the probe as the dimple beam is scanned over the dipole trap.

within the extent of the dipole trap, as seen in the second strip. The third and fourth strip shows a well overlapped dimple beam where all the atoms are in the dimple trap.

In figure 4.6 b), the dipole trap offers some confinement to the last two lines. To find and overlap the focus of the dimple trap with the dipole trap, the dipole trap is ramped relatively far down so the atoms are somewhat free to distribute themselves along the dimple beam. This alignment is complicated by the fact that misplacement of the objective alters the beam path. This can cause a tilt in the beam, which is not necessarily easy to detect on the far side of the vacuum chamber, where the beam has expanded. If the beam has a tilt when it is overlapped with the dipole trap, and this is then ramped down, the atoms can slide along the dimple trap beam under gravity. If the beam is far out of focus, the atoms are not very well confined, and can slide due to gravity, giving a wrong impression of the position of the focus. In the current experimental setup, we do not have imaging along the probe axis. Therefore, this tilt cannot be observed directly, but the alignment must rely on the somewhat precise observation of the large beam coming out on the backside of the vacuum chamber.

Though optimal alignment is important, as long as the focus of the dimple beam is well overlapped with the dipole trap it is not crucial to achieve perfect alignment of the dimple beam, since for even relatively large tilt angles the trap geometry will overrule the pull of gravity. Furthermore, the experiments are performed within very short time after turning off the dipole trap, and therefore the atoms cannot move very far.

Figure 4.6 c) shows the probe beam blowing away atoms in the center of the dimple trap. The slices show frequency scans across the dipole trap. This is an important alignment tool. Figure 4.6 reveals an important point about the alignment procedure. Across the applied frequencies, the cut becomes clearer, as seen in figure 4.6 c). This is a result of a rotation of the AOD

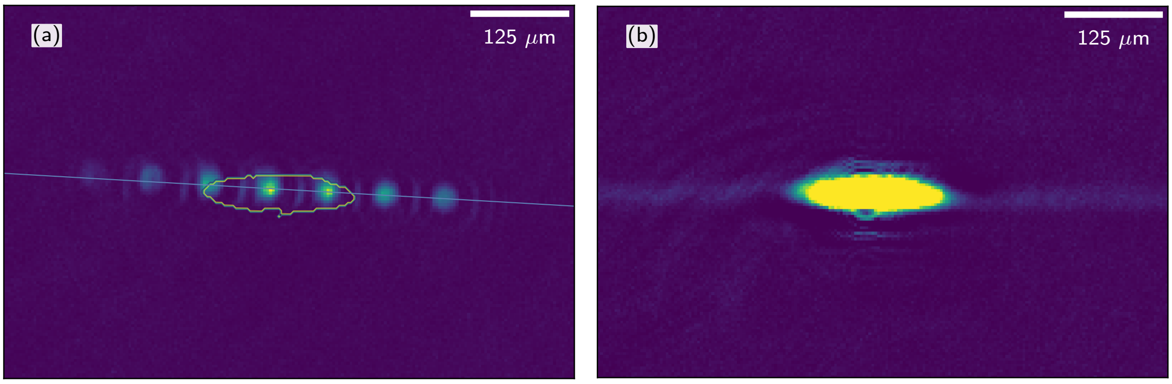

Figure 4.7: Dimple beams rotated with respect to the plane of the dipole trap. **a)** Horizontal absorption imaging showing a scan of frequencies showing a rotation with respect to the large cloud. The contour of the large cloud is outlined. A line 3.29° above horizon is plotted on top to illustrate the tilt. The image is averaged over images for seven frequencies. Each of the spots thus correspond to a frequency. For each spot, six images are averaged. The spots are from the same measurement as is shown in figure 4.5 b). **b)** Shows the corresponding cloud, giving rise to the outline in figure a). The cloud is not averaged over multiple images, and it has the same color scale as a) to illustrate the difference in atom number in the dimple traps and in the dipole trap. The apparent structure in the large cloud is an imaging artifact, arising from the imaging through the same optics as is used for the dimple trap.

deflection axis around the dimple beam axis. This is in principle not a problem if only one dimple beam is used, but it poses a problem for alignment of multiple dimple traps.

Alignment of multiple dimple beams is relatively complicated compared to alignment of a single dimple beam, due to the extra degrees of freedom added by having two beams. Aligning the plane of AOD deflections with respect to the plane of the dipole trap becomes difficult through the combined effect of objective, periscope and AOD. This is mainly a problem because the dimple beam height is smaller than the height of the optical dipole trap, as seen in figure 4.7 a). If the beams were higher than the dipole trap, the confinement provided by this would make rotations of the diffraction plane less crucial. In future iterations, it might be convenient to add an additional telescope to enlarge the beam perpendicular to the diffraction plane.

The problem of rotation is not of importance in the case when only a single diffraction order is used, but it becomes a hindrance when more than one dimple beam is applied. It is also a problem if the frequency applied to the AOD is changed, as this motion of the trap is tilted compared to the dipole trap and the probe. A scan through the large trap is shown in figure 4.7 a). Here a clear rotation is seen with respect to the dipole trap beams, which are seen in figure 4.7 b).

Alignment of dimple beam on optical depth

Aligning the dimple beam well on the dipole trap creates a small atomic cloud. For the experiments, it is critical that the probe beam is carefully centered on the atomic cloud, and since the dimple beam is smaller than the optical dipole trap, it is not enough to have the dipole trap centered around the probe, the dimple trap also needs to be aligned well on the probe.

The alignment of the dimple trap onto the probe beam can to some extent be done with absorption imaging. The probe cutting through the dimple imaged from top as defined in figure

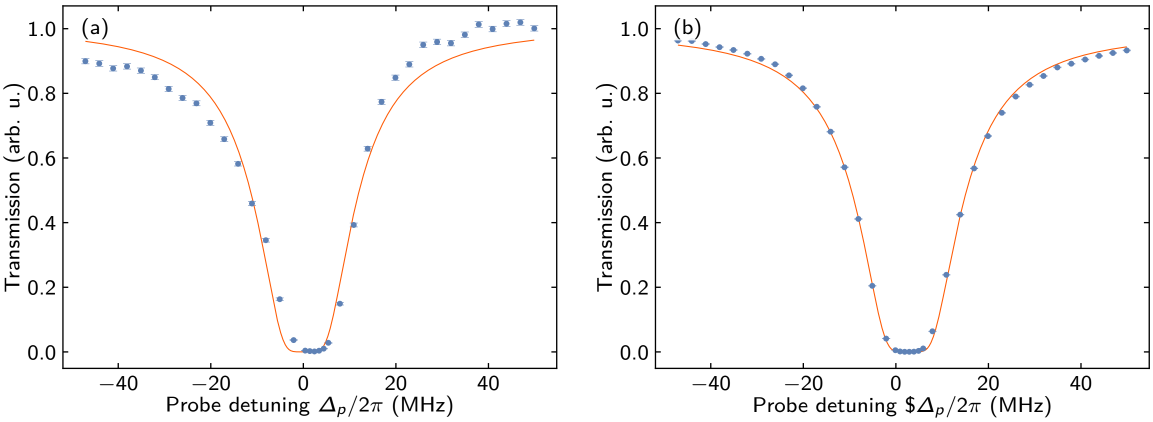

Figure 4.8: Scans of transmission through atom cloud in the dimple trap as function of probe detuning. The solid line is Lorenzian fit to the datapoints and the points are measured data. **a)** The dimple beam is not centered well on the probe beam. **b)** the dimple is aligned in up/down direction to get a symmetric OD. The spots are data points, normalized with reference pulse. Errorbars show standard error of mean.

4.2 is shown in figure 4.6 c). For the imaging along the probe, this alignment becomes more complicated however, since the oblong structure of the dimple trap along the imaging direction makes it hard to image, as the atoms in the dimple beam obscure the view of the cut.

Instead of aligning on the imaging, it is instructive to change to few-photon pulses in the probe instead of a high intensity probe. Scanning the frequency of the probe beam around single photon resonance yields a broad absorption valley from which the optical depth (OD) of the trap can be deduced. Such a scan is shown in figure 4.8. In figure 4.8 a), the dimple beam is not well centered on the probe, and therefore the transmission dip is asymmetric. Careful alignment of the height of the dimple leads to a symmetric transmission dip, as shown in figure 4.8. The solid line is a fit, and the points show the measurements.

The optical depth of the dimple depends not only on the alignment of the dimple beam and the dipole trap onto the probe, but also on a number of other parameters, such as intensities in both the dipole trap beam and the dimple beam and the ramps of these, on the electrical and magnetic fields and the optical pumping. In the end all these parameters determine the final state of the atoms, and hence the temperature of the cloud and whether the atoms can be addressed by the probe.

The position of the atomic cloud along the probe beam is not as critical as the up/down alignment on this beam, but it is still affecting eg. the optical depth. Fortunately, the alignment along the probe is made relatively easy by the fact that the AOD offers the opportunity to change the position of the dimple beam by changing the applied frequency. A scan of the dimple beam across the dipole trap is shown in figure 4.9. This corresponds to moving the dimple across the dipole trap. This scan is done by overlapping the dimple beam with the dipole trap and then ramping the dipole trap intensity off. This releases the atoms outside of the dimple trap. The dipole trap intensity is then ramped back up, yielding further confinement of the dipole trap. If the dimple trap is created outside of the dipole trap, it will not be loaded with atoms, and ramping the dipole trap intensity off results in a release of the atoms. Figure 4.9 a) shows the transmission dip for three different frequencies. The solid lines are fits, while the points are measured values. The figure shows how different positions along the probe yields slightly

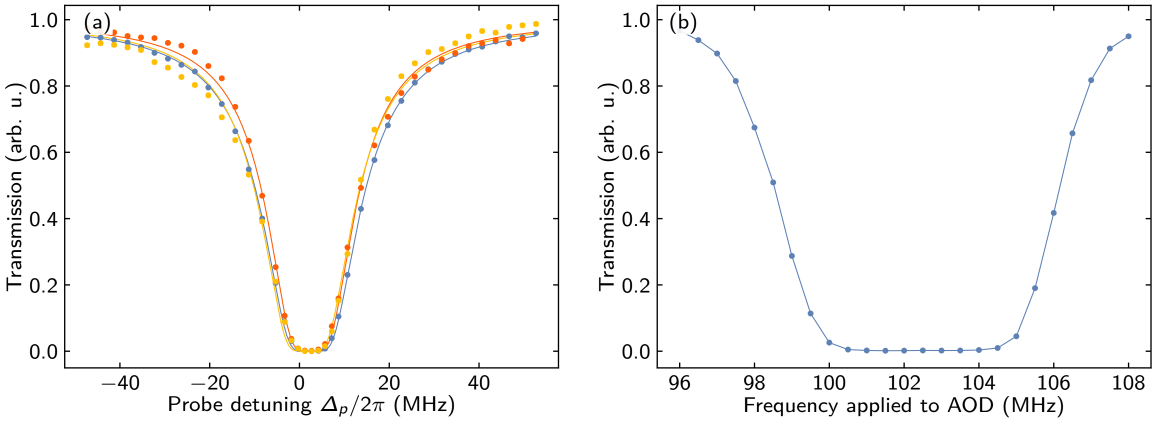

Figure 4.9: Using the frequency applied to the AOD to change align the dimple trap on the dipole trap. **a)** Frequency scan of the probe. The three sets of dots and lines corresponds to three different frequencies of the dimple. The dots are data points, while the solid lines are Lorentzian fits. The blue points and line are for frequency 100.5 MHz, the orange is 99 MHz and the green is 102 MHz. **b)** Frequency scan of frequency applied to the AOD. This corresponds to a move of the dimple trap across the dipole trap. The dipole trap intensity is ramped far down, thus releasing atoms outside of the dimple trap. If the dimple trap is not well overlapped with the dipole trap, only few atoms will be left to interact with the probe light. The scan shown here is for probe light on resonance. The slopes of the absorption valley are slightly different. This indicates that the dimple beam plane has a rotation with respect to the probing plane. Errorbars show standard error of mean.

different transmission curves. Figure 4.9 b) shows a scan of frequencies at probe resonance, showing how the dimple can be moved across the dipole trap.

4.3 Experiments with a single superatom

The results described in chapter 5, were measured with a single dimple trap where the probe and control field detunings were selected to allow adiabatic elimination of the intermediate state as described in section 2.3.1.

When the experiment described in chapter 3 is in the superatom configuration, a few things are changed in the experimental procedure.

In 3.1.2, it was discussed how the atomic population oscillates in the dipole trap after optical pumping. To get a homogeneous density distribution, it is therefore reasonable to introduce a wait time between optical pumping and probing. This is not as critical for the the smaller, deeper dimple trap. This trap does in fact not exhibit these characteristic oscillations on visible scales. For the dimple trap, the frequency of oscillations is expected to me much faster, and the damping is assumed to be much stronger, quickly bringing the atoms back to thermal equilibrium.

Because the dimple laser is not as far from the resonance frequencies, it is expected to cause some heating and hence some loss of atoms in the dimple trap. Therefore, it is preferrable to have only a short time between the optical pumping and the evaporation when the dimple is on, than to keep the atoms long in the trap before evaporation.

For the experimental procedure presented in chapter 3, the intensity of the dipole trap is ramped down during the evaporative cooling step. This becomes even more critical when dimple traps are considered.

If the dimple trap is created at the edge of the dipole trap, or if more than one dimple trap is applied, it is essential that the dipole trap is ramped down before the probing. It is necessary to release all atoms outside of the dimples, as there might otherwise be atoms left trapped outside of the dimple trap. Though the number of such atoms is very low, they are not necessarily within the blockade radius, and hence they can introduce a dramatic error in for instance the number of measured ions.

The dipole trap is switched off during probing as described in section 3.2. The optical depth decreases if the dipole trap is at a constant value between the pulses, as some atoms are lost during the time when the trap is off, and as some atoms are lost when applying the field ionization pulse. Therefore, the dipole trap intensity is ramped across the pulses thereby increasing the density of fewer atoms.

The dimple trap is not ramped off during the probing because the switching of the AOD is relatively slow compared to the switching off for instance an acusto optic modulator (AOM). Though the AOM's used in the experiment use the same crystal as the AOD, the different devices rely on different optical axes of the birefringent crystal, with different sound velocities. Keeping on the dimple trap during probing means that the Raman resonance will be slightly shifted, as the depth of the trap potential has to be subtracted from the ground state energy. This is however not a problem, as the Raman resonance is determined by scanning the probe frequency around the resonance and choosing the peak based on this.

The dimple trap for this ramping scheme yields a single superatom. For the cooling parameters applied, the temperature of rubidium atoms making up the superatom is $\approx 5.9\,\mu\mathrm{K}$. This temperature is estimated from absorption imaging for different times of flight. In these time-of-flight images, the shadow of the cloud is fitted in horizontal and vertical direction with a Gaussian profile. From the expansion of cloud as a function of time-of-flight, the temperature of the cloud can be estimated.

The one-dimensional Gaussian fits are also used to determine the horizontal and vertical density profiles for the ensemble. The final ensemble has $1/e$ of approximately $6.5\,\mu\mathrm{m}$ along the probe direction and $10\,\mu\mathrm{m}$ in y-direction as defined on figure 4.1. The size in the last direction is deduced from the atom number from absorption imaging and optical depth to the probe beam to be $21\,\mu\mathrm{m}$. The optical depth to the probe is on resonance around 9.4. The dimple trap contains around 24 000 atoms.

It should be noted that as the probe beam waist of $6.2\,\mu\mathrm{m}$ is smaller than the size of the ensemble, the number of atoms from absorption imaging is not the number of atoms interacting with light, and hence not the number of atoms which contribute to the collective effects.

The number of atoms in the intersection of the probe is estimated by considering the Gaussian probe beam having a square intensity profile. The intensity is taken to be half the peak intensity and the width of the square profile is two times $1/e^2$. Assuming the probe beam to be this cylindrical beam intersecting a Gaussian density profile with the sizes from absorption imaging, the atom-light interaction can be integrated over the beam-cloud intersection to give the effective atom number. This is found to be 4300 atoms.

The van der Waals coefficient of the $|111S_{1/2}, J = 1/2, m_j = 1/2\rangle$ state is calculated to be $C_6 = 1.88 \times 10^5\,\mathrm{GHz}\,\mu\mathrm{m}^6$ with the Pair Interaction software [28]. The Rabi frequency of the control field is $\Omega = 2\pi \cdot 12\,\mathrm{MHz}$. With these two parameters, the Rydberg blockade radius is sufficiently large to block the entire medium.

For the experiments, the intermediate state of the superatom is adiabatically eliminated. The adiabatic elimination is discussed in section 2.3.1. Here the control light is detuned from the EIT resonance by single photon detuning $\Delta = 2\pi 100\,\mathrm{MHz}$. This detuning is picked as a tradeoff between having long Rydberg state lifetime, as is the case for far off detunings, and having a relatively high absorption, as is the case for small detunings. The probe laser is detuned to be on Raman-resonance for the given control frequency.

Chapter 5

Three-photon correlation

In the previous chapters, the stage for the realization of a Rydberg superatom strongly coupled to light is set. In chapter 2, the theoretical framework for this coupling is described, and in chapters 3 and 4 our experimental realization of such a superatom is discussed.

With the superatom strongly coupled to a weak probe field it is possible to measure light pulse modulations on single photon level. The probe light measured on four single photon counter modules is shown in section 5.1. From this signal, correlation functions of photons can be calculated, as discussed in section 5.2 where the two photon correlation function is presented. Three-photon correlations can also be calculated from the experimental data, but as they depend on three absolute times rather than two a transformation of the data to Jacobi coordinates is introduced in section 5.3. In these new coordinates, the third order correlation can be plotted and investigated. The correlation function is further compared to numerical simulations based on the model presented in section 2.4.

The three-photon correlation function however includes also a signal from two photon correlations with a third spectator photon. To determine the signal stemming exclusively from three-photon correlations, the two photon correlation functions are subtracted from the three-photon correlation function yielding the connected third order correlation function, as further discussed in section 5.5. In the connected correlation function we observe the signature of three-photon correlation. This is the first demonstration of clear structure in the connected third order correlation function for photons interacting in a free space medium.

5.1 Results

As already mentioned in chapter 4, the signal measured is the outgoing probe pulse detected on the SPCMs. The signal is measured in time bins of 20 ns and is further binned in the data treatment. In figure 5.1 the time is binned to 40 ns. The time axis is defined so that $t = 0$ when the Tukey pulse defined in 3.2.1 starts to rise.

The pulses are shown in figure 5.1 for multiple amplitudes along with the resulting outgoing photon signal. The outgoing photon signals show clear Rabi oscillations in the photon rate across the pulse. As the photon rate decreases, the oscillations become less visible as the Rabi frequency decreases.

From the measurements at different amplitudes, three photon rates were chosen, a 'low' photon rate of $\mathcal{R}_{in} = 3.4\,\mu\text{s}^{-1}$, corresponding to a mean photon number of $\bar{N} = 19.9$ in each pulse, an intermediate photon rate $\mathcal{R}_{\text{in}} = 6.7\,\mu\text{s}^{-1}$, which corresponds to $\bar{N} = 39.2$ photons, and a 'high' photon rate of $\mathcal{R}_{\text{in}} = 15.2\,\mu\text{s}^{-1}$, corresponding to a mean photon number of $\bar{N} = 88.3$ photons in each experiment.

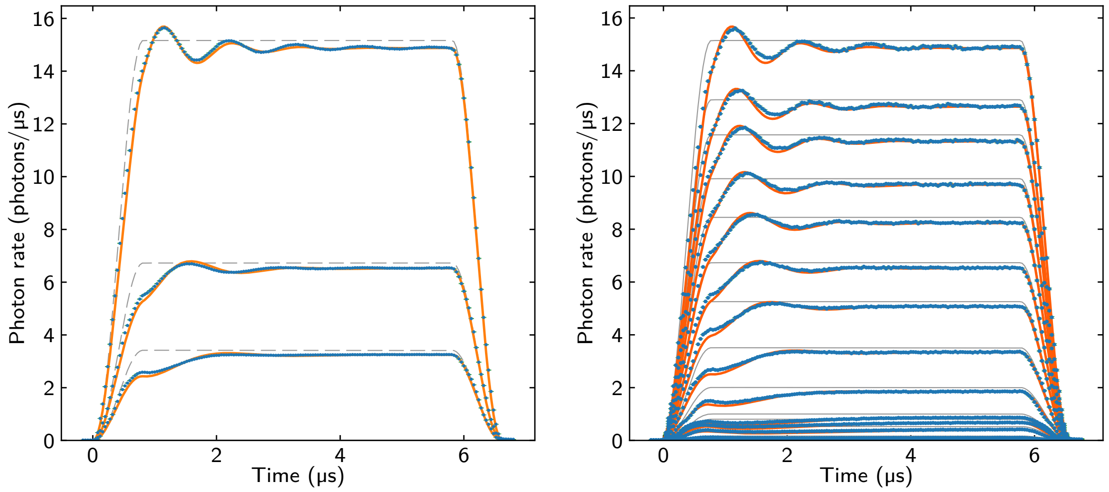

Figure 5.1: Pulse modification by superatom. **a)** time trace of measured pulse with and without superatom. The dashed lines are measured in the reference pulses and show the Tukey pulses at different amplitudes. The bullets are datapoints for three different lines are measured in the real pulses with a single superatom. **b)** Time traces for the three long measurements of the same amplitude for three amplitudes.

For each of these values, a series of experiments as described in chapters 3 and 4 were performed. To obtain sufficient statistical significance, we aimed for more than 900 times 1000 experiments for each photon rate.

5.1.1 Extraction of fit parameters

The time trace measurements shown in figure 5.1 were used to fit the parameters described in section 2.3. With these parameters, theoretical simulations of the time evolution of a similar system were performed, in order to compare the measured three-photon correlations with the values predicted by theory [19].

The fits are shown in figure 5.1 a) and b) as orange lines. For the final figure, the model was only fitted to the correlation measurements, but for the amplitude measurements shown in figure 5.1, the parameters still yield qualitatively good fits.

As seen in the figure, the fits are not fully capturing the oscillations at the end of the high photon rate pulses. This is mainly due to the system not being fully stable in time. For long measurement times, the atom number will fluctuate due to even very small drifts in the setup.

For the fit shown in figure 5.1, the fit values are $\kappa = 0.55\,\mu\mathrm{s}^{-1}$, $\gamma_D = 1.49\,\mu\mathrm{s}^{-1}$, and $\Gamma = 0.14\,\mu\mathrm{s}^{-1}$. This corresponds to the values of the master equation, equation 2.4.18, in section 2.4. The variable κ determines the coupling between the superatom and a probe photon, Γ is the spontaneous decay rate, and γ_D is the dephasing of the bright state of the superatom into the dark states.

In comparison to earlier results, the coupling with the light has increased substantially, and the same applies to the decay and dephasing terms, compared to the previous measurements on a similar system [19]. The increased decay means that the probability of the superatom to emit in forward direction will be lower. This probability is measured with the parameter β, which measures the fraction of the total emission that goes into the mode of the probe,

$$\beta = \frac{\kappa}{\kappa + \Gamma} = 0.80. \tag{5.1.1}$$

In the earlier experiment the parameter was 0.86 [19]. This difference can be assigned to the slight differences between the previous and the current realization of a superatom, but also to the fit, as discussed in section 5.1.

The fact that especially the late oscillations at high photon rates are damped too much in the fits indicates that some dynamics of the system are not captured by the model. This could as discussed be caused by fluctuations in atom number in the experiment. The fit parameters can be tweaked to capture these late oscillations better, but this introduces unphysical oscillations in the already fully damped low photon rate pulse.

5.2 Correlation functions

To investigate the interactions between photons, we measure the correlation function between photons leaving the medium [16]. Correlation functions are used in many branches of physics, from quantum field theory to classical statistical physics [15]. In quantum optics with Rydberg atoms, two photon correlations are used to show both attraction and repulsion between photons mediated by quantum nonlinear media [8, 30].

Three-photon correlations have been measured elsewhere, both in cavity systems [43, 44, 45], and recently in a free space system [20], however in a system of propagating polaritons rather than with a superatom. Through this work the correlation functions describe the modulation introduced by the Rydberg superatom on the light pulse [].

To describe correlations between photons, we apply the quantum field theory correlation function, which is defined analogously to the classical correlation function. For correlations between an observable ϕ depending on a variable x, the correlation function of i'th order is given by

$$g^{(i)}(x_1, x_2, \cdots, x_i) = \frac{\langle \phi(x_1)\phi(x_2)\cdots\phi(x_i)\rangle}{\langle \phi(x_1)\rangle\langle \phi(x_2)\rangle\cdots\langle \phi(x_i)\rangle}. \tag{5.2.1}$$

This function is already normalized [15].

The expectation of the photon flux for the model from section 2.4, is $\langle E^\dagger(t)E(t)\rangle$ [19], and hence it follows that the second order correlation function for photons is

$$g^{(2)} = \frac{\langle E^\dagger(t_1)E^\dagger(t_2)E(t_2)E(t_1)\rangle}{\langle E^\dagger(t_1)E(t_1)\rangle\langle E^\dagger(t_2)E(t_2)\rangle}. \tag{5.2.2}$$

This second order correlation function gives the correlation between two photons arriving at times t_1 and t_2 on the counters. In the experiment, the time trace of arriving photons are measured with the four single photon counter modules. For each experiment, the correlation function is found by counting when photons arrive within the same time bins on the counters.

Two photon correlation function

Figure 5.2 shows the measured $g^{(2)}$. The main feature of $g^{(2)}$ is the strong correlation line along the diagonal, corresponding to two photon bunching [30]. The darker bands along the two photon bunching line arise from the rearrangement of nearby photons into the peak. For high photon rates $g^{(2)}$ shows strong oscillation structures, while for lower photon rates the main

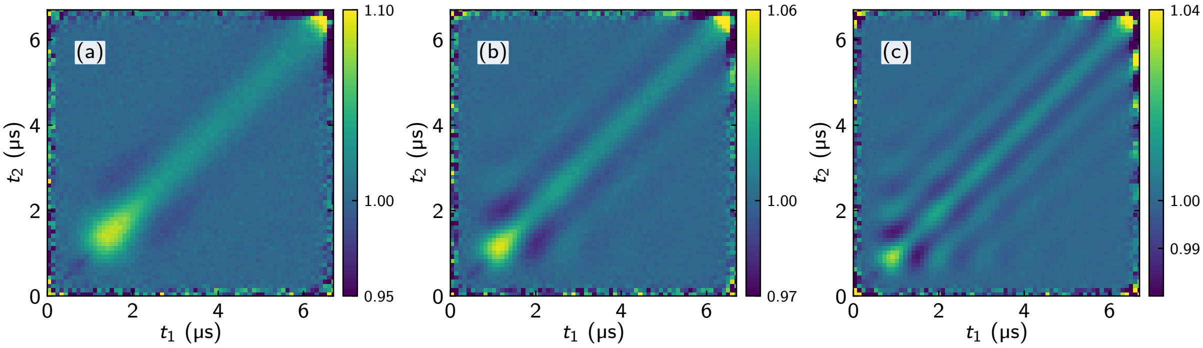

Figure 5.2: $g^{(2)}$ for tree different photon rates. The subfigures shown here correspond to **a)** $R = 2.5\sqrt{3}$µs, **b)** $R = 3.0\sqrt{3}$µs, and **c)** $R = 3.5\sqrt{3}$µs.

feature is broader, and the oscillations are slower. On the other hand, the signal is higher for the low photon rate, as seen on the color map. This is due to the correlations being a relative effect, and for the low photon rate, the relative pulse modulation is much stronger than for the high photon rate case, hence the stronger correlation signal.

In figure 5.2 $g^{(2)}$ is plotted as a function of absolute times, $g^{(2)} = g^{(2)}(t_1, t_2)$. Often $g^{(2)}$ is plotted as a function of time differences, so that $g^{(2)} = g^{(2)}(t_2 - t_1)$ but this holds only for the specific case of steady state [46]. Here the system does not go fully to steady state, which is also seen in figure 5.2, where oscillations are seen along the diagonals. The oscillations again reflect the oscillations seen in figure 5.1 a).

Three-photon correlation function

Following equation 5.2.1, the third order correlation function of photons for the system described in the model is

$$g^{(3)}(t_1, t_2, t_3) = \frac{\langle E^\dagger(t_1)E^\dagger(t_2)E^\dagger(t_3)E(t_3)E(t_2)E(t_1)\rangle}{\langle E^\dagger(t_1)E(t_1)\rangle\langle E^\dagger(t_2)E(t_2)\rangle\langle E^\dagger(t_3)E(t_3)\rangle}, \tag{5.2.3}$$

This equation gives the correlation between three photons arriving at t_1, t_2 and t_3 on three counters. In this setup, the correlation functions can be read off directly, as the photon detection traces are measured on four single photon counters.

5.3 Jacobi coordinates

The third order correlation function $g^{(3)}$ is a four-dimensional data set, i.e. a value is assigned to each time triple (t_1, t_2, t_3). In order to image such a dataset in a meaningful way, it is instructive to transform data in Jacobi coordinates [47]. Jacobi coordinates are often used for visualizing many-body problems, because they offer an often more meaningful choice of coordinates for two dimensional plots than absolute time or space coordinates.

The three-dimensional Jacobi coordinates consist of a center of mass coordinate R and two relative coordinates η and ζ corresponding to a coordinate of relative distance between two of three particles and a coordinate of distance between the last particle and the center of mass of the other two respectively.

$$R = \frac{1}{\sqrt{3}}(t_1 + t_2 + t_3), \qquad \eta = \frac{1}{\sqrt{2}}(t_1 - t_2), \qquad \zeta = \sqrt{\frac{2}{3}}\left(\frac{t_1 + t_2}{2} - t_3\right). \tag{5.3.1}$$

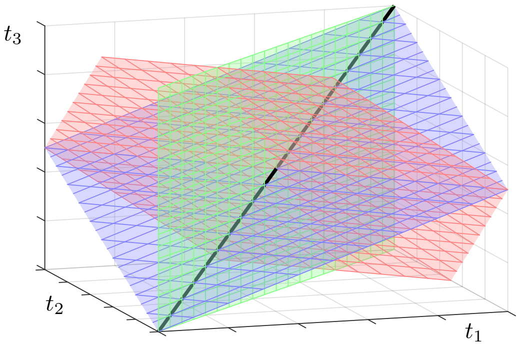

Figure 5.3: Jacobi coordinates plotted as planes. The red plane is orthogonal to R, the green to η, and the blue to ζ. One notices how the planes are orthogonal, and how the R-plane, which is plotted for $R = 1/2R_{\text{max}}$ is a regular hexagon.

If the three-dimensional data set is considered a cubic matrix of values, specific values of R corresponds to planes normal to the diagonal from the point $(t_1, t_2, t_3) = (0, 0, 0)$ to $(t_1, t_2, t_3) = (t_{\text{final}}, t_{\text{final}}, t_{\text{final}})$.

The relative coordinates η and ζ are orthogonal to R. This is seen by defining unit vectors,

$$R = \frac{1}{\sqrt{3}}\begin{pmatrix}1\\1\\1\end{pmatrix}, \qquad \eta = \frac{1}{\sqrt{2}}\begin{pmatrix}1\\-1\\0\end{pmatrix}, \qquad \zeta = \frac{1}{\sqrt{2}}\begin{pmatrix}1/2\\1/2\\-1\end{pmatrix}. \tag{5.3.2}$$

It is easily shown that the dot product of each pair of the vectors equal zero, and hence that they are orthogonal.

The coordinates are illustrated in figure 5.3. In time domain, the coordinates correspond to a mean time R, the time difference between two of three times η, and difference between the mean time of two times and the third time ζ. The coordinates are illustrated for photons in figure 5.4.

In the steady state case, there is no dependence on the center of mass coordinate, as the center of mass coordinate drops out of the effective potential for three-body interactions [47]. The experiments performed here do not reach steady state, but this is one of the main motivations to go to Jacobi coordinates: In jacobi coordinates one has a natural coordinate to average out, thus reducing four-dimensions to three.

The restrictions on the relative coordinates as a function of R in a cube with $0 \leq R \leq R_{\text{max}}$ can be described with

$$\eta \in \begin{cases} [-\sqrt{3/2}R;\ \sqrt{3/2}R] & \text{if } R < 1/3R_{\text{max}}, \\ [-\sqrt{1/6}R_{\text{max}};\ \sqrt{1/6}R_{\text{max}}] & \text{if } 1/3R_{\text{max}} \leq R < 2/3R_{\text{max}}, \\ [-\sqrt{3/2}(R_{\text{max}} - R);\ \sqrt{3/2}(R_{\text{max}} - R)] & \text{if } 2/3R_{\text{max}} \leq R \end{cases} \tag{5.3.3}$$

and for a given set of R and η the restrictions on ζ are given by

$$\zeta \in \begin{cases} [\sqrt{3}|\eta| - \sqrt{2}R;\ \sqrt{1/2}R] & \text{if } R < 1/3R_{\text{max}} \\ [\max(-\sqrt{2}R + \sqrt{3}|\eta|, -\sqrt{1/2}(R_{\text{max}} - R)); & \\ \qquad \min(\sqrt{2}(R_{\text{max}} - R) - \sqrt{3}|\eta|, \sqrt{1/2}R)] & \text{if } 1/3R_{\text{max}} \leq R < 2/3R_{\text{max}} \\ [-\sqrt{1/2}(R_{\text{max}} - R);\ \sqrt{2}(R_{\text{max}} - R) - \sqrt{3}|\eta|] & \text{if } 2/3R_{\text{max}} \leq R \end{cases} \tag{5.3.4}$$

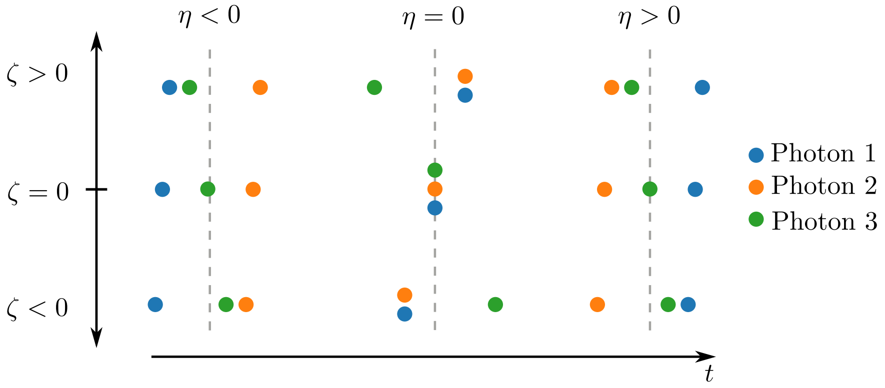

Figure 5.4: Jacobi coordinates illustrated as time spacing between photons. Here it is assumed that photon 1 is detected on counter 1 at time t_1, photon 2 is detected at counter 2 at t_2 and photon 3 is detected on counter 3, thus determining the value of t_3. The grey lines show the center of mass for the photons. For $\eta, \zeta = 0$, the three photons arrive at the same time. $\eta = 0$ always correspond to photon 1 and 2 arriving simultaneous, while for $\zeta = 0$, the third photon arrives exactly at the mean time of the arrival of photon 1 and 2. Negative ζ mean that the third photon arrives before the center of mass of the three photons, while positive ζ mean that photon 3 arrives after the center of mass.

As seen from the above expressions, η is a hexagon, rising with R to a flat top of value $\sqrt{1/6}R_{\max}$ and then dropping again with $R_{\max} - R$ towards the end. ζ is expressed in terms of both R and η. Together these maximal values will, for a given R, outline the R-plane within the cube.

In the expression for ζ, the first term in the maximum and minimum brackets corresponds to the cut off of triangle tips.

5.3.1 Binning of data points

The shape of the R-planes reflects the placement of the datapoints. This is seen in figure 5.5 a). The data points for a plane in R lies shifted in η and ζ with respect to the two following planed so that a point (η, ζ) only occurs in every third R-plane. This gives rise to empty data points, and in order to exclude those, R is binned in bins of three R-planes. The distance between the time binns in real time is $\sqrt{3} \cdot 0.1\,\mu\text{s}$.

The binning of R means that η and ζ will lie shifted with respect to each other in a hexagonal lattice pattern. Translating the hexagonal lattice pattern onto a rectangular grid gives rise to a checker board pattern with every second bin being empty. Therefore, η and ζ are further binned to give a pattern without any empty bins.

5.3.2 Averaging over R

As seen in figure 5.2 $g^{(2)}$ is not independent of the corresponding center of mass coordinate $\sqrt{1/2}(t_1 + t_2)$. Thus, there is no reason to assume that $g^{(3)}$ is independent of R either. Therefore, it is to some extend not meaningful to mean over many values of R. On the other hand, without an averaging over R, the data easily becomes relatively noisy, and the averaging over R can be justified as long as the theoretical values are averaged in a similar way. To conclude something

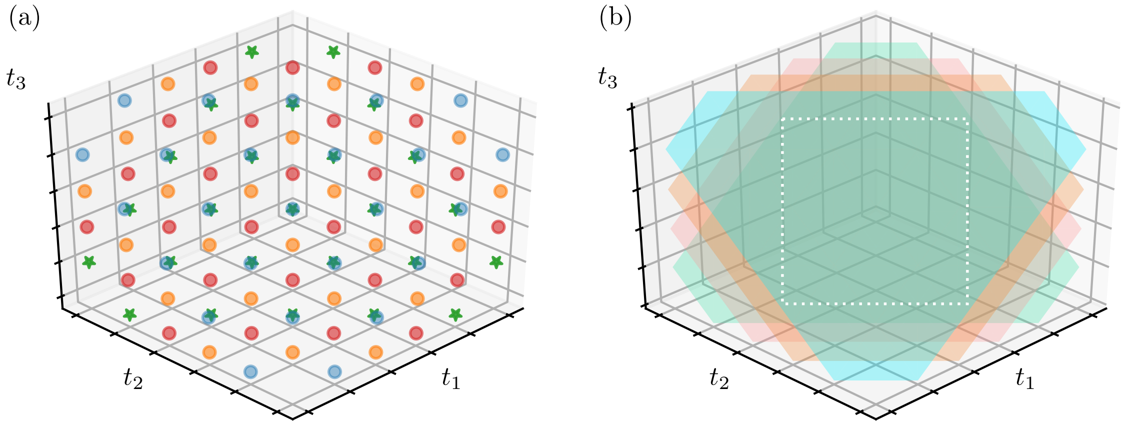

Figure 5.5: Visualization of datapoints in Jacobi coordinates. **a)** The hexagonal lattice pattern of coordinates in different R planes which makes binning of R necessary. As seen in the figure, the blue, orange, and red points have no overlap with each other, but the green points, which are far in the background, are overlapping with the blue points. When the binning is done, blue, orange and red points will all be contained in one plane of R, while the green points indicate the start of a new plane. **b)** For a range of R, not all planes contribute to the same points. In this figure, the purple and green semi-triangles have only overlap in the central hexagon. The drawn square shows how figures are cut so that all points get contributions from the same amount of R planes.

from the averaged data, it is further assumed that the signal does not change much in the R-direction on the time scales of the averaging.

Due to the shapes of the R-planes, (η, ζ)-coordinates far from $(0, 0)$ will not be contained in all planes contributing to the average. This is shown in figure 5.5 a) and b). In figure 5.5a) the blue points will not be contained in the plane of R which contains the green stars. In figure 5.5 b) it is seen more clearly how four planes of R all have regions not contained in any other planes. This uniqueness of points is only true in the region where the planes of R are hexagonal. When averaging it should be taken into account that points for large $|\eta|, |\zeta|$ will have different number of R-plane contributions than points η, ζ around zero.

To present the data in the most meaningful way, the η- and ζ-axes are therefore limited so plots only include data where every point (η, ζ) has the same number of contributing R-planes. This is illustrated in figure 5.5 b), where the outlined square shows the area where all points have the same number of contributing R-planes.

To find where to cut η and ζ the relations given in equations 5.3.3 and 5.3.4 are exploited. In this case R for the averaging is chosen to start relatively close to $R_{\max}/3$, and the largest R is around ${}^{R_{\max}}/_{2}$. This means that the smallest area over which the same averaging can be done is given by the plane for the smallest value of R. A plane for this value of R is then a downward pointing triangle with cut off tips. The largest square which can possibly fit within this shape has its side lengths determined by the main triangle. This is illustrated with the dashed square in figure 5.5b).

Equation 5.3.4 gives the bounds on ζ for a given R and η, which for this triangle is

$$\zeta = \sqrt{3}|\eta| - \sqrt{2}R \tag{5.3.5}$$

To find the largest allowed side length, the value of η is chosen to be η_0 such that for $\eta_0 > 0$, $\zeta(\eta_0) = \eta_0$.

$$\eta_0 = -\left(\sqrt{3}\eta_0 - \sqrt{2}R\right) \tag{5.3.6}$$

$$= \frac{\sqrt{2}}{\sqrt{3}+1}R. \tag{5.3.7}$$

Further the area plotted is narrowed down such that the first points on the Tukey pulse do not contribute to the shown part of the figure. These points contribute mainly noise as they have low signal to noise ratio. This is seen for $g^{(2)}$ in figure 5.2, which has a noisy frame reflecting the early rise and late decrease of the Tukey pulse.

To produce the figures in the following sections, the average is taken from $R = 2.5\sqrt{3}$µs to $R = 3.5\sqrt{3}$µs. In realtime this corresponds to a 1 µs interval. The full pulse time is 6.6 µs, but to avoid including the data from the rise of the pulse, the cut must be made so that the first part of the rising pulse is not included in the shown η, ζ-range.

Therefore η and ζ are calculated for $R = 2.3\sqrt{3}$µs. For this R-value, $\eta_0 = 2.06$ µs, and therefore the figures are cut to the range $[-2\text{µs}; 2\text{µs}]$ for both η and ζ.

5.4 Third order correlation function

Plots of the measured third order correlation function are shown in figure 5.6a), b) and c). They all clearly show a six-fold symmetric structure. The structure is expected, as it reflects the possible permutations of photons on the three counters.

In $g^{(3)}$, the main features are the three crossed photon bunching bands [30]. These three bands correspond to two photons arriving almost simultaneously on two counters. This structure is the same as what is seen in the $g^{(2)}$ plots in figure 5.2. The structures are accumulating along $\eta = 0$, and along around $\zeta = \pm\eta/\sqrt{3}$ respectively[1]. These bands are caused by two photon correlations [30], and the width of the bands depend on the photon rate. For low photon rates the main bunching effect is wider, while for higher photon rates the main peak is narrower but accompanied by higher order peaks further out along the lines. These bands of oscillations are also visible in figure 5.2, which shows two photon correlations.

The width of the bunching line is determined by the Rabi frequency of the oscillations. As the Rabi frequency is proportional to the intensity of the incoming field, see equation 2.1.17, a high incoming photon rate will lead to faster dynamics.

It is further apparent that the two photon lines in $g^{(3)}$ are stronger along the three lines that span a downward pointing triangle. The same tendency exist for the simulated results, but it is much less pronounced.

The experimentally measured $g^{(3)}$ can be compared to numerical simulations of the same system. The simulations are shown in figure 5.6 d), e), and f). The simulations shown are based on the model introduced in section 2.4. The master equation, equation 2.4.18, is used, assuming a coherent incoming pulse similar to the one used in the experiment. The simulations shown here and in the paper are a courtesy of Jan Kumlin, Universität Stuttgart. Similar simulations have already been shown for $g^{(2)}$ [19], yielding a good agreement between theory and experiments.

Comparing the measured $g^{(3)}$ in figure 5.6, a), b), c) to the simulated results, figure 5.6 d), e), and f), the same good qualitative agreement which is seen for $g^{(2)}$ [19] is also clear for $g^{(3)}$. It

---

[1] This factor follows from the consideration of two photons arriving at the same time. $\eta = 0$ represents the case where $t_1 = t_2$, while setting $t_3 = t_2$ and $t_3 = t_1$ in the expression for ζ yields the factors $\pm 1/3$.

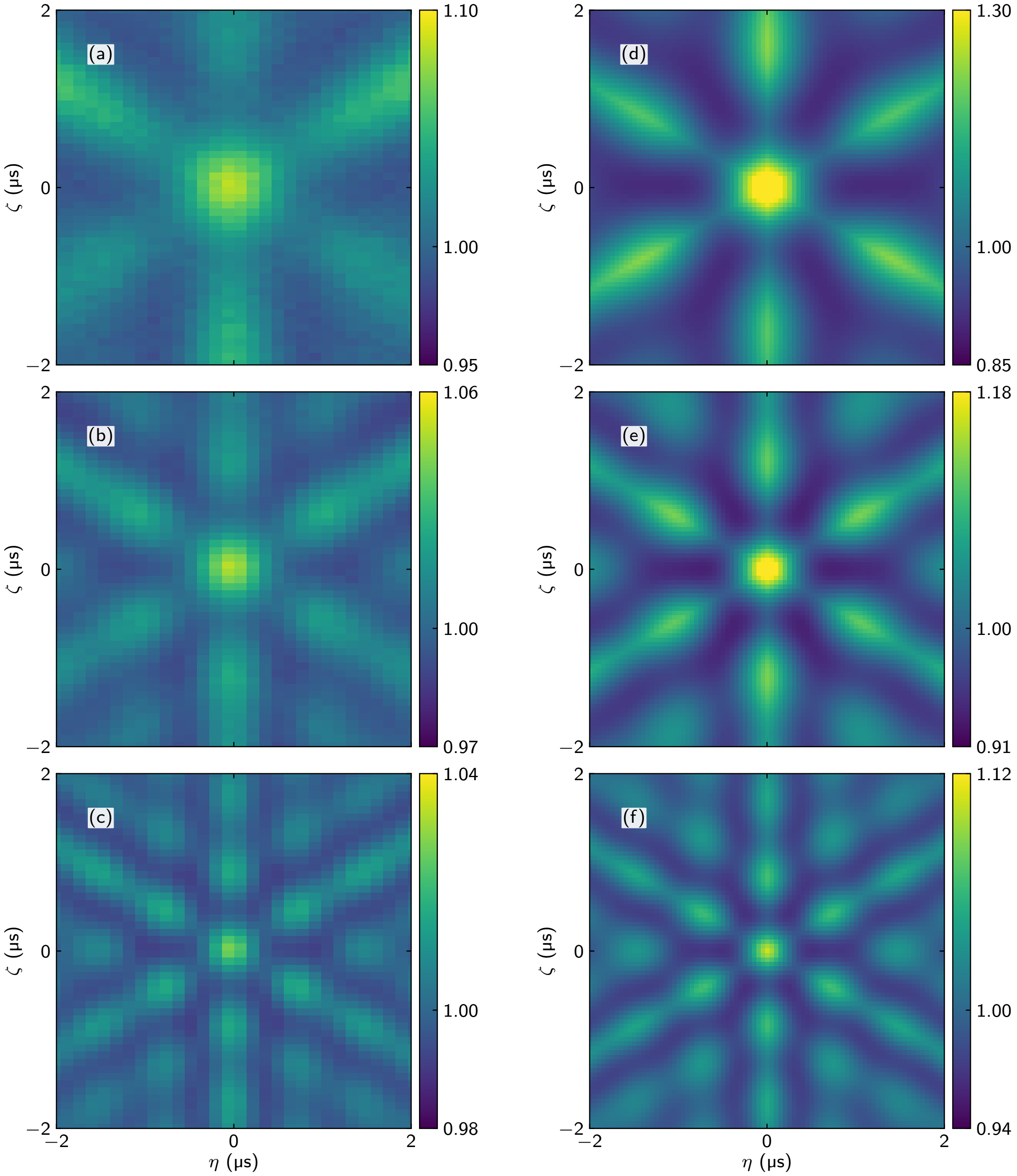

Figure 5.6: The third order correlation function $g^{(3)}$ for different photon rates $\mathcal{R}_{\text{in}}$, experimental results (a,b,c) and theoretical results (d,e,f). **a)** and **d)** are measured results and simulated results respectively for $\mathcal{R}_{\text{in}} = 3.4\,\mu\text{s}^{-1}$, **b)** and **e)** are measured results and simulated results for $\mathcal{R}_{\text{in}} = 6.7\,\mu\text{s}^{-1}$ respectively, and **c)** and **f)** are the experimental **e)** and the simulated **f)** results for $\mathcal{R}_{\text{in}} = 15.2\,\mu\text{s}^{-1}$. The simulated results are a courtesy of Jan Kumlin, Universität Stuttgart.

is worth noticing that close to the central correlation peak, the experimental data do not show the structure of antibunching along the bunching line as strongly, as the simulations suggest. This is especially the case for the low photon rate, figure 5.6a), while the experimental data for higher photon rates, figures 5.6b) and c) have these features more prominently. The bands of bunching for the experimental plots are also broader than the bands in $g^{(3)}$ from simulations, especially for low photon rate, as shown in figures 5.6a) and d).

The quantitative agreement the simulated correlations and the measured correlations should also be noted. The difference in the scale of the effect is relatively large. The range of the color bars around one is here for the experimental results chosen to be a factor three smaller than the values for the corresponding simulated data.. Thus for photon rate $\mathcal{R}_{\text{in}} = 15.3\mu\text{s}^{-1}$ the experimentally measured $g^{(3)}$ has a color scale spanning 0.06 units of $g^{(3)}$, whereas the color scale of the corresponding simulated $g^{(3)}$ is chosen to span 0.18 units.

The discrepancy is assumed to be due to the noise induced by the experimental setup. As already mentioned, thermal motion of the atoms is a main dephasing mechanism of the system, and it will cause damping of the outgoing signal. A similar quantitative difference is seen for the two photon correlation function [19], but to a smaller degree. This qualitative agreement is however relatively good, as already discussed.

However the results presented in figure 5.6 have a different binning for experimentally measured $g^{(3)}$ and simulated $g^{(3)}$, which can result in some smearing of peak values for the measured values.

5.5 Connected correlation function

The order of a correlation function gives the highest order of correlations contributing to the correlation function. However, lower order correlations will also contribute, and hence $g^{(3)}$ contains information about two photon correlations on top of information about correlation between three photons.

The main feature in $g^{(3)}$ is identical to verify features seen in $g^{(2)}$. In order to see that the signal actually stems from two body correlations with a third random spectator photon, it is useful to compare $g^{(3)}$ to the sum of $g^{(2)}$ for the three axes, that is

$$\sum_{i<j} g^{(2)}(t_i, t_j). \tag{5.5.1}$$

This sum is illustrated in Jacobi coordinates in figure 5.7. The resulting pattern is clearly almost identical to the structure seen in the corresponding experimentally measured $g^{(3)}$ in figure 5.6.

This clearly shows that the main component of $g^{(3)}$ stems from two body correlations. As two body correlations in this system is expected to everywhere be much stronger than the signal from pure three-body correlations, the latter will be mostly hidden in the $g^{(2)}$ structure of $g^{(3)}$.

To extract the pure three-body correlations, it is therefore necessary to exclude the signal stemming from pure correlations between two photons. Following the argumentation for figure 5.7, a natural quantity to subtract from $g^{(3)}$ is the sum of $g^{(2)}$. This yields the connected third order correlation $g^{(3)}_{\text{conn}}$. $g^{(3)}_{\text{conn}}$ is defined as [47]

$$g^{(3)}_{\text{max}} = 2 + g^{(3)}(t_1, t_2, t_3) - \sum_{i<j} g^{(2)}(t_i, t_j). \tag{5.5.2}$$

$g^{(3)}_{\text{conn}}$ will be seen as a measure of the pure three-body correlations. The addition of 2 ensures that the signal in $g^{(3)}_{\text{conn}}$ is zero, when no pure three-body correlations contribute. Thus it is

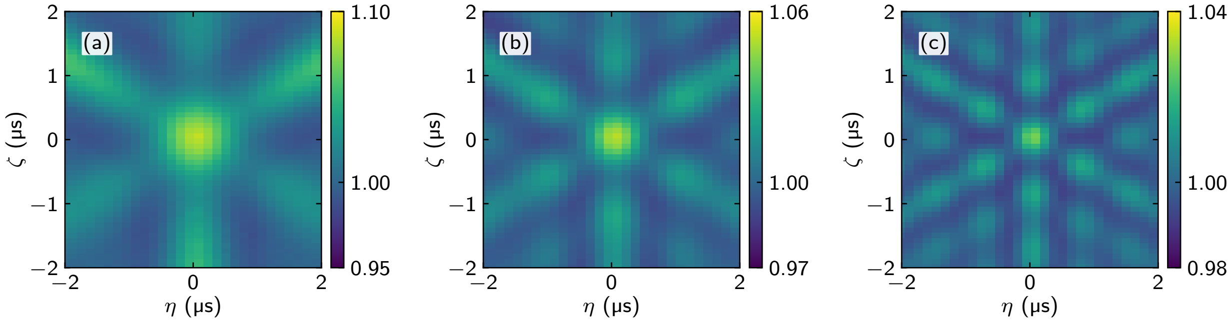

Figure 5.7: The sum of $g^{(2)}$ for all permutations of three times. The three subfigures show the sum of the experimentally measured $g^{(2)}$ for different photon rates, $\mathcal{R}_{\text{in}}$. **a)** for $\mathcal{R}_{\text{in}} = 3.4\,\mu\text{s}^{-1}$, **b)** for $\mathcal{R}_{\text{in}} = 6.7\,\mu\text{s}^{-1}$, and **c)** for $\mathcal{R}_{\text{in}} = 15.2\,\mu\text{s}^{-1}$.

ensured that $g^{(3)}_{\text{conn}}$ is zero both for a system without any correlations and for systems without true correlations between three or more components.

The connected correlation function can also be derived in a rigorously mathematical manner [47] As it will be shown in figure 5.8, signal of the pure three-body correlations are orders of magnitude smaller than the signal from two body correlations, and therefore the measured $g^{(3)}$ is qualitatively indistinguishable from the sum of $g^{(2)}$'s.

5.5.1 Connected third order correlation function

The structure of two photon interaction is clearly visible in figure 5.6, completely obscuring any structure emerging from higher order effects. Higher order effects are however present, and can be seen in the connected third order correlation function $g^{(3)}_{\text{conn}}$. This is seen in figure 5.8a), b), c), where $g^{(3)}_{\text{conn}}$ is plotted for three photon rates for the same values of R as is used for $g^{(3)}$ in figure 5.6. $g^{(3)}_{\text{conn}}$ has a completely different pattern than $g^{(3)}$. This pattern reflects correlations between more than two photons. For $g^{(3)}_{\text{conn}}$ there are no highly expressed band structures reflecting two photon effects. Instead the three experimental figures for $g^{(3)}_{\text{conn}}$ all share the same structure with a narrow peak of bunching in the center, and then rings of antibunching and bunching. The rings are not fully circular, especially not for higher photon rates, they have the expected six-fold symmetry. This hexagonal shape is most clearly seen in figure 5.8 c), where bunching-antibunching oscillation can be followed to at least the third ring of antibunching.

As for the two photon correlations, the results for high photon rate shows stronger oscillations in the correlations than the results for low photon rate, while the duration of each feature in the low photon case is much longer than the corresponding duration for higher photon rates. This is again a feature of damping being greater for low photon while the oscillation frequency is smaller for this case. For the same reason, the central peak of bunching is much wider for low photon rates than for high photon rates.

Though the six-fold symmetry predicted by theory is expressed in figure 5.8, it is worth noting that especially for figure 5.8 d) and e), a triangular bias is visible within the six-fold symmetric structure. This is caused by the same effect which causes the similar bias in figure 5.6 a), namely the finite size of the pulse which causes the absolute times to contribute different signals.

The six-fold symmetry is also predicted by the simulated values, which are shown in 5.8 e-f. Comparing the measured $g^{(3)}_{\text{conn}}$ with the simulated results yields a less directly similarity than for $g^{(3)}$. In the theoretical figures of 5.8, the six-fold symmetry of $g^{(3)}_{\text{conn}}$ is not very pronounced,

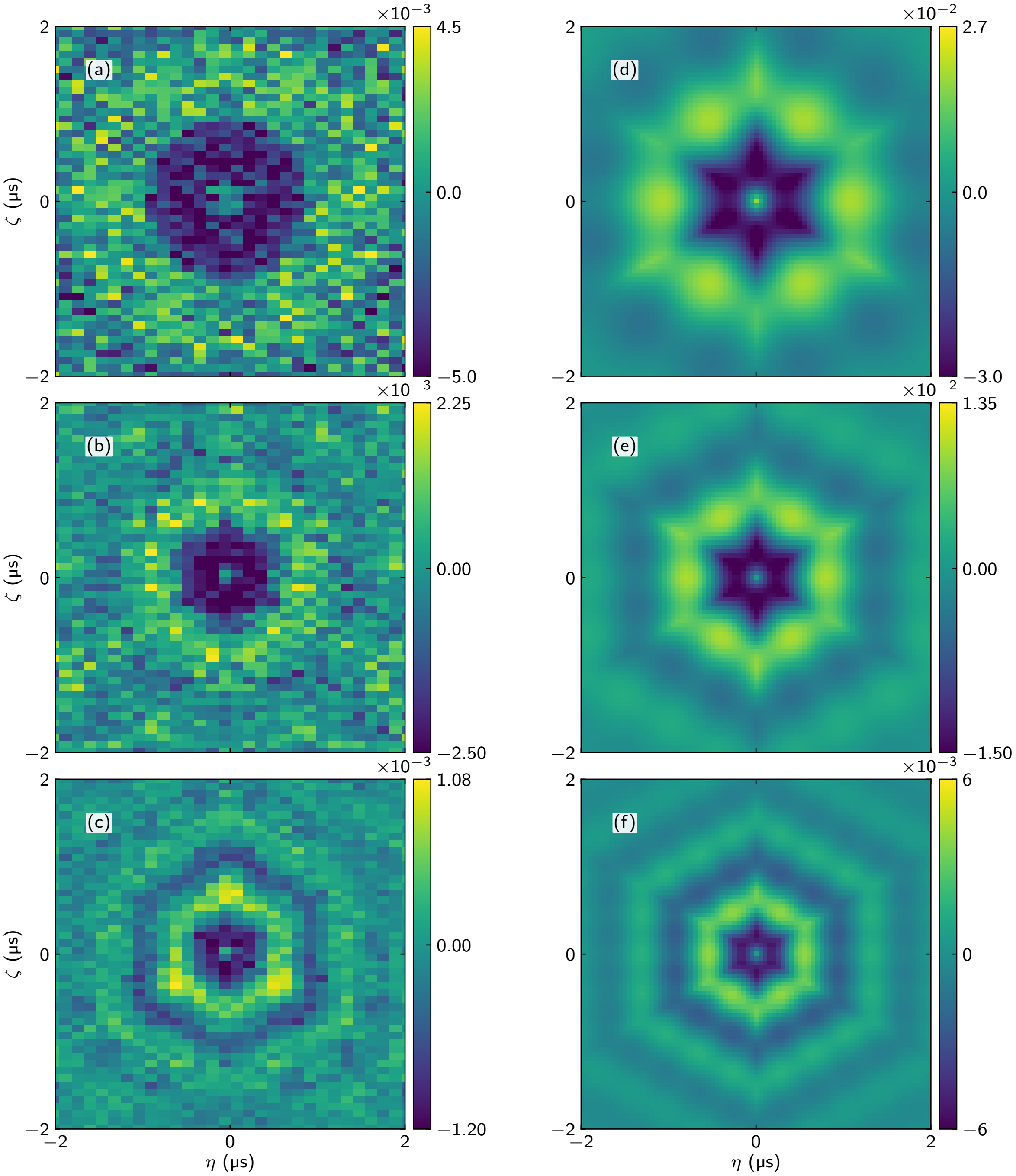

Figure 5.8: Connected third order correlation function $g^{(3)}_{\mathrm{conn}}$ for different photon rates $\mathcal{R}_{\mathrm{in}}$, experimental results and theoretical results. **a)** and **d)** are measured results and simulated results respectively for $\mathcal{R}_{\mathrm{in}} = 3.4\,\mu\mathrm{s}^{-1}$, **b)** and **e)** are measured results and simulated results for $\mathcal{R}_{\mathrm{in}} = 6.7\,\mu\mathrm{s}^{-1}$ respectively, and **c)** and **f)** are the experimental c) and the simulated f) results for $\mathcal{R}_{\mathrm{in}} = 15.2\,\mu\mathrm{s}^{-1}$. The simulated results are a courtesy of Jan Kumlin, Universität Stuttgart.

especially for the low photon rate, figure 5.8a) the shape of the central, uncorrelated area is quite circular. However, around this circle, a darker star shape is faintly recognizable in the first ring of correlation. The same star shape is found in the intermediate photon rate shown in figure 5.8 b).

The less good agreement is caused by a number of factors. The signal in both $g^{(3)}$ and $g^{(3)}_{\mathrm{conn}}$ is far smaller than $g^{(2)}$, resulting in a lower signal to noise ratio. This less good agreement between the theoretical prediction of the pulse shape and the measurements was also observed for the fits in figure 5.1. This is mainly due to instability of the atomic cloud over long measurements; the noise introduced by instability in for instance cloud position and atom number reduces the similarity between the theoretical values and the measured values.

The qualitative agreement of the simulated results with the experimental results is less good than for $g^{(3)}$, where the range of the color bar had been scaled with a factor three. For $g^{(3)}_{\mathrm{conn}}$, this factor is chosen to be six for the low and intermediate photon rates and to be a factor of five for the high photon rate case. This difference for three different photon rates is due to the degree of noise in the data. For the photon rate $\mathcal{R}_{\mathrm{in}} = 3.4\,\mu\mathrm{s}^{-1}$, the highest signal is found, but also the lowest signal to noise ratio. The high signal is due to the relative effect of a single photon modulation being higher for a small pulse amplitude than for a high pulse amplitude. On the other hand, the noise is higher due to the lower number of photons detected in each experiment. As signal to noise scales with photon rate, the low photon rate measurements should in principle have been extended for much longer.

5.5.2 Reference pulses

The signal in $g^{(3)}_{\mathrm{conn}}$ is in sharp contrast to the signal from the reference experiments, as seen in figure 5.9. Since the reference experiments are performed without a medium, no correlations are expected, neither in $g^{(2)}$ nor $g^{(3)}$ or $g^{(3)}_{\mathrm{conn}}$. Figure 5.9 a) and b) show $g^{(2)}$ and $g^{(3)}_{\mathrm{conn}}$ respectively for $\mathcal{R}_{\mathrm{in}} = 3.4\,\mu\mathrm{s}^{-1}$. The lowest photon rate is chosen for no particular reason. The corresponding figures for higher photon rates look similar.

Figure 5.9a) shows $g^{(2)}$ being flat around 1. This is exactly what is expected for coherent laser light, and shows that the laser is very stable over the experiments.

It is worth to notice the colorbar range for the reference $g^{(3)}_{\mathrm{conn}}$, which is orders of magnitude larger than the scale for $g^{(3)}_{\mathrm{conn}}$ measured with a superatom. This indicates that noise is completely dominating in the reference pulses. Any structure seen in figure 5.9 b) is due to noise.

Comparing the correlation functions with the empty reference measurements show clearly that the superatom induces three-photon correlations on an initially uncorrelated pulse.

5.5.3 Center of mass dependency

The data shown in figure 5.8 is plotted for planes of R. Other ways of presenting the results can also be considered. Figure 5.10 shows a) the η plane of $g^{(3)}_{\mathrm{conn}}$ when $\zeta = 0$ and b) the ζ plane of $g^{(3)}_{\mathrm{conn}}$ for $\eta = 0$, both as a function of R for $\mathcal{R}_{\mathrm{in}} = 15.2\,\mu\mathrm{s}^{-1}$.

The two plots in figure 5.10 both show the same structure, namely a line of antibunching parallel to R accompanied by lines of bunching. In the very center for $\eta, \zeta = 0$ respectively, a faint line of equal time bunching is seen.

The edges of the figures are noisy due to the low signal to noise contributions from times on the rising and falling part of the Tukey pulse.

For η as a function of R when $\zeta = 0$ the resulting shape is a square diamond. This correspond to a slice along the diagonal of the datacube as shown in figure 5.3. This also becomes clear by

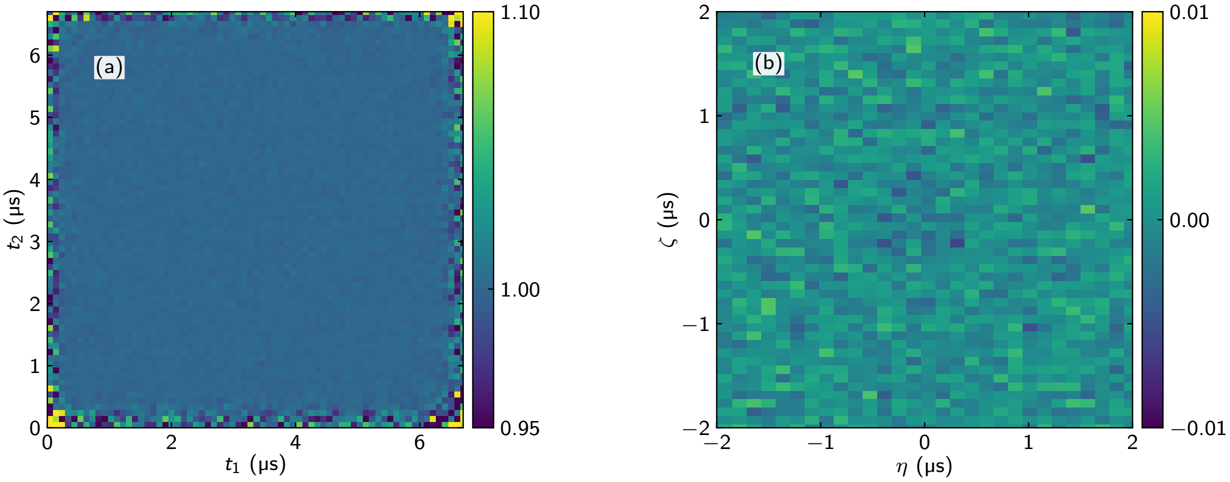

Figure 5.9: Reference pulses for $\mathcal{R}_{\text{in}} = 3.4\,\text{µs}^{-1}$. a) $g^{(2)}$ shows no correlations. b) $g^{(3)}_{\text{conn}}$ does not contain any information either.

setting $\zeta = 0$ in equation 5.3.4.

The plot for ζ is a rectangle standing on one point. Until $R = R_{\text{max}}/3$, the lower bound on ζ goes as $-\sqrt{2}R$, while the upper bound is rising with $\sqrt{1/2}R$. For $R_{\text{max}}/3 \leq R \leq 2R_{\text{max}}/3$, both upper and lower bound goes as $\sqrt{1/2}R$, and after that, the upper bound goes as $-\sqrt{2}R$, while the lower bound continues to increase as $\sqrt{1/2}R$. These three regimes correspond exactly to the slices of R being either an upside down triangle, a hexagon or a triangle.

The width of the line of antibunching depends on R, and the strength of the correlations around the line is seen to oscillate as a function of R, indicating that the system is not in steady state. Especially in figure 5.10 b), oscillations in the signal strength along R show up.

The width of both the faint peak at $\eta, \zeta = 0$ and the surrounding antibunching feature is also seen in figure 5.8. On this figure, the central peak for low photon rate is wider than for high photon rate, and the same will be seen in figure 5.10 if this is plotted for all three photon rates used here. The figures for lower photon rates are not shown here, as they are noisier.

That figure 5.10a) and b) are more noisy than figure 5.8c) is explained by figure 5.10 not being averaged over R. Noting the colorbar scale on these figures, it is seen that averaging will not only reduce noise, it will also wash out the contrast. Considering the hexagonal rings in figure 5.8 it is clear that any averaging over values of ζ and η in figures 5.10a) and b) respectively will smear the structure and can only be done for intervals of ζ and η respectively much smaller than the smallest ring feature.

In figure 5.10, it is seen that that $g^{(3)}_{\text{conn}}$ is not independent of the center of mass coordinate. This would be true only for a steady state case. In a), the signal for the first strip of antibunching and bunching around $\eta = 0$ oscillates with R.

The same is true for 5.10b), but whereas the oscillations are mirrored across $\eta = 0$, the oscillations in $g^{(3)}$ are shifted in R for values of ζ smaller and larger than $\zeta = 0$. This is a finite size effect, and for an infinite pulse this would not be the case.

The oscillation shift is due to the way the three times enter in ζ. Values of $\zeta > 0$ corresponds to the mean of t_1 and t_2 being greater than t_3, as shown in figure 5.4. Thus, for ζ along $\eta = 0$, which corresponds to $t_1 = t_2$, the positive part of ζ will be delayed compared to the negative part. The shift of oscillations is a result of the same effect which causes $g^{(3)}$ and $g^{(3)}_{\text{conn}}$ to have a triangular bias in the six-fold symmetric structure.

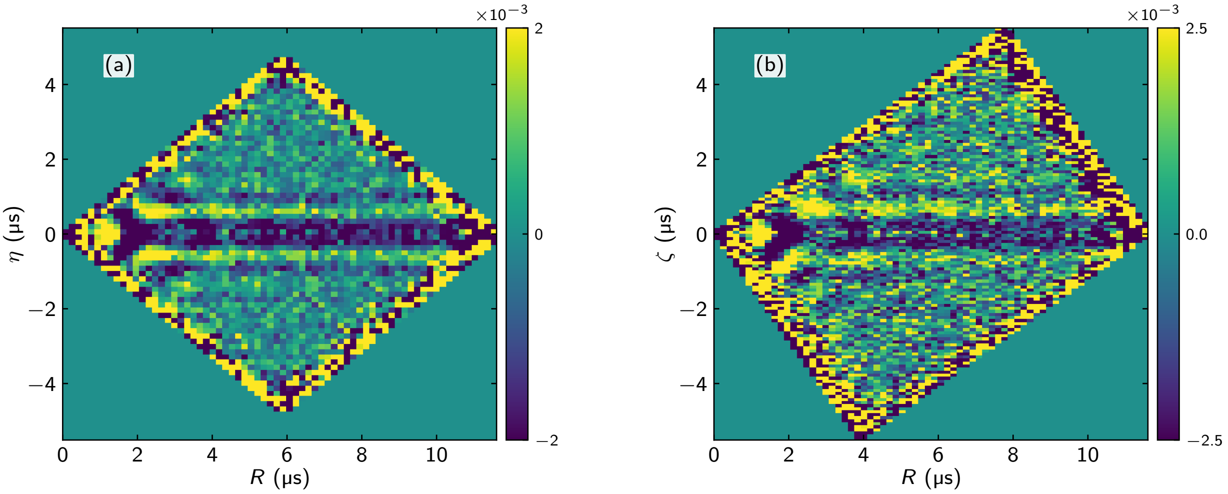

Figure 5.10: Cuts of η and ζ of $g^{(3)}_{\mathrm{conn}}$ as a function of R for photon rate $\mathcal{R}_{\mathrm{in}} = 15.2\,\mathrm{\mu s}^{-1}$. **a)** η as a function of R for $\zeta = 0$. **b)** ζ as a function of R for $\eta = 0$.

The time dependency of $g^{(3)}_{\mathrm{conn}}$ seen in figure 5.10 suggest to reconsider the averaging over R. The averaging is done under the assumption that the variation as a function of R is relatively small on the time scale of the R-range, but even small variations will smear any substructure.

To investigate the actual dependency of the signal on R, single planes of R are shown in figures 5.11 and 5.12. In figure 5.11, three planes of R are plotted. These are for $R = 2.5\sqrt{3}$µs, $R = 3.0\sqrt{3}$µs and $R = 3.5\sqrt{3}$µs. These values are chosen as they are the first, the half-way and the last value of the R-range contributing to figures 5.6 and 5.8.

As seen in figure 5.11, the structure of $g^{(3)}_{]\wr\backslash\backslash}$ depends on R. Figure 5.11 a) shows a flower-like structure with a slight triangular bias pointing up. Figure 5.11 b) shows a very perfect regular hexagon with a relatively sharp first ring of antibunching. Figure 5.11 c) shows again the shape of a flower with six petals. In contrast to figure 5.11a) and b) figure 5.11 c) does not show a central peak, its center shows only antibunching.

The color scale of figure 5.11 differs from the color scale of figure 5.8 c), as averaging washes out the contrast in figure 5.8.

From figure 5.11 the problem of averaging over R is clearly seen, as every slice of R through $g^{(3)}_{\mathrm{conn}}$ contains unique information about the time evolution of the outgoing field.

In figure 5.11 the signal to noise ratio is good enough to see the features of $g^{(3)}_{\mathrm{conn}}$. Considering the low photon rate case, as shown in figure 5.12, the signal to noise gets far worse. Figure 5.12 shows $g^{(3)}_{\mathrm{conn}}$ for the same planes of R as is shown in figure 5.11, namely $R = 2.5\sqrt{3}$µs, $R = 3.0\sqrt{3}$µs and $R = 2.5\sqrt{3}$µs.

In figure 5.12, the three different planes are also different, but the three figures are much more noisy. Figure 5.12a) has a triangular shape of antibunching. There is a peak in the center. For higher R, figure 5.12b) shows less triangular bias, and the central peak has vanished more or less. Figure 5.12c) has a more circular center than what was the case for the earlier values of R, and the structure around $\eta, \zeta = 0$ suggests that there might be some substructure within the central antibunching feature, but this information cannot be distinguished from the noise.

Thus to get a reasonable signal in the low photon rate case, some averaging over R is necessary, but it is clear that information is lost when averaging.

For the practical purpose of showing the signature of pure three-photon correlations averaging

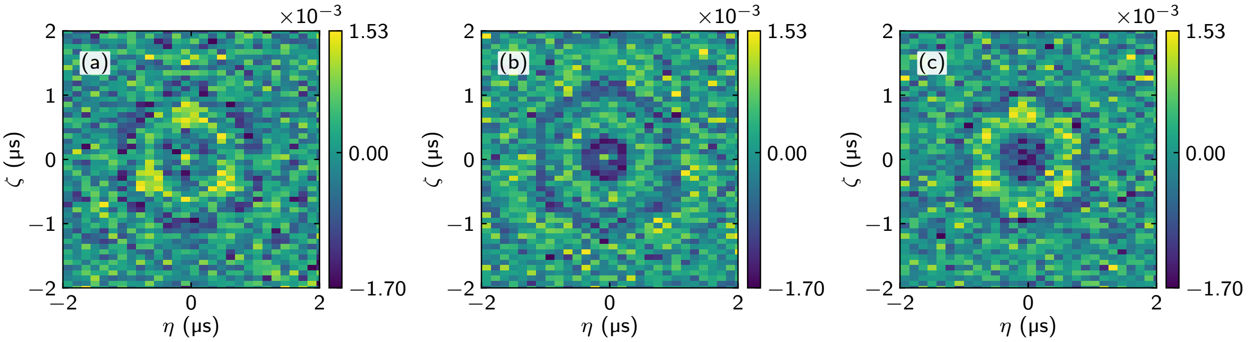

Figure 5.11: $g^{(3)}_{\text{conn}}$ for single planes of R for photon rate $\mathcal{R}_{\text{in}} = 15.2\,\text{μs}^{-1}$. The subfigures shown here correspond to $R = 2.5\sqrt{3}$μs, $R = 3.0\sqrt{3}$μs, and $R = 3.5\sqrt{3}$μs. It can be seen that the region changes for the different values of R. This shows how averaging over a range of R-values will cause some information to be lost. On the other hand the averaging over a range of R reduces the signal to noise substantially. This is especially important in the low photon rate, where the signal is the weakest.

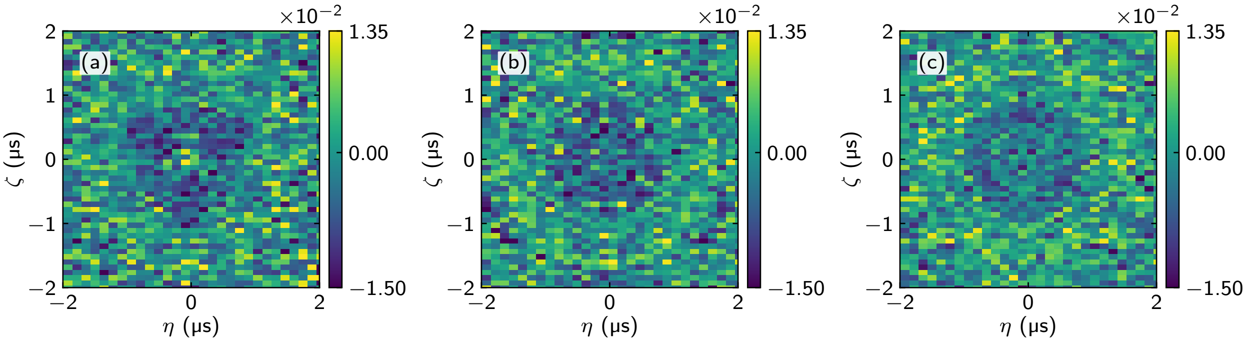

Figure 5.12: $g^{(3)}_{\text{conn}}$ for single planes of R for photon rate $\mathcal{R}_{\text{in}} = 3.4\,\text{μs}^{-1}$. Here the subfigures correspond to $R = 2.5\sqrt{3}$μs, $R = 3.0\sqrt{3}$μs, and $R = 3.5\sqrt{3}$μs. The central area of $g^{(3)}_{\text{conn}}$ varies for different values of R. Here for a low photon rate the noise is however obscuring much of the information.

over R is still valid. For comparison with the theory, averaging over R is also reasonable as long as the same averaging is done for the calculated results. On the point of calculated results, comparison of these specific planes of R to the corresponding theoretical values would be a strong way of testing the validity of the model.

5.5.4 The origin of three-photon correlations

The model described in section 2.4 predicts not only two body correlations but also three-body correlations. For the simple physical picture of the two-level system, shown in figure 2.1, two photon correlations can be readily understood as a rearrangement of the photons in the photon stream. The probability to reemit an absorbed photon is greater when a second photon is present to cause stimulated emission. Thus, two photons can readily be bunched just by stimulated emission.

In this very simple picture, it is harder to see how the three-photon correlation arises. This can be imagined by considering how the photon emission and absorption probability changes when many and few photons are present.

A single photon absorbed will have a higher probability to be reemitted if two photons are already present than if one is present, and along the same lines, three photons arriving at the atom will increase the probability of an absorption.

Following this argumentation, the probability of absorption increases with the photon rate. Thus it would be expected that for higher photon rates, correlations of order higher than three should arise as well.

The equations presented in section 2.4 can be solved analytically for a simplified system [38]. This analytic solution yields insight into the microscopic origin of the three-body correlations observed in the experiment. Here these theoretical results will only be treated briefly. The rigorous mathematical solution shows that the eigenstates of the solution are scattering states, two photon bound states with a third scattering photon and three-body bound states. The three-photon bound state naturally contributes to the connected third order correlation function.

Considering the wavefunction as function of three photon separation times the theory predicts the main contribution for equal times to stem from the three-body bound state, being four times larger than the contribution from pure scattering states and states with two bound photons and a third scattering state. The contribution to the wavefunction however decay faster than the other contributions.

So far the model has been solved for three photons ref to paper. For higher numbers of photons higher order bound states and thus higher order correlations are also assumed to contribute in a similar way as the three-body bound states, but as for the three-photon bound state, their contributions are assumed to decay even faster than the contribution from three-photon bound states.

Chapter 6

Multiple superatoms

While a single superatom was used to measure correlations between three photons, the setup described in section 4 has the versatility to introduce multiple dimple traps.

In this chapter we first introduce the advantage of multiple superatoms. In section 6.2, initial results for two superatoms are presented. The exploration of two superatoms yields very promising results for future experiments. With ion statistics show that we are approaching the case where one ion is always produced in each atomic ensemble, which would be a clear indication of two superatoms [12]. Further we study of the time traces of the ion measurements. These time traces show that due to the spatial separation of the two atomic ensembles, the ions from the different superatoms arrive at different times at the detector. Thus, from the ion time trace we can with high fidelity determine whether a Rydberg excitation was created in each cite.

However as described in section 4.2, the configuration of multiple dimple traps is very sensitive to alignment. These initial measurements are far from perfect but offer a promising outlook. Due to other experiments and lab renovation the two superatoms have so far not been pursued further than described here.

6.1 Multiple superatoms

As observed, a single superatom is close to unidirectional, due to the enhanced coupling to the forward mode of the probe light. This high probability of emission back into the system mode can be exploited for cascaded quantum systems [21].

The simplest system is a pair of emitters in series. In this case, a relevant system would be two superatoms separated by a distance much larger than the blockade radius. An incoming coherent light pulse will be modulated by the first superatom and then interact with the second superatom. Due to the separation, and the directional emission from both superatoms, it can be assumed that there will be only little or no backaction from the second superatom to the first.

Returning to the three fundamental processes; absorption, stimulated emission and spontaneous emission, shown in figure 2.1 in chapter 2, some initial proposals for the dynamics of two perfectly unidirectional two-level systems in series probed with resonant light can be given.

Consider an incoming photon pulse. The first two-level system would absorb a photon from the photon field and return it through stimulated emission, thereby bunching two photons together [30]. The second two-level system would receive this pulse of bunched photons and absorb one, thereby undoing the bunching.

From this argument, it could be considered whether the two-level systems in series will undo any correlations. This picture fails when considering a bunched pair arriving at the second

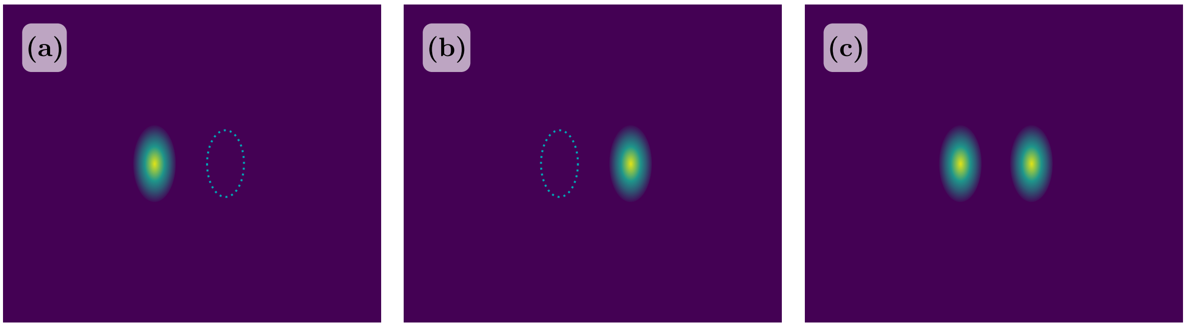

Figure 6.1: Illustrations of how investigations of two superatoms is done with each of the superatoms created independently as reference. The yellow spots illustrate the trapped superatom. The dashed outlines show where a second trap would be positioned if two traps were used. **a)** Only a single dimple trapping beam is on, and thus only one atomic ensemble is created in the first, rightmost position. **b)** Still only one dimple trap, but with a different position than for a). **c)** Two traps are created, realizing two superatoms in series.

two-level system, when this is already in the excited state. The two incoming photons will cause the emission of a third photon which will be bunched with the two already bunched photons.

Considering that three-photon correlations mediated by a single superatom have been shown experimentally in this thesis and the paper, multiple two-level systems can be expected to offer a light modulating dynamic beyond two photon correlations.

The signal of three-photon correlations, given by the connected third order correlation function $g^{(3)}_{conn}$, is two orders of magnitude smaller than the second order correlation function $g^{(2)}$. The naive assumption is that the correlation effects of introducing a second superatom after the first would also be higher order effects and cause modulations on the same qualitative level as the three-photon correlations. Whether these correlations are of sufficient intensity to be measured can be considered an open question, but since three-photon correlations are visible from the noise in the experiments presented here, it is expected that measurements of the two superatom modulations are possible.

It is however not clear so far what actually to expect of two superatoms in series, as also the theory does not give any clear predictions yet and as the experimental investigation of multiple superatoms have been brought to a halt due to construction work in the laboratory.

To investigate the correlations introduced by having two superatoms in series rather than a single superatom, correlations in the outgoing field should be measured for each superatom individually and then for the system of two simultaneous superatoms. Subtraction of the correlations introduced by one is expected to reveal the effect of introducing a second superatom. These three situations are illustrated in figure 6.1.

The setup is not limited to the superatom regime where the single photon detuning is large. As three-level systems, the two atomic ensembles offer a variety of parameters to tune, such as detunings from EIT resonance and internal dephasing parameters, allowing a number of possible investigations.

In the setup described here, the superatoms are created along the probe, in series. It is most common to investigate Rydberg interactions between separated atomic ensembles with the clouds in parallel. These setups offer the possibility to probe two atomic ensembles simultaneously and observe how they interact, as well as the option to probe the ensembles individually, thereby introducing a phase difference in the probe light exciting each atom [29, 48].

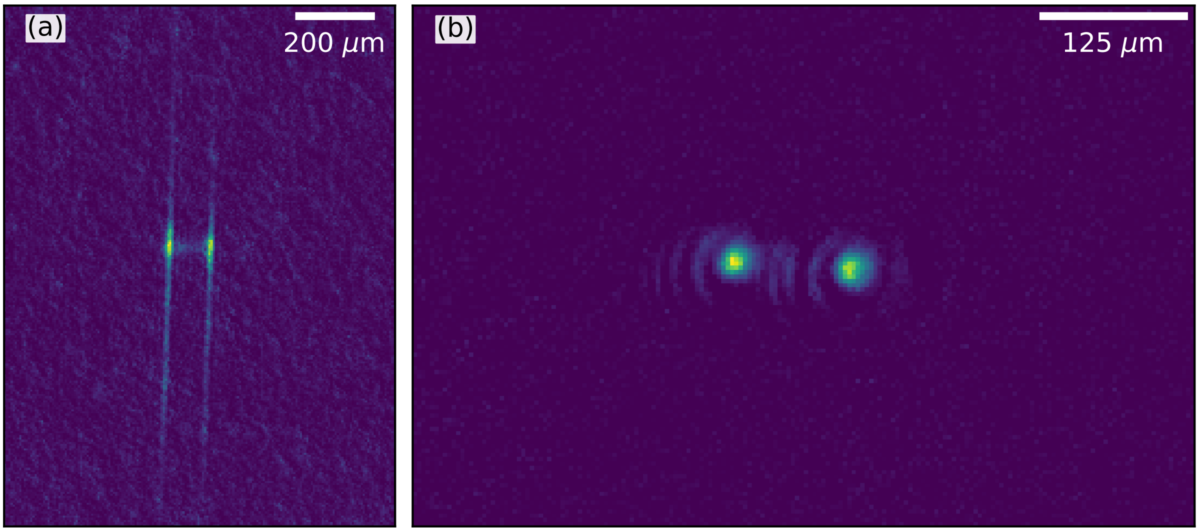

Figure 6.2: Two filled dimple traps as seen from the two imaging directions, **a)** is from above, averaged over 6 images. **b)** is from the imaging along the dimple traps, averaged over 6 images.

6.2 Initial results

The initial measurements on two superatoms presented here were performed on two atomic ensembles relatively similar to the single one presented in section 4.3. In chapter 4, several figures show multiple dimple traps. In figure 6.2, two atomic clouds in dimple traps are shown. Figure 6.2 a) shows the atomic clouds imaged from top for a time of flight measurement. From top imaging is defined as shown in figure 4.2. Figure 6.2 a) shows the dimple traps during alignment. The dimple beams are more visible towards the bottom of the image than towards the top, due to the dimple focus not being perfectly overlapped with the optical dipole trap. Due to this, some atoms are also seen in between the dimple traps, remaining in the dipole trap. It is further seen that the dimple beams come with a bit of an angle relative to the axes of the camera.

Figure 6.2 b) shows two filled dimple traps as seen with imaging along the dimple beams, as described in figure 4.2. The rotation with respect to the dipole trap discussed in chapter 4 is seen in figure 6.2, and can be compared to figure 4.7.

6.2.1 Ion detection and two photon absorption

The experimental setup includes a multi-channel plate (MCP) to detect ions. multiple electrodes are used to field-ionize the superatom and guide the resulting ion to the MCP. The field ionization pulse is applied after every experiment, to get rid of any remaining excitations.

The field ionization pulse addresses only atoms with a principal quantum number n higher than some lower limit such that only atoms excited to Rydberg states are addressed. Therefore, a true superatom can only produce a single ion, since it can only host a single excitation and only one atom can be ionized [12, 39]. With this in mind the ion counts can be used to determine the Rydberg population, and whether a true superatom is created. To investigate this, the number of ions is plotted as a function of photon rate, as shown in figure 6.3 a). The three lines in figure 6.3 a) represent two atomic ensembles (blue line), and each of the two ensembles on their own (orange and yellow lines). The green line shows the sum of the detected ions for the two

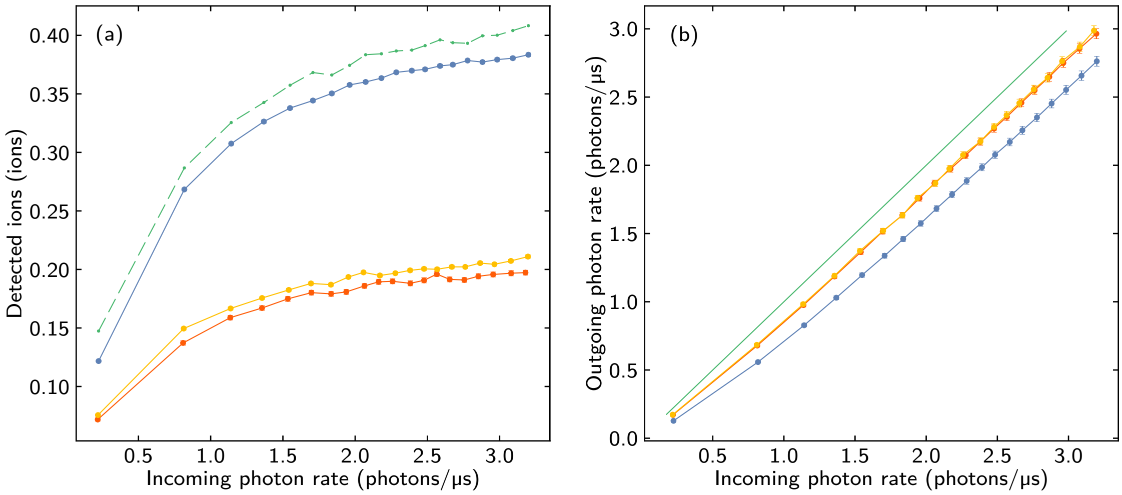

Figure 6.3: Incoming photons. **a)** Ions detected as a function of probe photon rate. Blue line is for two simultaneous superatoms, orange and yellow lines are for individual superatoms. The dashed green line shows the sum of ions from the two individually created atomic ensembles. The sum of ions from the two individual atomic ensembles should in the ideal case equal the number of ions created in two atomic ensembles created together. The lower number of ions created for two atomic ensembles is discussed in the text. **b)** Outgoing photon rate as a function of incoming photon rate. The blue line is for two superatoms while the orange and yellow lines corresponds to the individual superatoms. The green line shows the signal with no medium present.

individual superatoms. The green line should in principle coincide perfectly with the blue line, but here we observe that the total sum of ions from the individual atomic ensembles is different from the number of ions produced in the two simultaneously trapped atomic ensembles.

To understand the reduced ion count observed, we consider how two atomic ensembles are created. The ensembles are created by overlapping a dimple trap with the optical dipole trap. Atoms from the dipole trap will then fill the dimple trap, and the dipole trap will be turned briefly off to empty it of atoms outside of the dimple trap.

When loading two dimple traps from the dipole trap, there is the risk that the dipole trap does not contain enough atoms to fill two dimple traps with the same number of atoms as they would contain if only one had been created. This difference in atomic density will affect the absorption and hence the probability of exciting each superatom becomes a bit different if they are generated simultaneously or as a single superatom.

This is an important point to stress when considering the measurements proposed in section 6.1. To do meaningful measurements it is necessary to have dimple traps that are identical whether they are created alone or in multiples. If this condition is not practical, it is necessary to characterize this unavoidable difference.

It is shown in figure 6.3 a) that the number of detected ions does not increase linearly with the increasing photon rate. This is expected as the superatoms should only host one ion each. In principle the value should saturate, but in figure 6.3 a) the number of detected ions does not stop increasing for the chosen photon rates. This indicates that that the intensity in the light is not high enough to reach the saturation value, where an ion is created in every pulse. It can also indicate that the atomic ensembles created here are not fully blockaded. Additional ions can in principle come from some atoms remaining outside the dimple traps in a shallow dip caused by the dipole trap between the two dimple traps. This is briefly discussed in chapter 4, and to avoid this effect, the dipole trap intensity is ramped fully off before the probing to allow atoms outside of the dimples to evaporate.

Noting that the photon rate is not as high as for the measurements of three-photon correlations presented in chapter **??**, it is clear that these measurements were performed with a relatively conservative highest photon rate. As these are initial measurements, future measurements will go to higher photon rates.

Figure 6.3 b) shows the outgoing photon rate as a function of incoming photon rate. In this figure it is seen that the two individual atomic ensembles each absorbs the same amount of photons, and half as much as two atomic ensembles together.

6.2.2 Ion statistics

The ion measurements shown in figure 6.3 do not reach saturation, but some initial statistics can still be performed on them to help determine whether true superatoms are realized. A true superatom deterministically produces one and only one ion. To investigate whether this is the case, or whether the ions follow a Poisson distribution, it is useful to look at the Mandel Q-parameter [49]. Q is a measure for the deviation from Poissonian statistics.

For a stochastic variable x, Q is defined as

$$Q = \frac{\mathrm{var}(x)}{\langle x \rangle} - 1 = \frac{\langle x^2 \rangle - \langle x \rangle}{\langle x \rangle} - 1. \tag{6.2.1}$$

Where $\mathrm{var}(x)$ is the variance of x and $\langle x \rangle$ is the mean value of x. If x is drawn from a Poisson distribution, Q will be zero, as variance of x will equal the mean value. Therefore super/sub Po

Considering n ideal superatoms, the creation of ions can be described by n independent, not necessarily identical, Bernoulli trials. The trials are not necessarily identical, as the absorption in two superatoms might be different, and as detection efficiency may vary for ions from superatoms with different spatial positions. Such a system will follow a Poisson binomial distribution. With x as the number of successes, the mean of such a distribution is given by the sum of probabilities for success, while the variance is given by [50]

$$\mathrm{var}(x) = \sum_{i=1}^{n} (1 - p_i) p_i, \tag{6.2.2}$$

where p_i is the probability of success in the i'th trial. For a given mean value of the n trials, the variance on the number of successes will increase as the probabilities become more homogeneous and attend the maximum value when they are identical [50]. For n independent, not necessarily identical, Bernoulli trials, Q is

$$Q = \frac{\sum_{i=1}^{n} (1 - p_i) p_i}{\sum_{i=1}^{n} p_i} - 1 = -\frac{\sum_{i=1}^{n} p_i^2}{\sum_{i=1}^{n} p_i}. \tag{6.2.3}$$

If the probabilities are identical, $p_i = P$, it follows that $Q = -P$.

If two trials are performed, and they have different success probabilities, p_a, p_b, Q is expected to be

$$Q = \frac{(1 - p_a) p_a + (1 - p_b) p_b}{p_a + p_b} - 1 = -\frac{p_a^2 + p_b^2}{p_a + p_b}. \tag{6.2.4}$$

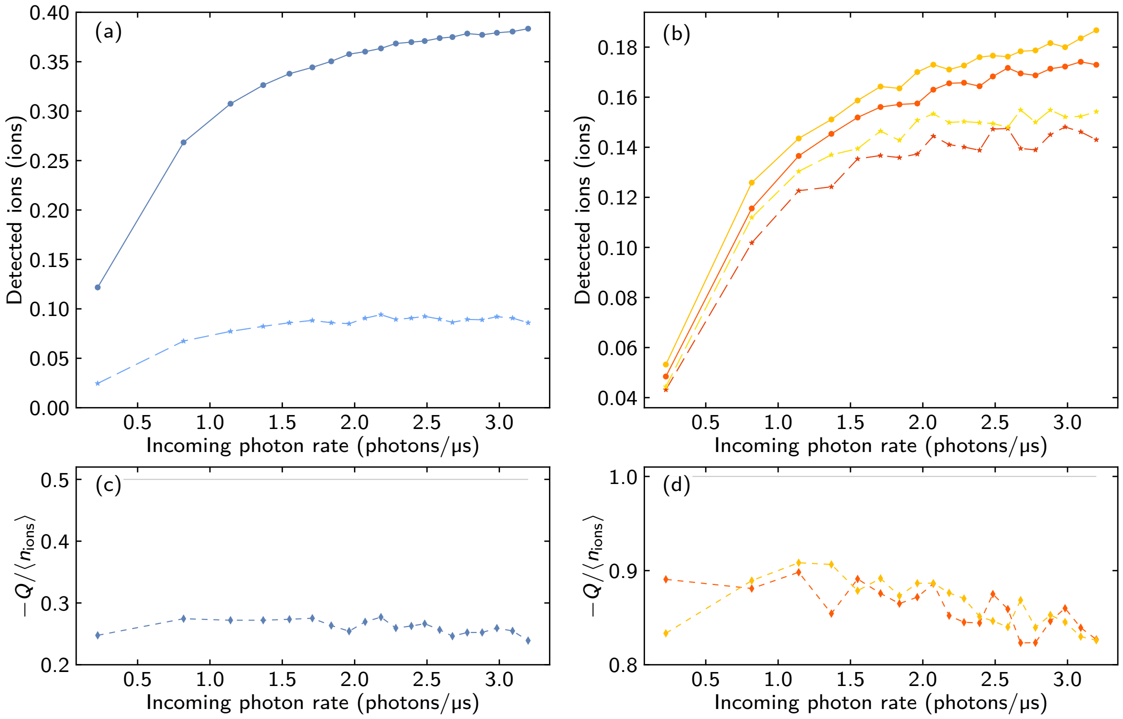

Figure 6.4: Mandel Q-parameter for the data shown in figure 6.3. **a)** shows the ion trace (solid line), and $-Q$, (dashed line) for the two simultaneously trapped atomic ensembles. $-Q$ does not correspond to half of the measured ions. **b)** Detected ions for a single atomic ensemble for two different positions (red and yellow solid lines). Dashed lines: connecting diamond points give the corresponding $-Q$. Again, $-Q$ is too low compared to the number of detected ions.. **c)** Blue line is $-Q/\langle n_{\mathrm{ions}}\rangle$ for the system of two trapped atomic ensembles. The grey line at $1/2$ shows the expected $-Q/\langle n_{\mathrm{ions}}\rangle$ for two identical, perfect superatoms. **d)** Orange and yellow lines: $-Q/\langle n_{\mathrm{ions}}\rangle$ for the two independent single atomic ensembles shown in b). The grey line at 1 shows the expected $-Q/\langle n_{\mathrm{ions}}\rangle$ for two identical, perfect superatoms.

Clearly Q will be furthest from zero when $p_a = p_b$.

Q over the distribution mean is another another measure for the deviation from Poissonian statistics. Dividing Q by the mean for the distribution will for n independent, identical Bernoulli trials be $-1/n$. For two superatoms with approximately the same detection efficiency, we would thus expect

$$\frac{Q}{\langle x\rangle} = -\frac{1}{2} \tag{6.2.5}$$

In the case where the probabilities are identical, the Q-parameter over the mean will be minus one over the number of trials, that is -1 for a single trial, $-1/2$ for two trials and so on. As seen in equation 6.2.4, $-1/2$ is the smallest achievable value, and is only true if the probabilities for success in the two trials are identical.

Plotting Q for the data given in figure 6.3 a) yields figure 6.4. Figure 6.4 a) shows $-Q$ and $-Q/\langle x\rangle$ for two superatoms. In figure 6.4 a), it is worth noticing that the dashed line representing $-Q$ is relatively far from half the number of detected ions, shown with the blue points. $-Q$ is instead relatively close to zero, the value Q takes for a Poissonian distribution.

This deviation can, to some extent, be explained by the same argument as why the number of detected ions for two superatoms does not correspond well to the sum of the ions detected for the two individual superatoms. The two superatoms generated simultaneously for these measurements are not independent in the sense that they are different from superatoms created one by one at the same positions. That the two superatoms have different detection efficiencies can be seen in figure 6.3 a), and this should indeed result in a lower value of the Mandel Q-parameter for the two superatoms, as the variance will be smaller for non-indentical probabilities [50].

For the individual superatoms, shown in figure 6.4 b), $-Q$ is closer to the number of detected ions. If the system was fully blocked by a single excitation, $-Q$ would have been expected to correspond exactly to the measured number of ions. Here however, $-Q$ is lower, again indicating that the individual superatoms does not deterministically produce a single ion. As discussed about figure 6.3 the maximal photon rate chosen is not close to the maximal photon rate used for the three-photon correlation measurements shown in chapter **??**. For the photon rates used here, we are not fully saturating the superatoms, and this will of course mean that the number of trials where no ion is created will change the statistics.

Figures 6.4 c) and d) show $-Q/\langle x\rangle$. If two ideal superatoms had been created, we would have expected the value in figure 6.4 c) to be centered around 1/2. It is however centered around approximately 1/4. A value lower than 1/2 is to some extent expected, as equation 6.2.4 will have minimum when the probabilities are equal, and as seen in figure 6.3 a) the two individual superatoms do not have the same detection efficiency. Studying figure 6.4 b), it is clear that for the two independent superatoms, Q over mean is not the expected -1 as expected for a Bernoulli trial, but slightly lower. A lower value indivates of $-Q/\langle x\rangle$ indicates that the superatoms are not fully blockaded. For experimentally realized superatoms, some effect of second photon absorptions are expected to increase $Q/\langle x\rangle$ [12, 39], however only at photon rates higher than what is used here. Therefore, the graphs shown in figure 6.4 c) and d) indicates that some atoms outside of the superatoms contributes ions to the staticstics, thereby yielding a system where the ion creation probability is closer to a Poissonian distribution than preferred.

6.2.3 Ion time traces

The results shown in figures 6.3 and 6.4 are the mean number of ions detected over an experiment and the mean photon rate over a pulse. Looking at the time traces yields further information about the system.

Figure 6.5 shows the mean time trace of probing experiments at constant photon rate. The signal is detected ions. The blue line shows the signal from two simultaneously created superatoms, while the yellow and red lines shows the ion trace for the individual superstoms respectively. The colors correspond to the colors in figure 6.3 and figure 6.4.

On figure 6.5 it is seen that the time it takes for the ions to reach the detector depends on the position where the ion is created, and thus the position of the superatom. In the case where more than one superatom is investigated, the ion signal from the different superatoms can be distinguished. Thus the red and yellow lines in figure 6.5 show the ion traces of a single superatom generated in two different positions. The blue line shows the time trace for two simultaneous superatoms. The blue line shows two main peaks with a temporal separation of 0.02 µs. This temporal spacing can, to some degree, be adjusted by adjusting the steering voltage.

The three subpeaks in each ion peak is caused by the screening wires in front of the MCP [42, 40]

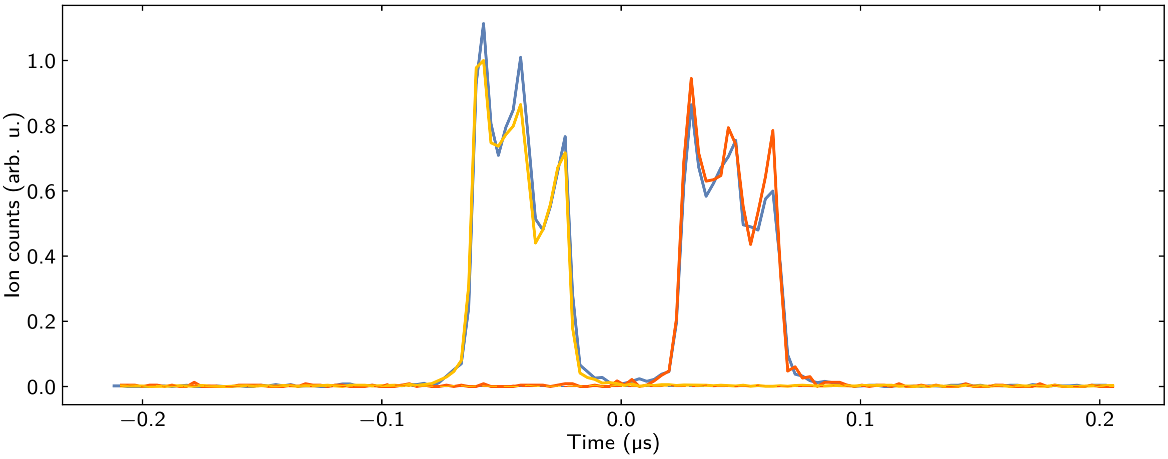

Figure 6.5: Ion time trace from two individually produced atomic ensembles and from two simultaneously created atomic ensembles. The blue line indicates the ion trace from two simultaneously created atomic ensembles. The red and yellow lines show the time trace of detected ions from each of the two atomic ensembles individually created. The lines are averaged over the ion counts from around 50 times 1000 experiments.

The observation that the ion trace from each superatom have a different arrival time allows post processing of data, as one can use the observation of whether ions arrives within both time windows or not as a measure for when two superatoms were excited. Hence for the data analysis it is possible to exclude experiments where this does not happen, and also to study the case where only one superatom is excited.

The distinguishable ion traces can, for instance, give an indication of whether two superatoms are equally likely to be excited for low photon numbers, or whether the probability of excitation depends on the presence of another superatom. This could, for instance, be the case if the first superatom pulse modulation makes the pulse more likely to interact with the second superatom.

6.2.4 Outlook for two superatoms

The initial results presented in the previous sections, sections 6.2.1, 6.2.2, and 6.2.3 clearly show that the two superatoms we have been studying are not yet ideal superatoms. It is also clear from figure 6.3 a) and figure 6.4 that the system of two superatoms generated simultaneously is not the sum of its components if these are studied individually, probably due to a fundamental difference between generating one and two superatoms. When two superatoms are generated simultaneously, they both fill depending on the atomic density in the optical dipole trap. This filling is not necessarily uniform for the two dimples, as it will depend on how well they are overlapped with the dipole trap. If only one dimple beam is used, the atomic trap does not have to 'share' atoms with another trap. Thus, it is possible that the two simultaneous superatoms have different atomic densities than their single counterparts due to the loading process.

Another source for deviation is the AOD intensity distribution, which seems to depend on the number of applied frequencies. This is briefly mentioned in section 4.1.3. Compared to the realization of a single superatom, two superatoms are harder to align, as also discussed briefly in chapter 5. The two superatoms should ideally have the same number of atoms interacting with the probe light so that the Rabi frequency for the two are the same. To realize this, the two superatoms must ideally be aligned similarly onto the dipole trap to give them identical atom numbers and they must be overlapped identically with the probe. Ideally, the focus of the probe should be exactly in between the two dimple traps.

To ease the alignment of two superatoms, a number of steps can be taken in the future, for instance introduction of a horizontal telescope to enlarge the dimple traps perpendicular to the probes, such that they are less sensitive to alignment onto the dipole trap. It is further an option to add yet another trapping beam, along the probe beam. With such a trap, it will be possible to create two dimples further apart, and thus have them less prone to steal atoms from each other.

It thus is clear from the inital results presented here, that while a system of two or more superatoms offers a variety of exciting experiments, the implementation is delicate.

Chapter 7

Conclusion

In this thesis, measurements of correlations between three photons mediated by a single Rydberg superatom are presented, and initial results for a cascaded quantum system consisting of two Rydberg superatoms are discussed.

To realize a Rydberg superatom, our existing experimental setup has been extended to include an additional optical trap. Such an additional optical trapping setup has been tested and implemented during the scope of the thesis. The trap setup make use of an AOD, which allows us to have multiple dimple traps, and thereby create multiple superatoms at the same time.

With this new experimental capability, our first scientific use was to investigate three-photon correlations mediated by a single superatom. In particular, we managed to observe a clear signature in the connected part of g3 even after subtraction of g2. These correlation measurements are in good qualitative agreement with the results predicted by theory.

Furthermore, comparison to an idealized analytical model suggests that the three-photon correlation stems from three body bound states in the photon wavefunction.

These results have led to a joint publication with theory partners from Universitẗ Stuttgart.

The experimental trapping setup with the AOD is not limited to the realization of a single superatom. In the current setup, four radio frequency fields can be applied to the AOD, which in principle allows the realization of four highly confined atomic ensembles in series.

In the scope of this thesis, a setup of two Rydberg superatoms has been investigated, and the initial results are presented here. The ion statistics presented here indicate that with the current alignment the two superatoms are not yet fully blockaded. Furthermore, the initial measurements on two superatoms in series have yielded slightly different results for two atomic ensembles created simultaneously and for each of the components created alone. This observation indicates that our two traps are created in such a way that they compete for some atoms, leading to lower densities in the two serial traps than the densities in the individually created traps. The difference may also be caused by deviations in the AOD intensity distribution as a function of the number of applied rf-fields. However, in the view of the early stage of the investigations, the results for two superatoms look promising for future experiments.

One particular result from our first investigations is that in our ion-detection setup, ions resulting from the two superatoms can be time-resolved on our single MCP. This permits us to measure the Rydberg population of each ensemble independently, which will provide additional information for two (or possibly more) superatoms. One possible future use is in post-processing of data, because we can select for data where light has interacted with both ensembles

7.1 Outlook

The results presented in chapter 6 for two trapped atomic ensembles show that further work is necessary to realize two fully blockaded ensembles acting as Rydberg superatoms, and to have the ensembles behave identically whether they are created together or one by one. To improve the performance of the two atomic ensembles, a number of experimental steps can be taken. One of them is the planned introduction of yet another trapping beam, this one along the probe direction. With such a trap, two dimple traps can be generated further apart than is possible now, and then be ramped to the position of interest. In this way, the possibility of the two dimple traps stealing atoms from each other would be ruled out.

To counter the problem of the intensity in a beam from the AOD depending on the number of applied rf-fields, an aperture could be introduced in the beam path, allowing us to always operate the AOD with two applied fields. When only one dimple is of interest, we would be able to deflect the other beam with a large angle and clip it on the aperture.

Considering the three-photon correlations, further investigation could be done if phase measurement of phase was possible in the experiment. Therefore, we will implementation of a phase measurement setup in the existing setup. With phase measurement, the full wavefunction of the photons can be determined, and we are not limited to probe only the probability of states. The phase measuring setup would also give valuable information about the interactions of two superatoms with light.

Bibliography

[1] Jonathan P Dowling and Gerard J Milburn. Quantum technology: the second quantum revolution. *Philosophical transactions. Series A, Mathematical, physical, and engineering sciences*, 361(1809):1655–74, aug 2003.

[2] H. J. Kimble. The quantum internet. *Nature*, 453(7198):1023–1030, jun 2008.

[3] Darrick E. Chang, Vladan Vuletić, and Mikhail D. Lukin. Quantum nonlinear optics — photon by photon. *Nature Photonics*, 8(9):685–694, sep 2014.

[4] O Firstenberg, C S Adams, and S Hofferberth. Nonlinear quantum optics mediated by Rydberg interactions. *Journal of Physics B: Atomic, Molecular and Optical Physics*, 49(15):152003, aug 2016.

[5] M. D. Lukin, M. Fleischhauer, R. Cote, L. M. Duan, D. Jaksch, J. I. Cirac, and P. Zoller. Dipole Blockade and Quantum Information Processing in Mesoscopic Atomic Ensembles. *Physical Review Letters*, 87(3):037901, jun 2001.

[6] Shuai Chen, Yu-Ao Chen, Thorsten Strassel, Zhen-Sheng Yuan, Bo Zhao, Jörg Schmiedmayer, and Jian-Wei Pan. Deterministic and Storable Single-Photon Source Based on a Quantum Memory. *Physical Review Letters*, 97(17):173004, oct 2006.

[7] Y O Dudin and A Kuzmich. Strongly interacting Rydberg excitations of a cold atomic gas. *Science (New York, N.Y.)*, 336(6083):887–9, may 2012.

[8] Thibault Peyronel, Ofer Firstenberg, Qi Yu Liang, Sebastian Hofferberth, Alexey V. Gorshkov, Thomas Pohl, Mikhail D. Lukin, and Vladan Vuletić. Quantum nonlinear optics with single photons enabled by strongly interacting atoms. *Nature*, 2012.

[9] T. G. Tiecke, J. D. Thompson, N. P. de Leon, L. R. Liu, V. Vuletić, and M. D. Lukin. Nanophotonic quantum phase switch with a single atom. *Nature*, 508(7495):241–244, apr 2014.

[10] H. Gorniaczyk, C. Tresp, J. Schmidt, H. Fedder, and S. Hofferberth. Single-Photon Transistor Mediated by Interstate Rydberg Interactions. *Physical Review Letters*, 113(5):053601, jul 2014.

[11] E. Urban, T. A. Johnson, T. Henage, L. Isenhower, D. D. Yavuz, T. G. Walker, and M. Saffman. Observation of rydberg blockade between two atoms. *Nature Physics*, 5(2):110, 2009.

[12] C. Tresp, C. Zimmer, I. Mirgorodskiy, H. Gorniaczyk, A. Paris-Mandoki, and S. Hofferberth. Single-photon absorber based on strongly interacting rydberg atoms. *Phys. Rev. Lett.*, 117:223001, Nov 2016.

[13] L. Li, Y. O. Dudin, and A. Kuzmich. Entanglement between light and an optical atomic excitation. *Nature*, 498(7455):466–469, jun 2013.

[14] T. Wilk, A. Gaëtan, C. Evellin, J. Wolters, Y. Miroshnychenko, P. Grangier, and A. Browaeys. Entanglement of Two Individual Neutral Atoms Using Rydberg Blockade. *Physical Review Letters*, 104(1):010502, jan 2010.

[15] Marlan O. Scully and M. Suhail Zubairy. *Quantum Optics.* Cambridge University Press, 1997.

[16] M. D. Eisaman, J. Fan, A. Migdall, and S. V. Polyakov. Invited Review Article: Single-photon sources and detectors. *Review of Scientific Instruments*, 82(7):071101, jul 2011.

[17] Jens Honer, R. Löw, Hendrik Weimer, Tilman Pfau, and Hans Peter Büchler. Artificial Atoms Can Do More Than Atoms: Deterministic Single Photon Subtraction from Arbitrary Light Fields. *Physical Review Letters*, 107(9):093601, aug 2011.

[18] Marlan O. Scully, Edward S. Fry, C. H. Raymond Ooi, and Krzysztof Wódkiewicz. Directed Spontaneous Emission from an Extended Ensemble of N Atoms: Timing Is Everything. *Physical Review Letters*, 96(1):010501, jan 2006.

[19] Asaf Paris-Mandoki, Christoph Braun, Jan Kumlin, Christoph Tresp, Ivan Mirgorodskiy, Florian Christaller, Hans Peter Büchler, and Sebastian Hofferberth. Free-space quantum electrodynamics with a single rydberg superatom. *Phys. Rev. X*, 7:041010, Oct 2017.

[20] Qi-Yu Liang, Aditya V. Venkatramani, Sergio H. Cantu, Travis L. Nicholson, Michael J. Gullans, Alexey V. Gorshkov, Jeff D. Thompson, Cheng Chin, Mikhail D. Lukin, and Vladan Vuletić. Observation of three-photon bound states in a quantum nonlinear medium. *Science*, 359(6377):783–786, 2018.

[21] Peter Lodahl, Sahand Mahmoodian, Søren Stobbe, Arno Rauschenbeutel, Philipp Schneeweiss, Jürgen Volz, Hannes Pichler, and Peter Zoller. Chiral quantum optics. *Nature*, 541(7638):473–480, jan 2017.

[22] J. J. (Jun John) Sakurai. *Advanced quantum mechanics.* Addison-Wesley Pub. Co, 1967.

[23] Thomas F. Gallagher and Cambridge University Press. *Rydberg Atoms.* Cambridge University Press, 1994.

[24] C. J. Foot. *Atomic physics.* Oxford University Press, 2005.

[25] C.S Adams, M Sigel, and J Mlynek. Atom optics. *Physics Reports*, 240(3):143–210, may 1994.

[26] Daniel A. Steck. *Quantum and Atom Optics.* available online at `http://steck.us/teaching`, 2007, (revision 0.12.2, 11 April 2018).

[27] Mark (Anthony Mark) Fox. *Quantum optics: an introduction.* Oxford University Press, 2006.

[28] Sebastian Weber, Christoph Tresp, Henri Menke, Alban Urvoy, Ofer Firstenberg, Hans Peter Büchler, and Sebastian Hofferberth. Calculation of rydberg interaction potentials. *Journal of Physics B: Atomic, Molecular and Optical Physics*, 50(13):133001, 2017.

[29] Alpha Gaëtan, Yevhen Miroshnychenko, Tatjana Wilk, Amodsen Chotia, Matthieu Viteau, Daniel Comparat, Pierre Pillet, Antoine Browaeys, and Philippe Grangier. Observation of collective excitation of two individual atoms in the Rydberg blockade regime. *Nature Physics*, 5(2):115–118, feb 2009.

[30] Ofer Firstenberg, Thibault Peyronel, Qi-Yu Liang, Alexey V Gorshkov, Mikhail D Lukin, and Vladan Vuletic. Attractive photons in a quantum nonlinear medium. *Nature*, 502(7469):71–75, oct 2013.

[31] R. H. Dicke. Coherence in Spontaneous Radiation Processes. *Physical Review*, 93(1):99–110, jan 1954.

[32] T. M. Weber, M. Höning, T. Niederprüm, T. Manthey, O. Thomas, V. Guarrera, M. Fleischhauer, G. Barontini, and H. Ott. Mesoscopic Rydberg-blockaded ensembles in the superatom regime and beyond. *Nature Physics*, 11(2):157–161, feb 2015.

[33] Y O Dudin, L Li, F Bariani, and A Kuzmich. Observation of coherent many-body Rabi oscillations. *Nature Physics*, 8, 2012.

[34] P. Bienias, S. Choi, O. Firstenberg, M. F. Maghrebi, M. Gullans, M. D. Lukin, A. V. Gorshkov, and H. P. Büchler. Scattering resonances and bound states for strongly interacting Rydberg polaritons. *Physical Review A*, 90(5):053804, nov 2014.

[35] Asaf Paris-Mandoki, Christoph Braun, and Sebastian Hofferberth. Correlations between interacting Rydberg atoms. In *AIP Conference Proceedings*, volume 1950, page 020001. AIP Publishing LLC, apr 2018.

[36] E. Brion, L. H. Pedersen, and K. Molmer. Adiabatic Elimination in a Lambda System. oct 2006.

[37] Christoph Braun. *Free-Space Quantum Electrodynamics with a single Rydberg superatom.* Master thesis, Universität Stuttgart, 2017.

[38] Kevin Kleinbeck. *Quantum Light Interaction with Superatoms.* Master thesis, Universität Stuttgart, 2017.

[39] Christoph Tresp. *Rydberg polaritons and Rydberg superatoms - Novel tools for quantum nonlinear optics.* PhD thesis, Universität Stuttgart, 2017.

[40] Hannes M. Gorniaczyk. *Single Photon Transistor mediated by electrically tunable Rydberg-Rydberg Interactions.* PhD thesis, Universität Stuttgart, 2016.

[41] Rudolf Grimm, Matthias Weidemüller, and Yurii B. Ovchinnikov. Optical Dipole Traps for Neutral Atoms. *Advances In Atomic, Molecular, and Optical Physics*, 42:95–170, jan 2000.

[42] Johannes Schmidt. *Generation of non-classical light using ultra-cold Rydberg ensembles.* Master thesis, Universität Stuttgart, 2014.

[43] M Assmann, F Veit, M Bayer, M van der Poel, and J M Hvam. Higher-order photon bunching in a semiconductor microcavity. *Science (New York, N.Y.)*, 325(5938):297–300, jul 2009.

[44] Markus Koch, Christian Sames, Maximilian Balbach, Haytham Chibani, Alexander Kubanek, Karim Murr, Tatjana Wilk, and Gerhard Rempe. Three-Photon Correlations in a Strongly Driven Atom-Cavity System. *Physical Review Letters*, 107(2):023601, jul 2011.

[45] Christoph Hamsen, Karl Nicolas Tolazzi, Tatjana Wilk, and Gerhard Rempe. Two-Photon Blockade in an Atom-Driven Cavity QED System. *Physical Review Letters*, 118(13):133604, mar 2017.

[46] Paolo Sibani and Henrik Jeldtoft Jensen. *Stochastic Dynamics of Complex Systems*, volume 2 of *Series on Complexity Science.* IMPERIAL COLLEGE PRESS, apr 2013.

[47] Krzysztof Jachymski, Przemysław Bienias, and Hans Peter Büchler. Three-Body Interaction of Rydberg Slow-Light Polaritons. *Physical Review Letters*, 117(5):1–5, 2016.

[48] Hannes Busche, Paul Huillery, Simon W. Ball, Teodora Ilieva, Matthew P. A. Jones, and Charles S. Adams. Contactless nonlinear optics mediated by long-range Rydberg interactions. *Nature Physics*, 13(7):655–658, 2017.

[49] L. Mandel. Sub-poissonian photon statistics in resonance fluorescence. *Opt. Lett.*, 4(7):205–207, Jul 1979.

[50] Y. H. Wang. On the number of successes in independent trials. *Statistica Sinica*, 3(2):295–312, 1993.

Acknowledgment

It should be no secret, that my acknowledgement could easily take up as much space as the rest of this thesis, since so many people should be thanked for contributing to this work or for making every day special. In particular I would like to mention

- Sebastian Hofferberth for excellent guidance and supervision, and for the opportunity to work on this incredibly cool project as the first Danish master student. I could not be happier that you choose to relocate to here, you have brought so many good things!
- The group members, current and former: Asaf Paris-Mandoki, Christoph Braun, Christoph Tresp, Florian Christaller, Philipp Lunt, Simon W. Ball, and Tom Asmussen for good company, sheepish humour, and interesting discussions. Every day that I have spent with you guys I have learned something new.
- Christoph Tresp, not only for all the fun times and for teaching me so much, but also for being someone to look up to; I can happily say I learned from the best. I hope that you will only work with super stable experiments that are completely free of dust.
- Philipp Lunt who a always bring a spark of humor and insight to my day. I so admire how you always courageously challenge yourself, both regarding science, puzzles, and jumping into the icy waters of the harbor bath.
- Simon Ball for providing a great deal of my daily dose of dry humor and for proof reading this work. It would have turned out much worse if it was not for you!
- Jan Kumlin, Kevin Kleinbeck and Hans Peter Büchler for excellent collaboration. It is always a pleasure to work with great minds!
- The employees at FKF who provide a very nice working environment with a positive atmosphere and lots of humor. Also, my fellow students, both from FKF and Imada.
- All my other friends! Especially my amazing galpals both from the university and elsewhere; my friends from Hjerneblod, my outreachbesties Sara, Sofie, and Majken, and my masters of Lego.
- My rugby squad for being the best team. We don't win much, but you girls won my `<3`.
- Glenn. You are the best!
- My family, especially my parents, who have provided perfect curling for a curlingchild both before and during this thesis. Hvor er vi heldige, vi har hinanden.